POLITECNICO DI MILANO

School of Industrial and Information Engineering

Master of Science in
Space Engineering

POLITECNICO
MILANO 1863

MODELING AND OPTIMIZATION OF AERO-BALLISTIC CAPTURE

Supervisor
Prof. Francesco TOPPUTO

Candidate
Carmine GIORDANO
Matr. 836570

ACADEMIC YEAR 2015/2016

Abstract

In this thesis a novel paradigm for Mars missions is formulated, modeled and assessed. This concept consists of a maneuver that combines two of the most promising methods in terms of mass saving: aerocapture and ballistic capture; it is labeled aero-ballistic capture. The idea is reducing the overall cost and mass by exploiting the interaction with the planet atmosphere as well as the complex Sun–Mars gravitational field. The aero-ballistic capture paradigm is first formulated. It is split into a number of phases, each of them is modeled with mathematical means. The problem is then stated by using optimal control theory, and optimal solutions, maximizing the final mass, are sought. These are specialized to four application cases. An assessment of aero-ballistic capture shows their superiority compared to classical injection maneuvers when medium-to-high final orbits about Mars are wanted.

Sommario

In questa tesi, è formulato, modellato e valutato un nuovo paradigma per missioni verso Marte. Questi consiste in una manovra che combina due dei metodi più promettenti in termini di riduzione della massa, l'aerocattura e la cattura balistica, ed è definito cattura aero-balistica. L'idea è di ridurre il costo totale e la massa andando a sfruttare sia l'interazione con l'atmosfera sia il complesso campo gravitazionale creato dal Sole e da Marte. Come primo punto, è formulato il paradigma della cattura aero-balistica, dividendo la manovra in una serie di fasi, ognuna modellata matematicamente. Successivamente il problema è esposto utilizzando la teoria del controllo ottimo in modo da cercare soluzioni ottime, che massimizzino la massa. Queste sono analizzate in dettaglio per quattro casi studio. Una valutazione sulla cattura aero-ballistica mostra la superiorità di queste soluzioni rispetto alle manovre classiche di inserimento intorno a Marte quando l'orbita finale desiderata ha un'altitudine media o alta.

Ringraziamenti

Vorrei ringraziare, prima di tutto, il Prof. Topputo per la sua disponibilità e il suo supporto durante tutto il periodo di sviluppo di questa tesi. Un sentito grazie per i preziosi consigli e per avermi indicato sempre la giusta direzione da seguire nel lungo periodo di studio per questo lavoro.

Un grazie di cuore a tutte le persone che, in tutti questi anni, ho incontrato e che hanno percorso un pezzo di strada con me e mi hanno aiutato a crescere non solo dal punto di vista accademico, ma soprattutto umano.
Un ringraziamento speciale va a Giorgio e a Chiara e a Luca e alla Fede: siete stati la mia famiglia a Milano in questi anni, più di ogni altro, e mi avete fatto sentire a casa. Vi devo davvero molto.
Un caloroso grazie a tutti i ragazzi e le ragazze del Convitto, con i quali ogni giorno ho vissuto momenti di gioia: grazie per aver reso splendido il tempo al San Geatano e per il calore che mi date, in ogni istante. Un ringraziamento particolare va ad Andrea: ho convissuto e condiviso con te per 5 anni ogni momento universitario e privato, mi hai dato supporto e consiglio per qualsiasi cosa, sei un amico prezioso. Ah, e ti devo ancora qualche birra, forse. A Ruggiero e a Giovanni: mi dispiace non aver potuto condividere con voi questo ultimo periodo, ma un grande grazie lo devo anche a voi, per tutti i momenti belli che ho trascorso in vostra compagnia. Un grazie di cuore ad Anna: sei una persona speciale; la tua tenacia e la tua forza nell'affrontare le avversità della vita sono state e saranno d'inspirazione per me. Grazie infinite per l'aiuto e il supporto, ti auguro tutto il meglio dalla vita.
Un immenso grazie è per Vittoria: ci conosciamo da poco, ma è come se ci conoscessimo da sempre. Abbiamo condiviso tanti bei momenti in questi mesi e sei stata di grande aiuto sempre, incondizionatamente. Grazie davvero di tutto.

Un ringraziamento va agli amici che hanno vissuto al mio fianco da tempo immemore. Giovanni, Federico, Salvatore, vi conosco da sempre e abbiamo condiviso un bel po' di avventure insieme. E, per quanto qualcuno sia sparito ultimamente (ogni riferimento a Monte è puramente casuale) vi ringrazio per il tempo felice trascorso insieme e che farà sempre parte di me. Un grazie grande va a Valentina: per una volta non importa se hai fatto il classico, e hai qualche piccola difficoltà in matematica, grazie davvero per essermi stata di supporto sempre in questi anni. E anche quando la distanza ci ha separati, ci sei sempre stata. Un affettuoso grazie, poi, a Sara per avermi sopportato e supportato

lungo tutto il periodo universitario, anche se lontani. Non dimenticherò mai il tuo aiuto sempre presente.

Infine, desidero ringraziare tutta la mia grande famiglia, che ha saputo circondarmi di bene e di affetto. In particolare, un grazie immenso va ai miei nonni, presenza silenziosa ma costante da sempre, e a zia Rita, per avermi sostenuto sempre e dato sempre tutto il possibile, sotto ogni aspetto. Un grazie di cuore è per Ciccio: sei sempre stato il mio mentore, mi hai insegnato tutto il possibile sulla vita, mi hai insegnato a capire gli altri e a guardare oltre le apparenze in ogni situazione. Grazie davvero.

Più di tutto, però, il mio grazie più sentito e più grande va ai miei genitori e a mio fratello. Senza di voi, senza il vostro sostegno e incoraggiamento, constante e forte, soprattutto nei momenti più bui, non avrei mai avuto la possibilità di arrivare a questo traguardo e di perseguire i miei sogni. Vi voglio un bene immenso.
Un grazie speciale è, poi, tutto per Marianna. Degli anni trascorsi lontano da casa, il mio unico rimorso è non aver avuto la possibilità di esserti stata vicino e di non averti visto crescere. Ti ho lasciato che eri una bambina e ti ritrovo ragazza. Spero di essere riuscito ad essere un buon esempio per te e di averti dato tanto, almeno quanto tu hai dato a me. Ti voglio bene.

Come ultima cosa, vorrei dedicare questo giorno tanto importante alle persone che non potranno esserci, ma che sono state per me fondamentali per diventare quel che sono, che mi hanno voluto bene e che mi hanno dato molto, permettendomi di raggiungere questo momento. A zia Silvana e zio Arturo, a zia Maria, ma soprattutto a nonna Mena: in questo giorno, il mio pensiero e la mia dedica è per voi.

TABLE OF CONTENTS

Page

List of Tables **x**

List of Figures **xii**

1 Introduction **1**
- 1.1 Aerocapture . . . 2
- 1.2 Ballistic capture . . . 3
- 1.3 State of the art . . . 4
  - 1.3.1 Aerocapture . . . 4
  - 1.3.2 Ballistic capture . . . 4
- 1.4 Motivations . . . 5
- 1.5 Research question & Goals . . . 6
- 1.6 Outline of the thesis . . . 7

2 Aerocapture modeling **8**
- 2.1 Vehicle geometry . . . 8
- 2.2 Aerocapture dynamics . . . 9
  - 2.2.1 Complete three-dimensional model . . . 10
  - 2.2.2 Simplified bi-dimensional model . . . 12
- 2.3 Mars atmosphere . . . 13
- 2.4 Heating rates . . . 14
  - 2.4.1 Heating rates model . . . 14
  - 2.4.2 TPS selection . . . 15

3 Ballistic Capture modeling **17**
- 3.1 Elliptic Restricted Three-Body Problem . . . 17
  - 3.1.1 Polar coordinates . . . 19

3.1.2 Energetic considerations 20
3.1.3 Circular Restricted Three-Body Problem 20
3.1.4 Lagrangian points 21
3.2 Sun gravitational assist 21
3.2.1 Sun gravitational assist in ER3BP 25

4 Aero-Ballistic Capture modeling **27**
4.1 Approaching phase 29
4.2 Atmospheric phase 29
4.3 Ballistic phase 30
4.3.1 From atmospheric phase to ballistic phase 31
4.3.2 Mathematical characterization 33
4.4 Final orbit 33

5 Aero-Ballistic Capture optimization **35**
5.1 Aerocapture optimization 36
5.1.1 Singular control in aerocapture 37
5.1.2 Conclusions for control in aerocapture 39
5.2 Aero-ballistic capture optimization 40
5.2.1 Singular control in aero-ballistic capture 42
5.2.2 Conclusions for control in aero-ballistic capture 43
5.3 Nonlinear Programming Problem statement 43
5.4 Numerical techniques 45
5.4.1 Minimization 45
5.4.2 Integration 48
5.4.3 Heat flux integration 52
5.4.4 Summary 52

6 Results **55**
6.1 Study cases 55
6.2 Aero-ballistic capture solutions 56
6.2.1 Low-Mars orbit 56
6.2.2 Areostationary 59
6.2.3 Moons 63
6.3 Reference aerocapture solutions 66
6.3.1 Methodology 66

6.3.2 Low-Mars orbit 67
6.3.3 Areostationary 69
6.3.4 Moons 72
6.4 Reference impulsive-maneuver solutions 74
6.4.1 Methodology 76
6.4.2 Low-Mars orbit 77
6.4.3 Areostationary 78
6.4.4 Moons 80
6.5 General comparison 81

7 Critical analysis **83**
7.1 Robustness analysis against single-point failure 83
7.1.1 Robustness analysis against optimal parameters 85
7.2 Critical analysis 88

8 Conclusions and further developments **92**
8.1 Summary of results 92
8.2 Future improvements 93

Bibliography **94**

List of Tables

Table		Page
2.1	Spacecraft parameters	9
2.2	Mars atmosphere properties	14
3.1	Sun–Mars Three-Body problem parameters	19
5.1	Local optimization algorithms comparison	47
5.2	Summary of data related to different integration schemes	50
5.3	Summary of differences between RK8 and trapezoidal rule for heat flux	52
6.1	Study cases main data	56
6.2	Optimization parameters for ABC to LMO	56
6.3	Relevant values for ABC to LMO	59
6.4	Optimization parameters for ABC to ASO	60
6.5	Relevant values for ABC to ASO	63
6.6	Optimization parameters for ABC to moons	63
6.7	Relevant values for ABC to Phobos	66
6.8	Relevant values for ABC to Deimos	66
6.9	Optimization parameters for AC to LMO	68
6.10	Relevant values for AC to LMO	69
6.11	Optimization parameters for AC to ASO	70
6.12	Relevant values for AC to AS	72
6.13	Optimization parameters for AC to moons	72
6.14	Relevant values for AC to Phobos	74
6.15	Relevant values for AC to Deimos	74
6.16	Relevant values for direct insertion to a LMO	77
6.17	Optimization parameters for two-impulse maneuver to LMO	78
6.18	Relevant values for two-impulse maneuver to LMO	78

6.19 Relevant values for direct insertion to AS 78
6.20 Optimization parameters for two-impulse maneuver to AS 79
6.21 Relevant values for two-impulse maneuver to AS 79
6.22 Relevant values for direct insertion to a moons' orbits 80
6.23 Optimization parameters for two-impulse maneuver to moons' orbits 81
6.24 Relevant values for two-impulse maneuver to moons. 81

7.1 Relevant values for ABC to ASO with $f_0 = 45°$ 91

List of Figures

Figure **Page**

1.1 Aerocapture steps 2

2.1 Capsule shape 9
2.2 Aerocapture reference frames 10
2.3 Atmospheric density models comparison 13
2.4 TPS mass fraction history 16

3.1 ER3BP reference frames with polar coordinates 18
3.2 Lagrangian points location 21
3.3 Solar gravity gradient reference figure 22
3.4 Solar gravity gradient field lines near Mars 23
3.5 Solar gravity gradient field effect on orbits near Mars 23
3.6 Adimensional angular momentum variation near Mars 24

4.1 Aero-ballistic capture steps 28
4.2 Definition of α and initial true anomaly. 32

5.1 Optimal bank angle profile 40
5.2 Cost function in dependence of t_s and σ_d. 46
5.3 Cost function in dependence of t_s and α. 46
5.4 Comparison among different integration schemes 49
5.5 Graphical representation of the regula falsi method 51
5.6 Block scheme for solving NLP problem 53
5.7 Algorithm to solve NLP problem for aero-ballistic capture optimization 54

6.1 Atmospheric phase for ABC to LMO 57
6.2 Ballistic phase for ABC to LMO 58
6.3 Atmospheric phase for ABC to AS 61

6.4 Ballistic phase for ABC to ASO 62
6.5 Atmospheric phase for ABC to moons 64
6.6 Ballistic phase for ABC to ASO 65
6.7 Atmospheric phase for AC to LMO 68
6.8 Atmospheric phase for AC to AS 70
6.9 Transfer and final orbits for AC to AS 71
6.10 Atmospheric phase for AC to moons 73
6.11 Direct insertion 74
6.12 Two-impulse maneuver steps 75
6.13 Trajectories of two-impulse maneuver to LMO 79
6.14 Trajectories of two-impulse maneuver to ASO 80
6.15 Comparison of between aero-ballistic capture and aerocapture 82

7.1 Trajectory propagation in case of SPF for ABC to ASO 84
7.2 Final constraint violation for optimal parameters variation 86
7.3 Solution for ABC to ASO with $\sigma_d = \sigma_d^* + 4^\circ$ 87
7.4 Earth–Mars porkchop plot 88
7.5 Earth–Mars porkchop plot with V_∞ areas 89
7.6 Earth–Mars porkchop plot with V_∞ areas and $f_0 = 0$ lines 90
7.7 Earth–Mars porkchop plot with V_∞ areas and $f_0 = 45^\circ$ lines 91

CHAPTER 1

INTRODUCTION

In space exploration, mass has always been a major limiting factor, imposing a very restrictive constraint on missions. Since launch vehicles have limited capability in term of payload, there is the need of minimizing the launch mass while achieving the scientific goals. So, mass optimization is a key factor in space engineering, because it allows improving the scientific return.
Space engineering works in two directions in order to fulfill this constraint:

- Searching for new technologies, being able to improve efficiency of the spacecraft (e.g. lighter structures, better propellant properties);
- Deepening orbital mechanics knowledge, in order to find less fuel-expensive maneuvers.

In this document, the second option is followed. The basic idea is to merge two different approaches, aerocapture and ballistic capture, in order to obtain less fuel consuming and safer trajectories.
Mars is selected as case study in this work. The choice is related to the interest about the *Red Planet* in the scientific community, in planetology, space science, exobiology. Furthermore, a strong knowledge of the planet is required to forecast human missions. For these reasons, many cargo probes will be sent to Mars in the next future and so "fuel-optimal" trajectories will be needed.

1.1 Aerocapture

Aerocapture is an orbital maneuver that allows to change the trajectory of a spacecraft from hyperbolic to elliptical orbit.
The technique starts with the spacecraft approaching the target body on a hyperbolic orbit having the pericenter below the atmospheric interface, and so the probe enters in the atmosphere. Orbital energy is removed by aerodynamic drag and the spacecraft is on a closed orbit at the exit from the atmosphere, with a desired final apocenter. At the apocenter of this transfer orbit, a firing is given in order to raise the pericenter above the interface. So aerocapture can be divided into three phases:

1. a hyperbolic approaching phase;
2. an atmospheric phase;
3. a ballistic phase on a transfer orbit up to the final orbit.

Figure 1.1 shows the different steps of an aerocapture.

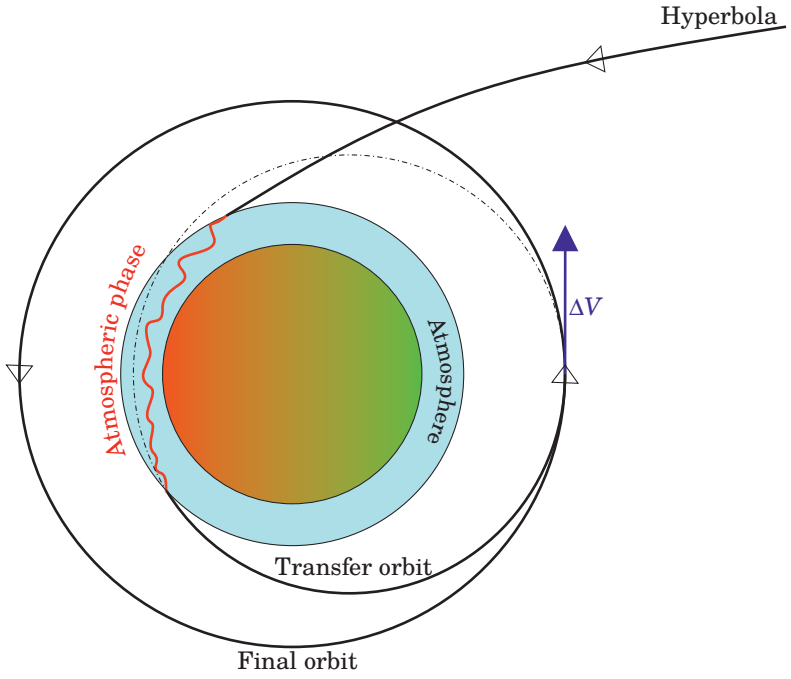

FIGURE 1.1. The different phases of aerocapture: the spacecraft arrives on a *hyperbola*; then the *atmospheric phase* (in red) brings the vehicle on a *transfer orbit*; a propelled maneuver is performed (in blue) moving it to the *final orbit*.

In some conditions a second propelled maneuver has to be performed at the final pericenter in order to bring the apocenter at a desired altitude, if the sought value is not attained.
The aerocapture reduces the amount of propellant needed to go from the hyperbolic approaching up to the final orbit and, thus, the spacecraft is more efficient.
On the other hand, this maneuver needs spacecraft with a capsule-like shape in order to yield appropriate lift-to-drag ratios and a good control authority. A closed-loop guidance has to be also implemented. Furthermore a dedicated thermal protection system (TPS) is required in order to manage the high heat load produced by friction. The heat-shield is jettisoned after the atmospheric phase.

1.2 Ballistic capture

Ballistic capture is a technique used to reduce the amount of propellant needed to change orbit in space, exploiting the gravitational accelerations provided on the spacecraft by different celestial bodies.
The classical approach used to design interplanetary trajectories is the so called *patched-conics* method: the whole spacecraft trajectory is created patching different two-body problems and, for each leg, the vehicle is considered to be inside a *Sphere of Influence* where it is subjected only to the gravity force of the central body. The model used in this technique is very simple and allows to reduce the computational time, since an analytic solution exists; but this dynamics is oversimplified and does not permit to find some interesting trajectories that are able to reduce the amount of propellant needed. For this reason, more complex models are introduced, like the restricted three-body problem, with the spacecraft affected by the gravity accelerations of two different primaries at the same time. Under these assumptions, if a spacecraft attains a body with low relative velocity from outside the sphere of influence, some non-Keplerian low-energy orbits can be found; these allow the spacecraft to temporarily revolve about the planet. Usually little fuel is needed to stabilize them. Of course, a drawback is present: they take longer to complete than classical Hohmann transfers.
This kind of orbits are called *ballistic capture trajectories* or *weak stability boundary trajectories* or otherwise *low-energy transfers*, since the orbital energy is lower than that of a classical Keplerian orbit.

1.3 State of the art

1.3.1 Aerocapture

In the last thirty years, aerocapture has been the subject of some relevant papers ([32], [4], [41]), even if it has never been used in a real mission. Benefits of this technique with respect to a fully propulsive maneuver, both in terms of spacecraft mass and costs, are clearly shown in [5]. In this study, a payload mass increase of 15% is obtained for Martian scenarios. Even better performances are documented for other celestial objects: for example, spacecraft mass for a Titan mission can be improved by 280%.
For this reason, this approach was studied for different bodies in the solar system, both for moons ([15], [36]) and for planets ([34], [16]). Aerocapture was analyzed also for re-entry on the Earth [13], but many studies focuses on Mars [40], for the scientific interest about that planet, but also because a CNES-NASA sample return mission, called Mars Sample Return Orbiter, scheduled for 2005 but never performed, was designed exploiting this technique [3].
Since that the dynamics related to aerocapture is not very complex and quite well known, nowadays papers are focusing on finding a reliable, accurate and high-performance guidance [19]. Different algorithms were developed, most of them using the bank angle as control command, designed in order to ensure a correct exit condition, that is the one allowing the spacecraft to reach the desired apocenter. These algorithms can be group in different categories: analytical predictor-corrector ([6], [24]), numerical predictor-corrector [30] or terminal point controller [33]. Algorithms using a different control variable were also investigated [12].
Recently, a *closed-loop* optimal aerocapture guidance was developed [19], starting from an entry guidance algorithm [18]. It confirms theoretically what was showed numerically in previous studies [25]: if post-atmospheric ΔV minimization is desired, using the bank angle as control, the optimal trajectory has a bang-bang structure, with the vehicle flying nearly full lift up, then almost full lift down.

1.3.2 Ballistic capture

The concept of ballistic capture was first introduced in early 90s by Belbruno and Miller for Earth to Moon transfer [1]. They stated the concept of *weak stability boundaries*, which are locations in phase space where a spacecraft can move from an unstable to a stable orbit, freely, without fuel. This approach was later successfully used to rescue the

Japanese spacecraft *Hiten*.
Since this technique was proven to be effective and efficient, many studies focused their aim in this subject. A method for finding this kind of orbits was devised in order to extend them from the Earth-Moon system to interplanetary trajectories, under the assumption of the *circular restricted three body problem* (CR3BP) [39]. Also in this more complex situation, numerical simulation showed that the ballistic capture is still feasible. However the classical restricted three body problem is not capable of representing in a very accurate way the Solar system dynamics, because the real trajectories of the planets are still too simplified. For this reason, studies on the *elliptic restricted three body problem* (ER3BP) were performed ([8], [9]). The method used in these papers to design ballistic capture was then extended to a n-body problem, representing accurately the three-dimensional dynamics of the planetary orbits, through the ephemeris [22]. Also in this framework, the simulations showed the effectiveness of the method in finding good solutions. Under these assumptions, the effects of natural satellites in ballistic capture was later addressed [21].
A summary and a comparison among all these frameworks (circular three-body, elliptic three-body and three-dimensional n-body) can be found in [20]: it is showed that the ER3BP is a good approximation of the real model and it allows to save computational time and effort.
All these different studies produce only temporary orbits about the smaller primary. It was demonstrated that permanent capture by the smaller primary in the R3BP is of no probability [7]. So a stabilization mechanism through dissipation is required.
Additionally, different studies were performed in order to better understand the effects of "planetary" relative configuration on the ballistic capture ([2], [44], [43]).

1.4 Motivations

Ballistic capture and aerocapture were quite well investigated in the last years, because they are able to improve the efficiency of the interplanetary missions, so reducing the propellant needed to close the orbit and thus increasing the scientific return.
These two approaches were studied separately up to now. Firstly, because they are ontologically different and the combination is not trivial. Secondly, they exist for different conditions: in aerocapture, the spacecraft at Mars arrival is on an hyperbola, with high incoming velocity; on the contrary, in ballistic capture, the vehicle is on lower velocity trajectories. Also the models used are different, considering that a patched conics appro-

ach is adopted for aerocapture; instead ballistic capture is feasible only under a more complex multi-body problem.
Nevertheless, a combination of these two techniques can be beneficial in term of mass with respect to the two approaches taken separately. In fact, for what concerns aerocapture, a merging will possibly reduce the heat and mechanical stresses on the Thermal Protection System, and this means lower mass for the heat shield. Moreover, the pericenter can be raised by exploiting the Sun perturbation, allowing to perform the propulsive maneuver at the pericenter, and not at the apocenter, reducing the amount of propellant needed thanks to the Oberth effect. On the other hand, a mix of these two *different worlds* can shorten the time of flight compared to a simple ballistic capture.
To account of this, the merging of ballistic capture with aerocapture in order to obtain less fuel-expensive, cheaper and safer trajectories has to be investigated.

1.5 Research question & Goals

A study that tries to combine aerocapture and ballistic capture does not exist. Thus, this document have as primary objective the characterization and the modeling of this brand-new technique. Furthermore, an optimal solution maximizing the scientific return is sought, applying the optimal control theory. As last point, a comparison between this approach and classical methods has to be analyzed.
In conclusion, this study has to answer the following question:

> To what extent a maneuver combining aerocapture and ballistic capture can bring advantages over the classic ways used to inject a spacecraft into an orbit about Mars?

In order to answer this question, it is needed to undertake a number of steps:

1. Formulate the concept of aero-ballistic capture;
2. Model both the atmospheric and ballistic part of the trajectory;
3. Carry out an end-to-end optimization of this maneuver;
4. Perform an accurate comparison with classic aerocapture or fully impulsive orbit injections.

1.6 Outline of the thesis

In the first part of the thesis, the models used in the study are appropriately selected, developed and explained. In the Chapter 2 models related to aerocapture are presented: the vehicle shape and dimensions, the dynamics, the atmospheric model and the heating rates affecting the spacecraft, together with the Thermal Protection System selection, are deeply analyzed. In Chapter 3 definitions, dynamics and trajectory effects of ballistic capture are discussed.
In Chapter 4, the aero-ballistic capture is introduced, starting from definitions. Then the dynamics related to the different phases is modeled, together with the links between two consecutive phases.
Chapter 5 contains a discussion about the optimal control theory both for aerocapture and aero-ballistic capture. Transcription of optimal control problems into non-linear programming problems is presented. Finally, numerical techniques developed to solve these problems are showed.
In Chapter 6, results are presented. First, solutions of aero-ballistic capture, related to some interesting final orbits, are discussed. Then, a comparison with aerocapture results and fully-propulsive maneuvers is performed on these study cases. Consequently, the main result, consisting in a general comparison among all these techniques for different circular final orbits, is presented.
In Chapter 7, robustness against single-point failure and parameters' variation is analyzed, followed by a critical analysis on the feasibility of those solutions.
Final considerations and possible further developments are given in Chapter 8.

CHAPTER 2

AEROCAPTURE MODELING

In order to properly describe the dynamics of the spacecraft during the atmospheric flight, some models related to different aspects of the problem are selected and described.
The choice of the models to adopt is driven by a compromise between accuracy and computational effort. The adopted models are able to provide a first solution, that as far as approximated can assess the feasibility of the described maneuvers.

2.1 Vehicle geometry

In aerocapture, the spacecraft has a capsule-like shape. This peculiar form allows to dissipate orbital energy, converting it into thermal energy and at the same time it has a good lift-to-drag ratio, giving a good control authority. Furthermore, the heat loads can be managed quite easily using this shape. Capsule shapes are also used in most aerocapture studies in literature.
Figure 2.1 shows the vehicle used in this thesis. As depicted, the spacecraft is a typical sphere-cone vehicle: it is composed by a spherical section with a blunted cone attached. This shape guarantees a better dynamic stability with respect to a spherical capsule. Furthermore, this shape was commonly used for Mars entry vehicles in the past. The spacecraft will enter the atmosphere with the conical section first. Its relevant geometric parameters are the nose radius r_n and the base radius r_b and, for this study, the dimensions are based on the ones of the Mars Sample Return Orbiter [24]. A 70° half-

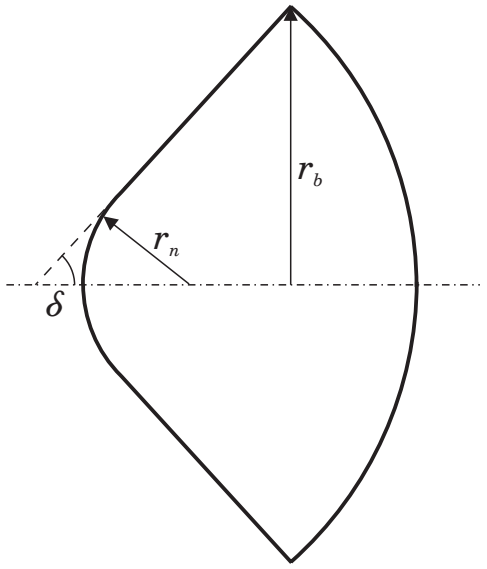

FIGURE 2.1. Capsule shape with relevant parameters

angle δ (the angle between the cone axis and its outer surface) is selected, like most previous mission on Mars [26].
Spacecraft data are summarized in Table 2.1.

r_n [m]	r_b [m]	S [m^2]	δ [°]	m_0 [kg]
0.2013	1.659	8.647	70	2200

TABLE 2.1. Spacecraft parameters

The base surface $S = \pi r_b^2$ is taken as reference for the aerodynamic coefficients.
The mass of the vehicle is set equal to the one in [24].

2.2 Aerocapture dynamics

The spacecraft dynamics in the atmospheric phase is described using a set of ordinary differential equations (ODEs): it is derived starting from the generic complete 3-D ODEs system, making then some simplifying assumptions.
The simplified dynamics allows to describe quite accurately the vehicle trajectory inside the atmosphere, reducing at the same time the computational effort needed to integrate the equations and to perform optimization.
Firstly, the complete model is described. Then the simplified model is presented as a reduction of the former.

2.2.1 Complete three-dimensional model

The vehicle dynamics is described using a local non-inertial reference frame (x, y, z), centered on the spacecraft center-of-mass, with the y axis directed towards North, the z axis pointing the local zenit and the x axis taken to complete the triad. Then, a planetocentric non-inertial reference frame (**X**, **Y**, **Z**) is defined. The **Z** axis points toward the North pole. The other two directions are defined such that the plane defined by **X** and **Y** contains the Equator and the plane defined by **X** and **Z** contains the prime meridian. This frame rotates with respect to the planetocentric inertial reference frame (X, Y, Z) (defined with the Z axis poiting the North pole and the X axis pointing the vernal equinox) with the planet angular velocity $\Omega_{\male}$ about the axis Z.
The local and the planetocentric non-intertial reference frame are linked through the longitude θ and the latitude ϕ.
Furthermore, the velocity vector is represented in the local reference frame using the magnitude V, the flight path angle γ and the heading angle ψ, measured clockwise from the north in the local horizontal plane. Figure 2.2 highlights all these quantities.

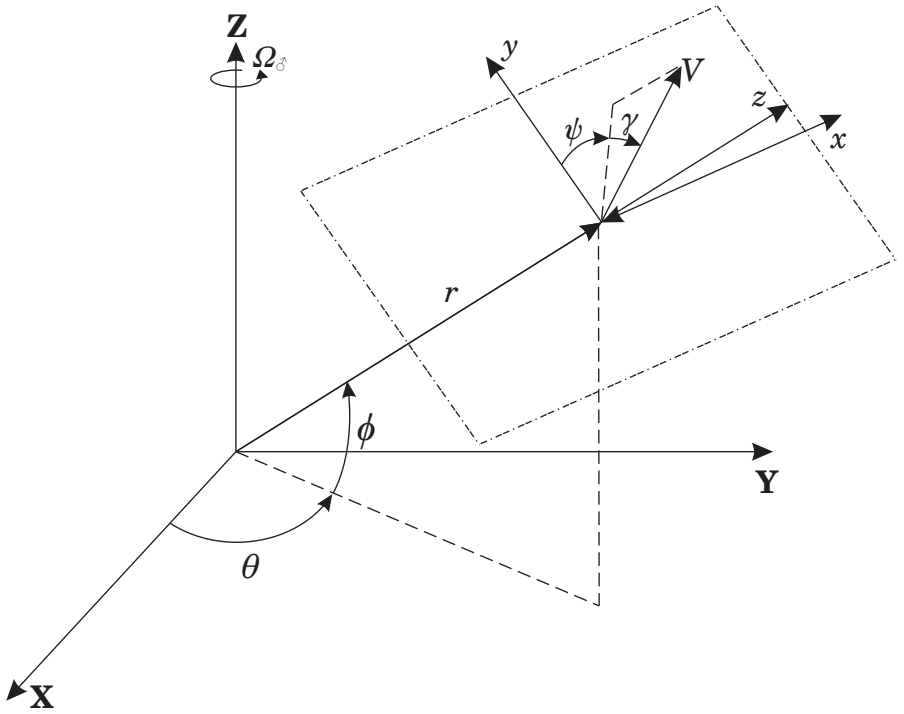

FIGURE 2.2. Local and non-inertial planetocentric reference frames with state vector variables definition

If an ellipsoidal rotating planet is considered, the equations of motion can be described using six coupled ODEs, three describing the kinematics and three related to the dynamics. They are

$$\dot{r} = V \sin\gamma \tag{2.1}$$

$$\begin{aligned} \dot{V} = &-D - g_r \sin\gamma - g_\phi \cos\gamma \cos\psi \\ &+\Omega_{\male}^2 r \cos\phi \left(\sin\gamma\cos\phi - \cos\gamma\sin\phi\cos\psi\right) \end{aligned} \tag{2.2}$$

$$\begin{aligned} \dot{\gamma} = \frac{1}{V}\Bigg[&L\cos\sigma + \left(\frac{V^2}{r} - g_r\right)\cos\gamma + g_\phi \sin\gamma\cos\psi + 2\Omega_{\male} V \cos\phi\sin\psi \\ &+\Omega_{\male}^2 r\cos\phi\left(\cos\gamma\cos\phi + \sin\gamma\cos\psi\sin\phi\right)\Bigg] \end{aligned} \tag{2.3}$$

$$\dot{\theta} = \frac{V\cos\gamma\sin\psi}{r\cos\phi} \tag{2.4}$$

$$\dot{\phi} = \frac{V\cos\gamma\cos\psi}{r} \tag{2.5}$$

$$\begin{aligned} \dot{\psi} = \frac{1}{V}\Bigg[&\frac{L\sin\sigma}{\cos\gamma} + \frac{V^2}{r}\cos\gamma\sin\psi\tan\phi + g_\phi\frac{\sin\psi}{\cos\gamma} \\ &-2\Omega_{\male} V\left(\tan\gamma\cos\psi\cos\phi - \sin\phi\right) + \frac{\Omega_{\male}^2 r}{\cos\gamma}\sin\psi\sin\phi\cos\phi\Bigg] \end{aligned} \tag{2.6}$$

where r is the distance from the planet center and σ is the bank angle [19]. By definition, the bank angle is the angle of rotation of the vehicle about the velocity vector, positive with the right wing down. L and D are the lift and drag accelerations. They can be written as

$$L = \frac{1}{2}\rho V^2 S\frac{C_L}{m_0}$$

$$D = \frac{1}{2}\rho V^2 S\frac{C_D}{m_0}$$

with m_0 the spacecraft mass. The density ρ is function of r (see Section 2.3); instead, the aerodynamics coefficients C_L and C_D are dependent on the angle of attack. Usually, in these problems, the angle of attack is function of the Mach number; but, in aerocapture, the Mach number is very high and the motion is considered fully hypersonic. For this reason, these coefficients can be considered constant. For the vehicle used in this document $C_D = 1.723$ and the ratio $C_L/C_D = 0.27$ is the same of capsule-like spacecrafts [24].

The terms g_r and g_ϕ are the gravity accelerations, respectively in radial and lateral directions. If a planet with the zonal term J_2 dominating the other ones is considered, they can be written in an approximate form as:

$$g_r = \frac{\mu_{\male}}{r^2}\left[1+\frac{3}{2}J_2\left(\frac{R}{r}\right)^2\left(1-3\sin^2\phi\right)\right]$$

$$g_\phi = \frac{\mu_{\male}}{r^2}\left[3J_2\left(\frac{R}{r}\right)^2\left(3\sin\phi\cos\phi\right)\right]$$

where $\mu_{\male}$ is the standard gravitational parameter of Mars and R is the equatorial radius of the planet.

2.2.2 Simplified bi-dimensional model

The equations of motion for the atmospheric phase can be simplified without losing too much in accuracy, making some assumptions. First of all, since the atmospheric phase of the aerocapture maneuver lasts only few minutes, the rotation of the planet can be neglected. Also the non-spherical gravity can be ignored due to its small magnitude. (In fact, $\Omega_{\male} = 4.061\times10^{-3}$ °/s and $J_2 = 1.960\times10^{-3}$).
Under these assumptions, the equations of motion become:

$$\dot{r} = V\sin\gamma \tag{2.7}$$

$$\dot{V} = -D - \frac{\mu_{\male}}{r^2}\sin\gamma \tag{2.8}$$

$$\dot{\gamma} = \frac{1}{V}\left[L\cos\sigma + \left(V^2 - \frac{\mu_{\male}}{r}\right)\frac{\cos\gamma}{r}\right] \tag{2.9}$$

$$\dot{\theta} = \frac{V\cos\gamma\sin\psi}{r\cos\phi} \tag{2.10}$$

$$\dot{\phi} = \frac{V\cos\gamma\cos\psi}{r} \tag{2.11}$$

$$\dot{\psi} = \frac{1}{V}\left[\frac{L\sin\sigma}{\cos\gamma} + \frac{V^2}{r}\cos\gamma\sin\psi\tan\phi\right] \tag{2.12}$$

It is clear that the Eqs. (2.7), (2.8) and (2.9), describing the longitudinal dynamics, are decoupled from the other three equations, describing the lateral dynamics. For this reason, the in-plane trajectory can be studied separately from the out-of-plane one.

2.3 Mars atmosphere

This study is fully centered on Mars. Since the aerocapture dynamics is strongly dependent on the characteristics of the atmosphere, a good model for the Martian environment has to be implemented.
The simple exponential model for the air density is not capable of giving the desired accuracy. For this reason, the model suggested by Justus [10] is implemented. It is based on the Committee on Space Research (COSPAR) Mars Reference Atmosphere [28]: values of density, temperature and pressure are tabulated for different altitudes; a spline interpolation with not-a-knot end conditions is used to connect the different points, in order to have a class $\mathscr{C}^2$ function. The difference between this model and the exponential model is shown in the Figure 2.3: for lower altitudes the two models give similar results, but the higher is the altitude, the larger is the gap.
The interface for Mars atmosphere is set at an altitude of 125 km.

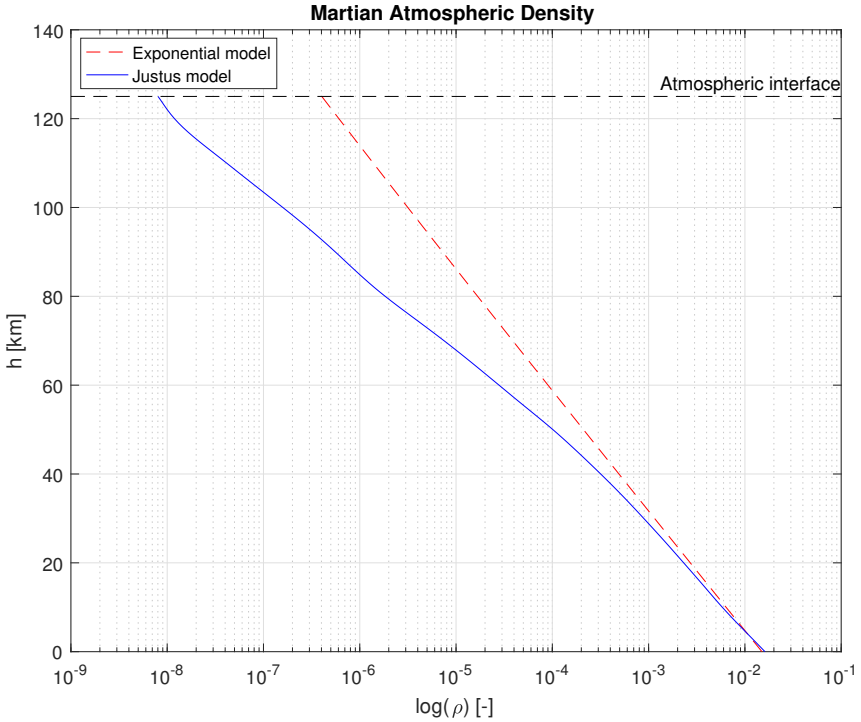

FIGURE 2.3. Comparison between the exponential model and Justus [10] model for the Martian atmosphere

For what concerns the atmospheric chemistry, the composition is considered not changing with the altitude. Thus, properties are constant and they are summarized in Table 2.2.

$c_{p_{atm}}$ [J/(kg K)]	R_{atm} [J/(kg K)]	γ_{atm} [-]
819	189	1.3

TABLE 2.2. Mars atmosphere properties

2.4 Heating rates

In aerocapture, the orbital energy is lowered converting it in thermal energy, thanks to the interaction with the atmosphere. For this reason, heating rates represent one of the major issues for this kind of maneuver. Also the selection and design of TPS is of paramount importance, in order to correctly manage the thermal load. For aerocapture maneuver, the more appropriate choice is a classical ablative material [42].
Furthermore, a fully catalytic spacecraft surface is assumed. This is a conservative approach given that the heating rate can be lower if this assumption is not verified.
For capsule-like vehicles, only the stagnation heating rate is considered, both radiative and convective [26], that is

$$\dot{q} = \dot{q}_{conv} + \dot{q}_{rad} \tag{2.13}$$

Its value is used then to compute the TPS mass.

2.4.1 Heating rates model

The convective stagnation point heating rate is computed using the Marvin-Deiwert model [37]

$$\dot{q}_{conv} = k_0 \left(\frac{\rho}{r_n}\right)^{\frac{1}{2}} V^{3.04} \left(1 - \frac{h_w}{H}\right) \tag{2.14}$$

with k_0 that is a constant, equal to 1.35×10^{-8} for Mars, h_w is the wall enthalpy and H is the total enthalpy. Assuming to have radiative equilibrium, the latter are computed as

$$h_w = c_{p_{TPS}} T_w \qquad \text{with} \quad T_w = \left(\frac{\dot{q}}{\sigma_{SB}\varepsilon}\right)^{\frac{1}{4}}$$

and

$$H = c_{p_{atm}} T_{atm} \left(1 + \frac{\gamma_{atm} - 1}{2} M^2\right)$$

where σ_{SB} is the Stefan-Boltzmann constant, ε the TPS surface emissivity, T_{atm} is the atmospheric temperature given by the atmosphere model and $M = \frac{V}{\sqrt{\gamma_{atm} R_{atm} T_{atm}}}$ is the Mach number.
The radiative stagnation point heating rate is computed using the Tauber-Sutton model [38]

$$\dot{q}_{rad} = C r_n^a \rho^b f(V) \tag{2.15}$$

For the Martian environment, the constant in Eq. (2.15) are

$$C = 2.35 \times 10^{-4}, \quad a = 0.526 \quad \text{and} \quad b = 1.19$$

Instead $f(V)$ is a tabulated value dependent on velocity and its magnitude can be found in [38].
Both the relations (2.14) and (2.15) give results in W/cm^2.
It can be seen, starting from Eq. (2.13) and (2.14), that the total heating rate is described by an implicit function, and it is impossible to write an explicit relation for $\dot{q}$. Thus, some problems arise and they are faced in Chapter 5.

2.4.2 TPS selection

In the equations describing the heat loads, thermal and optical properties of the thermal protection system are needed. For this reason, a TPS selection is required.
Since in the atmospheric phase, the heating rate experienced is expected to be the same of previous missions on Mars, a classical ablative TPS is chosen. This technology was used by NASA in most the Entry, Descent and Landing missions and aerocapture studies [42] and so it is a well known and proved thermal protection.
As is understandable, the interaction between ablative TPS and the surrounding environment is very complex, as well as the processes undergone the heat transfer. An ablative heat shield works cooling down the boundary layer, through two different mechanisms: when the TPS is heated up, the outer layers char, melt and finally sublimate, while the inner layers decompose due to pyrolysis, producing some gases. These gases percolate through the external surface, removing some heat from the heat shield and altering the boundary layer properties, typically reducing the heat transfer by convection. Also radiation is reduced: the gases produced by pyrolysis introduce carbon in the boundary layer, making it optically opaque. (For more details see [27]).
As the thermal protection system is subjected to melting and decomposition, it loses

mass. Thus, the mass of the spacecraft is reduced as it passes through the atmosphere. In this study, this effect is neglected assuming that the mass loss is small with respect to the total mass of the spacecraft.

Among the different ablative material, SLA-561V is selected. Produced by Lockheed Martin[1], it is a widespread technology for 70° sphere-cone vehicle for Mars missions: only Mars Science Laboratory (better known as *Curiosity*) has used a different TPS material. SLA-561V is characterized by $c_{p_{TPS}} = 1260\ \mathrm{J\,kg^{-1}\,K^{-1}}$ and $\varepsilon = 0.97$.

The last point related to TPS is the estimation of its mass. This is of paramount importance for the following mass optimization. As shown in [11], historical data on previous NASA missions give a direct relation between the TPS mass fraction and the integrated total heat load q (Figure 2.4). Basing on this connection, the mass of the TPS is estimated using the formula given by the fit curve in Figure 2.4 (in blue), whose analytic expression is

$$\frac{m_{TPS}}{m_0} = Kq^{\beta} \tag{2.16}$$

with $K = 0.091$ and $\beta = 0.51575$.

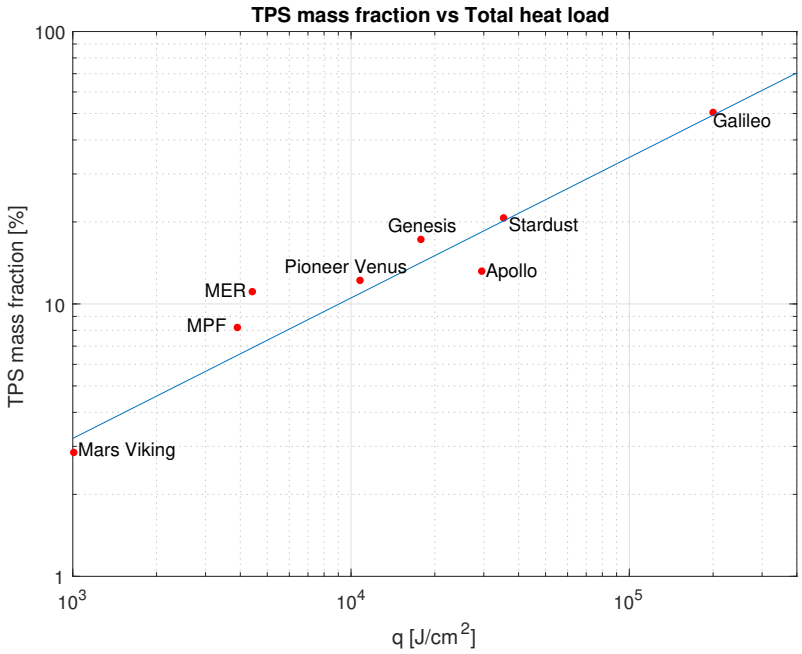

FIGURE 2.4. TPS mass fraction and total heat load for previous missions with ablative heat shield [11]

[1] LOCKHEED-MARTIN, SLA-561 Product Informations, Retrieved on: 2017/03/28

CHAPTER 3

BALLISTIC CAPTURE MODELING

Some models describing the ballistic trajectory are presented in this chapter. Their selection is based always on a compromise between accuracy and computational resources.
They are used to describe the dynamics of the vehicle outside the atmosphere, where the motion of the spacecraft is driven only by gravitational force of celestial bodies.

3.1 Elliptic Restricted Three-Body Problem

The *Elliptic Restricted Three-Body problem* (ER3BP) is a generalization of the *Circular Restricted Three-Body problem* (CR3BP), which is deeply analyzed in literature. This problem studies the planar motion of a third massless body P, attracted by two primaries, P_1 and P_2, of mass m_1 and m_2 respectively, revolving one around the other in an elliptic motion.
It was shown in [20] that the elliptic problem describes quite accurately the dynamics of the Solar System. For this reason together with the fact that Mars orbit eccentricity is not negligible (~ 0.1), this model is used for the non-atmospheric phase.
A non-uniformly rotating, barycentric, adimensional reference frame ($\hat{\xi}$, $\hat{\eta}$, $\hat{h}$), called *synodic frame*, is defined in order to write the equation of motion for P. The center of this system is placed at the primaries barycenter; the $\hat{\xi}$ axis is aligned with the two primaries, with $\hat{h}$ orthogonal to the plane of motion. In this frame, P_1 and P_2 have fixed position (-μ, 0) and (1-μ, 0) respectively, with $\mu = m_2/(m_1 + m_2)$, being the mass parameter of

the system (see Figure 3.1). Moreover, the distances are normalized accordingly to the distance between P_1 and P_2.

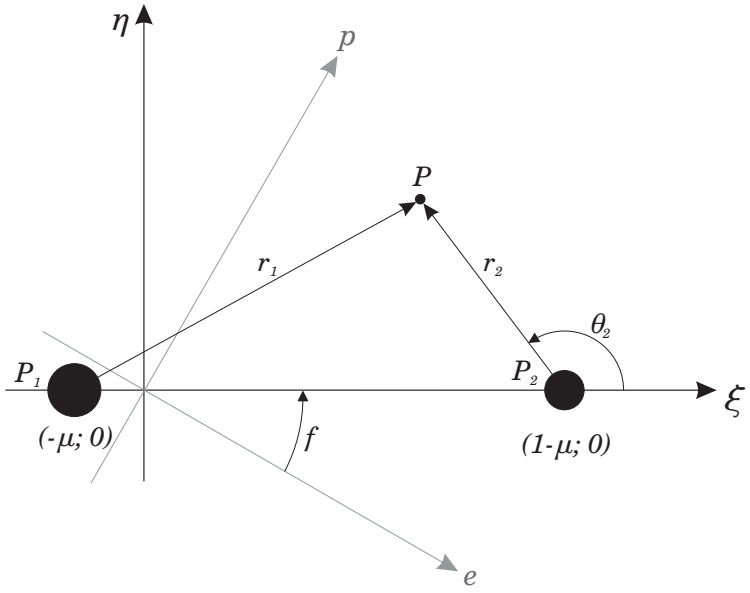

FIGURE 3.1. Rotating, pulsating, non-inertial reference frame with polar coordinates. The inertial sidereal perifocal reference frame is drawn in gray.

Defining e_p the eccentricity of the ellipses described by the two primaries around the barycenter, the unit distance can be defined as

$$r_{ref} = \frac{a_p(1-e_p^2)}{1+e_p\cos f}$$

where f is the true anomaly of the system and a_p the primary semi-major axis. Therefore, r_{ref} varies in time according to the mutual position of the two primaries, so creating a pulsating reference system.

The true anomaly f represents the independent variable of the system, playing the role of the time, making the system non-autonomous. If the period of revolution of the system P_1-P_2 is set equal to 2π, the link between f and time can be written in differential form as

$$\frac{\mathrm{d}f}{\mathrm{d}t} = \frac{\left(1+e_p\cos f\right)^2}{\left(1-e_p^2\right)^{3/2}} \tag{3.1}$$

In this framework, it is possible to write the equations of motion for the third body as (see [35]):

$$\begin{aligned} \xi'' - 2\eta' &= \omega_\xi \\ \eta'' + 2\xi' &= \omega_\eta \end{aligned} \tag{3.2}$$

with the primes representing the derivatives with respect to f and the subscripts the partial derivatives of

$$\omega(\xi,\eta,f) = \frac{\Omega(\xi,\eta)}{1+e_p\cos f} \tag{3.3}$$

where Ω is the potential function, defined as

$$\Omega(\xi,\eta) = \frac{1}{2}(\xi^2+\eta^2) + \frac{1-\mu}{r_1} + \frac{\mu}{r_2} + \frac{1}{2}\mu(1-\mu) \tag{3.4}$$

and $r_1 = \sqrt{(\xi+\mu)^2+\eta^2}$ and $r_2 = \sqrt{(\xi+\mu-1)^2+\eta^2}$ are the distances of P from the primaries.

For the Sun–Mars three-body problem used in this work, the main parameters are presented in Table 3.1.

μ [-]	a_p [AU]	e_p [-]
3.226208×10^{-7}	1.523688	0.093418

TABLE 3.1. Sun–Mars Three-Body problem parameters

3.1.1 Polar coordinates

Beside the synodic reference frame, the three body problem can be described using polar coordinates, centered at P_2. If r_2 is defined as the magnitude of the vector from P_2 to the third body and θ_2 is the angle between the $\hat{\xi}$ axis and this vector (see Figure 3.1), P moves under the dynamics described by [8]

$$\begin{aligned} r_2'' - r_2\theta_2'^2 - 2r_2\theta_2' &= \frac{1}{1+e_p\cos f}\left[r_2\left(1-\frac{1-\mu}{r_1^3}\right) - \frac{\mu}{r_2^2} + (1-\mu)\cos\theta_2\left(1-\frac{1}{r_1^3}\right)\right] \\ r_2\theta_2'' + 2r_2'\theta_2' + 2r_2' &= \frac{(1-\mu)\sin\theta_2}{1+e_p\cos f}\left(\frac{1}{r_1^3}-1\right) \end{aligned} \tag{3.5}$$

with $r_1 = \sqrt{r_2^2+2r_2\cos\theta_2+1}$.

Since that these equations involve trigonometric functions, they are more expensive from the computational point of view, but allow to write more easily the initial and final conditions and are able to provide a smooth function for θ_2 in dependence of f.

3.1.2 Energetic considerations

Some important energetic considerations can be made by manipulating the equations of motion. In fact, starting from Eqs. (3.2), an integral of motion, dependent on f can be found [8]. It reads

$$J_E(\xi,\eta,\xi',\eta',f) = 2\omega - \left(\xi'^2+\eta'^2\right) - 2e_p\int_{f_0}^{f}\frac{\Omega\sin\hat{f}}{\left(1+e_p\cos\hat{f}\right)^2}\,\mathrm{d}\hat{f} \tag{3.6}$$

Given the energy value C, it is possible to define the anomaly-dependent manifold as

$$\mathscr{J}_E(C,f) = \left\{(\xi,\eta,\xi',\eta')\in\mathbb{R}^4 | J_E(\xi,\eta,\xi',\eta',f) - C = 0\right\} \tag{3.7}$$

Defining a value for C, Eq. (3.7) describes the Hill's curves, that are the boundaries of Hill's regions. Since there is a dependence not only on C but also on f, both in ω and in the integral, the Hill's curves are not steady, but they vary on time, showing a pulsating behavior, so generating *pulsating Hill's regions*. Thus, forbidden and allowed zones for a given level of energy vary according to $P_1 - P_2$ mutual position. An in-dept analysis about energy level in ER3BP and relation with ballistic capture can be found in [9].

3.1.3 Circular Restricted Three-Body Problem

The CR3BP can be retrieved from the ER3BP, setting $e_p = 0$. In this case, Eq. (3.1) becomes simply $d/df = d/dt$ and Eq. (3.3) yields $\omega = \Omega$. Inserting these results in Eqs. (3.2), the dynamics are

$$\begin{aligned}\ddot{\xi} - 2\dot{\eta} &= \Omega_\xi\\ \ddot{\eta} + 2\dot{\xi} &= \Omega_\eta\end{aligned} \tag{3.8}$$

Furthermore, $e_p = 0$ in Eq. (3.6) yields the classic Jacobi integral for the circular problem comes out

$$J_C(\xi,\eta,\dot{\xi},\dot{\eta}) = 2\Omega - \left(\dot{\xi}^2+\dot{\eta}^2\right) \tag{3.9}$$

Given an energy C, starting from this integral of motion, the Hill's curves definition in the circular problem can be recalled as

$$\mathscr{J}_C(C) = \left\{(\xi,\eta,\dot{\xi},\dot{\eta})\in\mathbb{R}^4 | J_C(\xi,\eta,\dot{\xi},\dot{\eta}) - C = 0\right\} \tag{3.10}$$

Differently from the ones of the elliptic problem, the zero-velocity curves in the circular problem are steady, since there is no explicit dependence on the independent variable.

3.1.4 Lagrangian points

A last useful consideration can be made by analyzing the equilibrium points of this system. By definition, it is possible to find them setting to zero accelerations and velocities in Eqs. (3.2), that means

$$\nabla\omega = \mathbf{0} \tag{3.11}$$

Solving the two equations given by Eq. (3.11), five equilibrium points are found. They are called Lagrangian points, indicated with the symbol L_k, where $k \in \{1, \dots, 5\}$. Their position is fixed in the pulsating, non-inertial frame, so the relative location with respect to the primaries does not change, but the real distance from P_1 and P_2 changes according to the system true anomaly. Lagrange points are shown in Figure 3.2: L_1, L_2 and L_3 are collinear points, lying on the $\hat{\xi}$ axis, and L_4 and L_5 are placed at the vertex of equilateral triangles with the base equal to the segment $P_1 - P_2$.

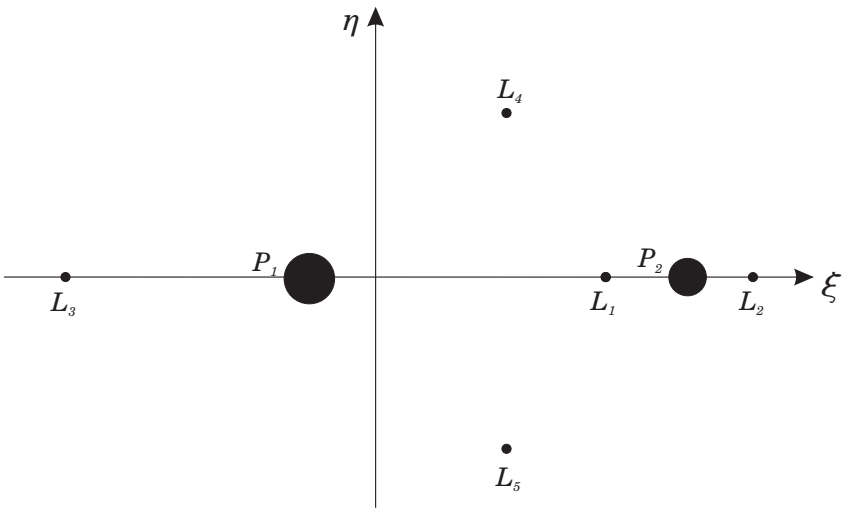

FIGURE 3.2. Lagrange points location (not in scale)

3.2 Sun gravitational assist

Since this work studies orbits around Mars, in order to better understand the dynamics of the massless body P, an investigation about the effects related to the Sun gravity field near to the *Red Planet* is required.
How the orbits change due to the perturbation of the Sun is of interest. For this reason, first of all, the solar gravity gradient field near Mars is analyzed, without taking into

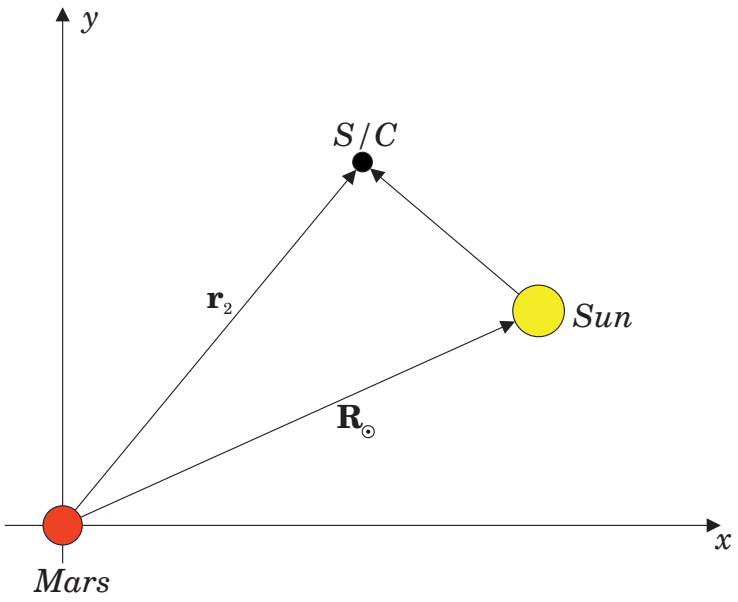

FIGURE 3.3. Solar gravity gradient reference figure.

account the presence of the planet. So, with reference to Figure 3.3, the definition of the gravity acceleration can be written as

$$\mathbf{g}_{SUN} = \frac{\mu_{\odot}}{\|\mathbf{R}_{\odot} - \mathbf{r}_2\|^3} \begin{bmatrix} (\mathbf{R}_{\odot} - \mathbf{r}_2) \cdot \hat{x} \\ (\mathbf{R}_{\odot} - \mathbf{r}_2) \cdot \hat{y} \end{bmatrix} \tag{3.12}$$

then neglecting the higher order terms, the gradient can be defined [2]

$$\nabla \mathbf{g}_{SUN} = \begin{bmatrix} \frac{\partial}{\partial x}(\mathbf{g}_{SUN} \cdot \hat{x}) \\ \frac{\partial}{\partial y}(\mathbf{g}_{SUN} \cdot \hat{y}) \end{bmatrix} = \frac{\mu_{\odot}}{R_{\odot}^3} \begin{bmatrix} \left(3\hat{R}_{\odot_x}^2 - 1\right) x \\ \left(3\hat{R}_{\odot_y}^2 - 1\right) y \end{bmatrix} \tag{3.13}$$

where $\hat{R}_{\odot_x} = (\mathbf{R}_{\odot} \cdot \hat{x})/\|\mathbf{R}_{\odot}\|$ and $\hat{R}_{\odot_y} = (\mathbf{R}_{\odot} \cdot \hat{y})/\|\mathbf{R}_{\odot}\|$.
The Sun gravity gradient vector field is showed in Figure 3.4, where the length of the arrows is proportional to its strength. It is clear that the farther is the third body from the planet, the strongest is the effect of the Sun, but for different angular positions with respect to Mars, a different effect is attained, since the field lines change direction. In fact, considering prograde orbits, if the apocenter is in the second or fourth quadrant, a raising in orbital energy or angular momentum is obtained, since the tangential component of the gravity force and the tangential velocity are in the same direction; otherwise, in the first and third quadrant, the Sun gravity slows down the vehicle, removing energy from its orbit. (See Figure 3.5). The same effect can be studied, analyzing the change in angular momentum, as showed in [43]. In fact, it is possible to define the angular

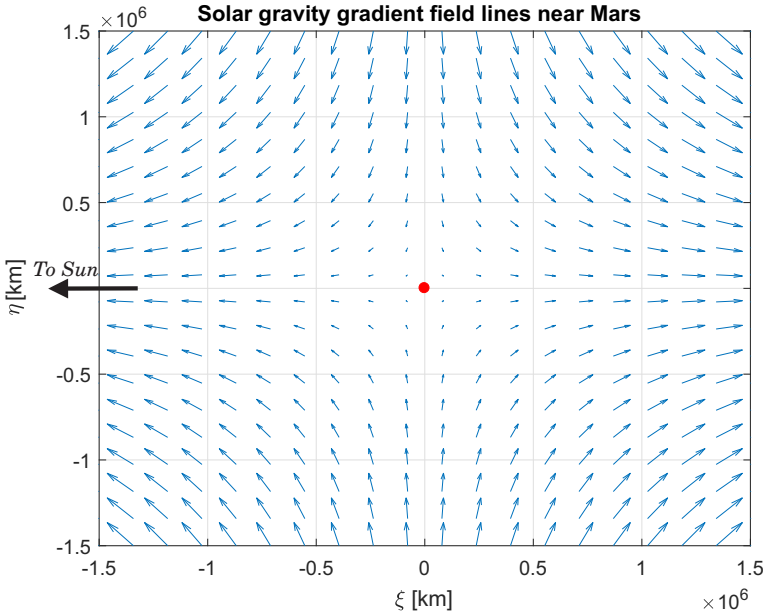

FIGURE 3.4. Solar gravity gradient field lines near Mars. The red dot indicates Mars position.

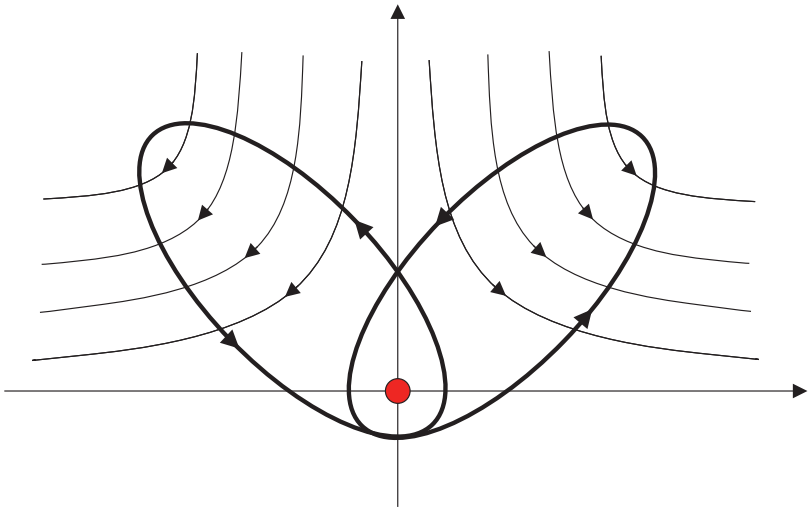

FIGURE 3.5. Solar gravity gradient field effect on orbits near Mars. In the II quadrant tangential velocity and Solar gravity field lines are in the same direction. In the I quadrant they have opposite directions.

momentum vector magnitude with respect to the smaller primary in the P_2-centered polar coordinates as [35]

$$h_{P_2} = r_2^2 + r_2^2\dot{\theta}_2 \tag{3.14}$$

It is possible to compute the variation of h_{P_2} deriving it with respect to time, obtaining that

$$\dot{h}_{P_2} = 2\dot{r}_2 r_2 + 2\dot{r}_2 r_2 \frac{\mathrm{d}\theta_2}{\mathrm{d}t} + r_2^2 \ddot{\theta}_2 \tag{3.15}$$

Using the Eqs. (3.5) in this last expression, setting $e_p = 0$, the angular momentum variation reads [43]

$$\dot{h}_{P_2} = r_2(1-\mu)\sin\theta_2 \left[\frac{1}{\left(r_2^2 + 2r_2\cos\theta_2 + 1\right)^{3/2}} - 1 \right] \tag{3.16}$$

In Figure 3.6, the adimensional angular momentum variation is plotted. Also in this case, an increase in angular momentum can be found in the second and in the fourth quadrant. In those locations, h_{P_2} increases and it means that the semi-major axis with respect to the smaller primary is enlarged or the eccentricity is reduced. If orbits close to P_2 are considered, only the second effect has a major importance. Thus, if the apocenter of an orbit around P_2 is in the second or in the fourth quarter, a raising in the pericenter is expected.

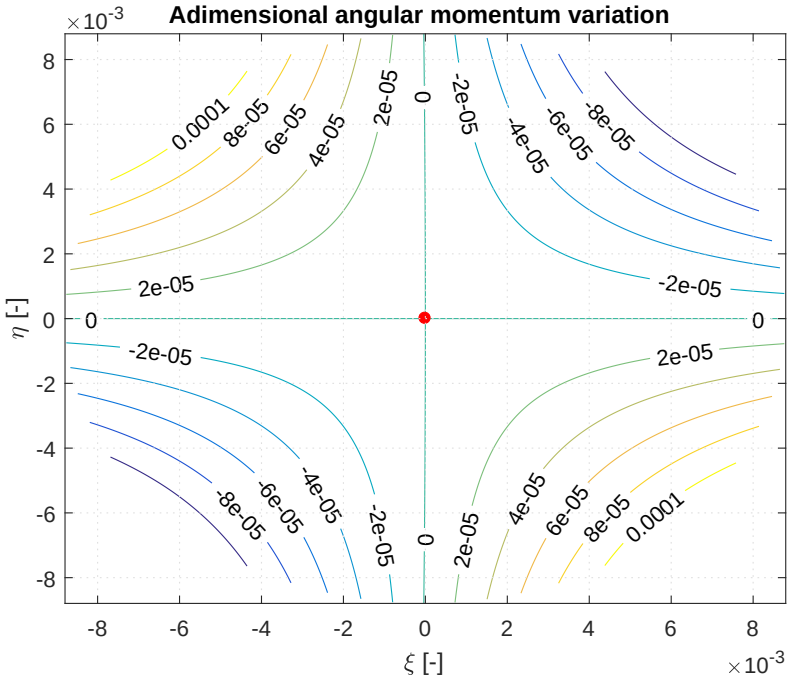

FIGURE 3.6. Adimensional angular momentum variation near Mars. The red dot indicates Mars position. Positive values can be found only in II and IV quadrant.

3.2.1 Sun gravitational assist in ER3BP

If the elliptic problem is taken in account, instead of the simpler circular problem, some quantities change and moreover it is possible to study the effect of true anomaly of the primaries on the Sun gravitational assist.
The first step is the analysis of the solar gravity gradient. For the ER3BP, the distance of Mars with respect to the Sun varies in time, so it means that, in the Eq. (3.13), $R_\odot$ is no more constant, but it has to be defined as

$$R_\odot = \frac{a_p\left(1-e_p^2\right)}{1+e_p\cos f} \tag{3.17}$$

So a dependence from true anomaly appears. Since this quantity is at the denominator, the solar influence is the strongest when $(1+e_p\cos f)$ is the highest. Thus, the solar gravitational assist is more effective at the pericenter of the Sun–Mars orbit, when $\cos f$ is at its maximum.
The same result can be found studying the angular momentum variation with respect to P_2. In fact, using polar coordinates, it is possible to write the position of a body in non-inertial P_2-centered frame as

$$\mathbf{r} = \begin{bmatrix} r_\xi \\ r_\eta \end{bmatrix} = \begin{bmatrix} r_2\cos(\theta_2) \\ r_2\sin(\theta_2) \end{bmatrix} \tag{3.18}$$

and the velocity as

$$\mathbf{v} = \begin{bmatrix} v_\xi \\ v_\eta \end{bmatrix} = \begin{bmatrix} r_2'\cos(\theta_2) - r_2\theta_2'\sin(\theta_2) \\ r_2'\sin(\theta_2) + r_2\theta_2'\cos(\theta_2) \end{bmatrix} \tag{3.19}$$

Now, defining as f the true anomaly, two rotation matrices and two reference quantities can be described. They are, respectively:

$$T_f = \begin{bmatrix} \cos f & -\sin f \\ \sin f & \cos f \end{bmatrix}$$

$$T_f' = \begin{bmatrix} -\sin f & -\cos f \\ \cos f & -\sin f \end{bmatrix}$$

and

$$r_f = \frac{1-e_p^2}{1+e_p\cos f}$$

$$r'_f = \frac{(1-e_p^2)e_p \sin f}{(1+e_p \cos f)^2}$$

Recalling the link between time and true anomaly given by Eq. (3.1), it is possible to define the state in inertial P_2-centered reference frame computing

$$\mathbf{R} = r_f T_f \mathbf{r} \tag{3.20}$$

$$\mathbf{V} = \frac{\mathrm{d}f}{\mathrm{d}t}\left[r_f T_f \mathbf{v} + \left(r'_f T_f + r_f T'_f\right)\mathbf{r}\right] \tag{3.21}$$

And, in conclusion, the angular momentum respect to P_2 can be evaluated through

$$h_{P_2} = \mathbf{R} \times \mathbf{V} \tag{3.22}$$

and so, for the elliptic problem, it reads

$$h_{P_2} = \sqrt{\left(1-e_p^2\right)}\left(r_2^2 + r_2^2\theta'_2\right) \tag{3.23}$$

This quantity is expressed as a scalar, since a planar motion is considered.
Again, in order to see variations, the derivative with respect to time is performed, finding that

$$\dot{h}_{P_2} = \frac{\mathrm{d}h}{\mathrm{d}f}\frac{\mathrm{d}f}{\mathrm{d}t} = \sqrt{\left(1-e_p^2\right)}\left(2r_2 r'_2 + 2r_2 r'_2\theta'_2 + r_2^2\theta''_2\right)\frac{\mathrm{d}f}{\mathrm{d}t} \tag{3.24}$$

Using Eqs. (3.5) together with Eq. (3.1), it can be written that

$$\dot{h}_{P_2} = r_2(1-\mu)\sin\theta_2\left[\frac{1}{\left(r_2^2 + 2r_2\cos\theta_2 + 1\right)^{3/2}} - 1\right]\frac{1+e_p\cos f}{1-e_p^2} \tag{3.25}$$

Also in that case, the angular momentum has its maximum when $f = 0$ and so the result is, as seen before, that the solar gravity assist is the strongest when the two primaries are as close as possible.

CHAPTER 4

AERO-BALLISTIC CAPTURE MODELING

In this chapter modeling of aero-ballistic capture is discussed.
The strategy used to merge aerocapture with ballistic capture follows this path:

1. At the beginning, the spacecraft approaches Mars with an hyperbolic trajectory with pericenter inside the atmosphere;
2. The probe pass through the atmosphere and some orbital energy is dissipated by aerodynamic drag and converted into heat;
3. At the exit, at the atmospheric interface, the vehicle is on a closed orbit, but with a very high apocenter, such that the effects of solar gravity cannot be neglected;
4. The Sun gravity field accelerates the probe when it is far from Mars and, thus, the pericenter is naturally raised and taken out from the atmosphere, at the desired altitude;
5. Finally, at the pericenter of this transfer orbit a propelled impulse is given in order to reduce the velocity and so lowering the apocenter to a prescribed value.

Thus, the aero-ballistic capture can be divided into four phases:

1. *Approaching phase*: the spacecraft arrives at target planet on an incoming hyperbola;

2. *Atmospheric phase*: the spacecraft is on a controlled trajectory inside the atmosphere. It is slowed down thanks to atmospheric friction;

3. *Ballistic phase*: the spacecraft is on a ballistic, low-energy orbit with a very high apocenter. Orbital energy and so the pericenter are increased thanks to interaction with solar gravity field;

4. *Final orbit*: a firing is performed at the pericenter, bringing the spacecraft on the final orbit.

Figure 4.1 shows the different phases of the aero-ballistic capture.

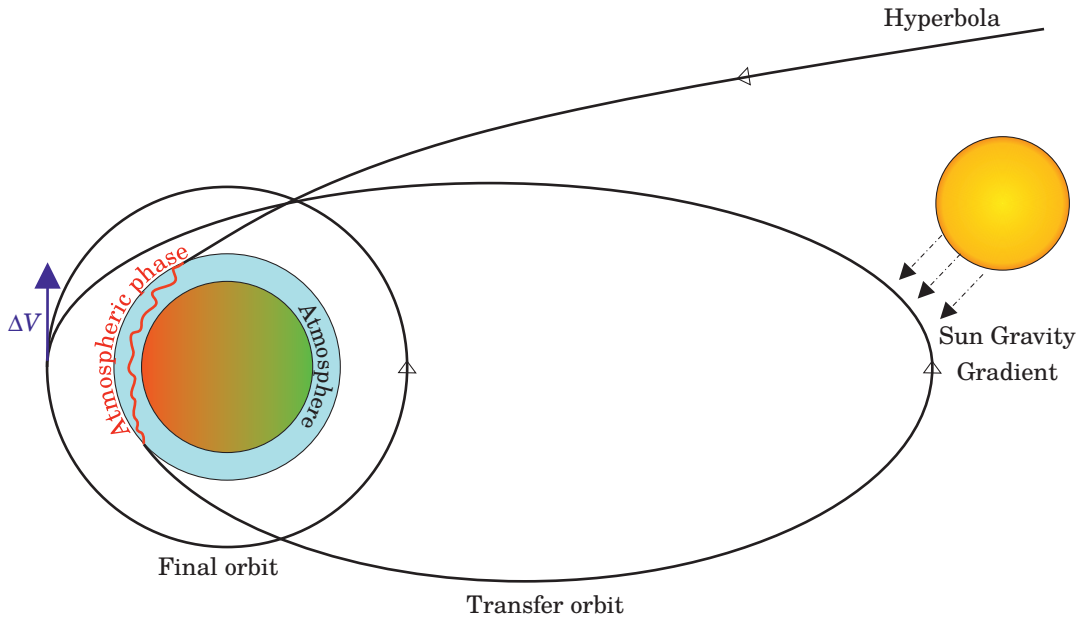

FIGURE 4.1. The different phases of aero-ballistic capture: the spacecraft arrives on a *hyperbola*; then the *atmospheric phase* (in red) brings the vehicle on a very elliptic transfer orbit; during the *ballistic phase* the solar gravity gradient raises the pericenter (dotted arrows); a propelled maneuver is performed (in blue) moving the probe to the *final orbit*.

This strategy may allow potential mass savings, since the passage through the atmosphere is used to dissipate less energy than a classic aerocapture and, so, the TPS is lighter. Moreover, the propelled maneuver is performed at the pericenter, and not at the apocenter, and this reduces the fuel consumption thanks to the Oberth effect. On the other hand, this kind of maneuver lowers the TOF with respect to the ballistic capture

and provides a simple mechanism for stabilization of the orbit.
Now, the different phases are analyzed and modeled one by one.

4.1 Approaching phase

In this leg, high-energy orbits are involved, so the decomposition of the Solar System in two-body problems is possible. After a direct transfer from the Earth, the spacecraft enters in the *Sphere of Influence* of Mars and follows an hyperbolic trajectory up to the atmospheric interface. The heliocentric orbit on which the probe is in this phase is not of interest in this work and, thus, it is not analyzed.
The characterization of this trajectory can be done in several and easy ways, since a simply analytic solution exists; in the remainder, it is described using state variables at the atmospheric boundary. Taking as reference previous studies about aerocapture at Mars [40], a $V_0 = 5900\ \mathrm{m\,s^{-1}}$ and a $\gamma_0 = -9.7°$ are chosen, where the subscript 0 is used to indicate the interface conditions.

4.2 Atmospheric phase

When the probe reaches the atmosphere, the atmospheric phase begins. During this leg, the only one where there is control, the dynamics of the vehicle is described by the differential equations given in the Section 2.2.2. For the sake of clarity, they are

$$\dot{r} = V \sin\gamma \tag{4.1}$$

$$\dot{V} = -D - \frac{\mu_{♂}}{r^2} \sin\gamma \tag{4.2}$$

$$\dot{\gamma} = \frac{1}{V}\left[L\cos\sigma + \left(V^2 - \frac{\mu_{♂}}{r}\right)\frac{\cos\gamma}{r}\right] \tag{4.3}$$

In this study, the lateral dynamics is not considered. In further developments, a targeted post-atmospheric orbital inclination can be implemented considering it; in that case, only the sign of σ will be affected, with multiple bank reversals during the atmospheric flight. Since that the guidance algorithm is beyond the scope of this work, this problem will be not faced. In this thesis, the spacecraft is assumed to be always on the Mars orbital plane at the exit from the atmosphere.
Furthermore, the bank reversal is considered to occur instantaneously.

Also for this problem, thermal loads are of paramount importance; so, for this reason, the heating rate, described by the implicit equation

$$\dot{q} = k_0 \left(\frac{\rho}{r_n}\right)^{\frac{1}{2}} V^{3.04} \left(1 - \frac{c_{p_{TPS}} \left(\frac{\dot{q}}{\sigma_{SB}\varepsilon}\right)^{\frac{1}{4}}}{H}\right) + C r_n^a \rho^b f(V) \tag{4.4}$$

derived in Section 2.4, is added to the ODEs system (4.1)–(4.3). This equation depends on position and velocity inside the atmosphere, but does not influence the other variables. So, in principles, it can be integrated a posteriori. It is possible for this phase to define an augmented state vector $\mathbf{x} = [r,\ V,\ \gamma,\ q]$.
The phase ends when the probe reaches the interface with the open space, that means when $r(t_{out}) = r_{interface}$.

4.3 Ballistic phase

In the ballistic phase, after the passage through the atmosphere, the spacecraft is on an orbit under natural dynamics. So, no control is performed.
Since the probe follows a low energy trajectory, the two-body problem no longer represent correctly the equations of motion. For this reason, the ER3BP is used to describe the dynamics, with the Sun and Mars as primaries. The motion is considered to be completely in Mars orbital plane. In the adimensional, non-inertial, pulsating reference frame, with Mars-centered polar coordinates, the probe follows the motion described by

$$\begin{aligned} r_2'' - r_2\theta_2'^2 - 2r_2\theta_2' &= \frac{1}{1+e_p\cos f}\left[r_2\left(1-\frac{1-\mu}{r_1^3}\right) - \frac{\mu}{r_2^2} + (1-\mu)\cos\theta_2\left(1-\frac{1}{r_1^3}\right)\right] \\ r_2\theta_2'' + 2r_2'\theta_2' + 2r_2' &= \frac{(1-\mu)\sin\theta_2}{1+e_p\cos f}\left(\frac{1}{r_1^3} - 1\right) \end{aligned} \tag{4.5}$$

with $r_1 = \sqrt{r_2^2 + 2r_2\cos\theta_2 + 1}$.
Even if it is computationally intensive, polar representation gives the possibility to write easily the final conditions for the ballistic phase. In fact, the integration has to be stopped at the pericenter of the transfer orbit, that means that

$$\begin{cases} r_2'(f_{fin}) = -\frac{r_2 e_p \sin f_{fin}}{1+e_p\cos f_{fin}} \\ r_2''(f_{fin}) < 0 \end{cases} \tag{4.6}$$

with f_{fin} that is the final true anomaly for the primaries. The first final condition represents an instant where there is no radial velocity with respect to Mars (the radial

velocity is only related to the non-inertial frame) and so it represents the condition at an apsis. Otherwise, the second one allows to select the pericenter instead of the apocenter, since indicates a moment when the radial velocity is decreasing.

4.3.1 From atmospheric phase to ballistic phase

The initial conditions for the ballistic phase are the final conditions of the atmospheric phase. So, an overview about the conversion between these two systems is required.
In this work, from now on, capital letters are associated to perifocal dimensional reference frame. Conversely lower case letters indicate quantities in non-intertial reference frame.
First of all, position and velocity have to be placed in a Mars-centered inertial frame, since from the first integration only the magnitude of this quantities are computed. Defining α as the angle between the ER3BP perifocal axis and the spacecraft position vector at the end of the atmospheric phase (see Figure 4.2), the state of the probe can be defined as

$$\begin{aligned} \mathbf{R} &= \begin{bmatrix} R_{e'} \\ R_{p'} \end{bmatrix} = \begin{bmatrix} r(t_{out})\cos\alpha \\ r(t_{out})\sin\alpha \end{bmatrix} \\ \mathbf{V} &= \begin{bmatrix} V_{e'} \\ V_{p'} \end{bmatrix} = \begin{bmatrix} V(t_{out})\cos\left(\alpha+\gamma(t_{out})-\pi/2\right) \\ V(t_{out})\sin\left(\alpha+\gamma(t_{out})-\pi/2\right) \end{bmatrix} \end{aligned} \tag{4.7}$$

with r, V and γ the state variables in the previous phase and t_{out} the time at the exit from the atmosphere.

Then a *scaling* is performed, dividing the positions by a_p and the velocities by $\sqrt{\mu_\odot/a_p}$, that is the first cosmic velocity for an orbit of radius a_p around the Sun.
Now, defining f_0 as the true anomaly when the spacecraft exits the atmosphere, the conversion from the Mars-centered inertial perifocal reference frame to the synodic one can be done. Two rotation matrices and two reference quantities are described, the firsts for the positions and the others for the velocities. They are, respectively:

$$T_f = \begin{bmatrix} \cos f_0 & -\sin f_0 \\ \sin f_0 & \cos f_0 \end{bmatrix}$$

$$T'_f = \begin{bmatrix} -\sin f_0 & -\cos f_0 \\ \cos f_0 & -\sin f_0 \end{bmatrix}$$

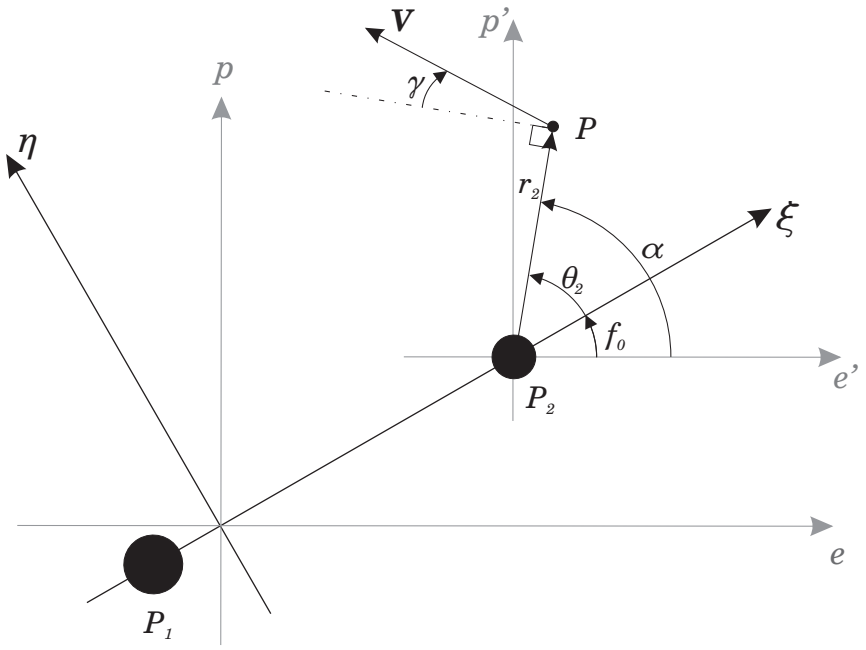

FIGURE 4.2. Definition of α and initial true anomaly. Synodic (in black) and perifocal (in grey) reference frames are reported.

and

$$r_f = \frac{1-e_p^2}{1+e_p\cos f_0}$$

$$r'_f = \frac{(1-e_p^2)e_p\sin f_0}{(1+e_p\cos f_0)^2}$$

Recalling the link between time and true anomaly given by Eq. (3.1), the state in synodic frame can be computed as

$$\mathbf{r} = \begin{bmatrix} r_\xi \\ r_\eta \end{bmatrix} = \frac{1}{r_f} T_f^T \mathbf{R} - \begin{bmatrix} \mu - 1 \\ 0 \end{bmatrix} \tag{4.8}$$

$$\mathbf{v} = \begin{bmatrix} v_\xi \\ v_\eta \end{bmatrix} = \frac{1}{r_f} T_f^T \left[\left(\frac{\mathrm{d}f}{\mathrm{d}t} \right)^{-1} \mathbf{V} - \left(T_f r'_f + T'_f r_f \right) \left(\mathbf{r} + \begin{bmatrix} \mu - 1 \\ 0 \end{bmatrix} \right) \right] \tag{4.9}$$

As last point, conversion form Cartesian coordinates to polar coordinates is needed. Thus, in conclusion, the initial conditions for ER3BP for ballistic phase are retrieved from the

final conditions of atmospheric phase writing

$$
\begin{aligned}
r_2(f_0) &= \sqrt{(r_\xi + \mu - 1)^2 + r_\eta^2} \\
\theta_2(f_0) &= \operatorname{atan2}\left(\frac{r_\eta}{r_2}\,,\quad \frac{r_\xi + \mu - 1}{r_2}\right) \\
r_2'(f_0) &= v_\xi \cos\theta_2 + v_\eta \sin\theta_2 \\
\theta_2'(f_0) &= \frac{1}{r_2}\left(v_\eta \cos\theta_2 - v_\xi \sin\theta_2\right)
\end{aligned}
\tag{4.10}
$$

4.3.2 Mathematical characterization

In the ballistic phase, the spacecraft is subjected to pure natural dynamics, because there is no control. This means that, given the initial conditions, the vehicle follows a predetermined path. For this reason, it can be convenient to describe the conversions and the integration associated to this leg using a map $\mathscr{M}$. This function takes as inputs the atmosphere exit conditions $(r,\ V,\ \gamma)$ plus the parameters f_0, relative to the time when the elliptic problem is solved, and α; uses them to find the state in Mars-centered polar coordinates in synodic reference frame; then integrates from f_0 up to the true anomaly f_{fin} when the conditions in Eq. (4.6) are found; so, the pericenter velocity conditions are directly implemented in the map. Using backward the algorithm in Subsection 4.3.1, the outputs, that are position and velocity at the end of integration in Mars-centered inertial coordinates, are retrieved. A wrap-up scheme for this map is:

$$
\begin{bmatrix} r \\ V \\ \gamma \end{bmatrix}_{t_{out}} \xrightarrow{\alpha} \begin{bmatrix} \mathbf{R} \\ \mathbf{V} \end{bmatrix}_{t_{out}} \xrightarrow{f_0} \begin{bmatrix} \mathbf{r} \\ \mathbf{v} \end{bmatrix}_{f_0} \longmapsto \begin{bmatrix} r_2 \\ r_2' \\ \theta_2 \\ \theta_2' \end{bmatrix}_{f_0} \xrightarrow{\int} \begin{bmatrix} r_2 \\ r_2' \\ \theta_2 \\ \theta_2' \end{bmatrix}_{f_{fin}} \longmapsto \begin{bmatrix} \mathbf{r} \\ \mathbf{v} \end{bmatrix}_{f_{fin}} \xrightarrow{f_{fin}} \begin{bmatrix} \mathbf{R} \\ \mathbf{V} \end{bmatrix}_{t_{fin}}
$$

In conclusion, it is possible to write

$$
\begin{bmatrix} \mathbf{R} \\ \mathbf{V} \end{bmatrix}_{t_{fin}} = \mathscr{M}_{\alpha,\, f_0}\left(r,\ V,\ \gamma\right)_{t_{out}} \tag{4.11}
$$

4.4 Final orbit

After the maneuver at pericenter, a desired closed orbit around the planet is obtained. Since this orbit has a quite high energy and it is relatively close to Mars, a simple two-body problem, with Mars as primary, is considered. So the final orbit is studied using

the simple analytic formulas for two-body problem.
This means that it is possible to compute the pericenter velocity of this final orbit writing

$$v_p^* = \sqrt{2\mu_{\male}} \sqrt{\frac{1}{r_p^*} - \frac{1}{r_p^* + r_a^*}} \tag{4.12}$$

where r_p^* is the desired final pericenter and r_a^* is the desired final apocenter.
Starting from this, since $\mathbf{V}(t_{fin})$ is tangential to the orbit by construction, the needed maneuver impulse can be evaluated as

$$\Delta V = v_p^* - \left\| \mathbf{V}\left(t_{fin}\right) \right\| \tag{4.13}$$

CHAPTER 5

AERO-BALLISTIC CAPTURE OPTIMIZATION

The *optimal problem* both for aerocapture and aero-ballistic capture is to find the control solution that minimizes an objective function. Since the aim for all space missions is to maximize the scientific return, this objective function is

$$J = -m_{fin} \tag{5.1}$$

where the minus is imposed in order to obtain a minimum instead of a maximum.
Now, two discrete events contribute to change in the mass value:

1. Ejection of the TPS;
2. Engine burn needed to go to the final orbit.

Thus, defining as m_{out} the mass of the spacecraft when the heat shield is jettisoned, it is possible to write

$$m_{fin} = m_0 \frac{m_{out}}{m_0} \frac{m_{fin}}{m_{out}} \tag{5.2}$$

where m_0 is the initial mass.
Recalling Eq. (2.16) and Tsiolkovsky rocket equation, since $m_{out} = m_0 \left(1 - \frac{m_{TPS}}{m}\right)$,

$$m_{fin} = m_0 \left[1 - Kq^{\beta}(t_{out})\right] e^{-\frac{\Delta V}{I_{sp} g_0}} \tag{5.3}$$

In conclusion, the objective function can be defined as

$$J = -m_0 \left[1 - Kq^{\beta}(t_{out})\right] e^{-\frac{\Delta V}{I_{sp} g_0}} \tag{5.4}$$

This function is equal for both problems, but the definition of some variables is different. So, from now on, the optimization problem will be discussed separately.

5.1 Aerocapture optimization

In this work, aerocapture optimization is studied for two main reasons: first of all, unlike previous studies, the cost function is not only the ΔV; on the other hand, a comparison between aerocapture and aero-ballistic capture has to be made and so it is necessary to work under the same framework for both the problems.
Denoting the state $\mathbf{x} = [r,\ V,\ \gamma,\ q]$, for aerocapture, the optimal problem is to minimize the cost function

$$J = J(\mathbf{x}(t_{out}))$$

described by Eq. (5.4), with

$$\Delta V = \sqrt{2\mu_{\sun}}\left(\sqrt{\frac{1}{r_a^*} - \frac{1}{r_a^* + r_p^*}} - \sqrt{\frac{1}{r_a*} - \frac{1}{2a}}\right) \tag{5.5}$$

where r_a^* is the desired apoapsis, r_p^* the desired periapsis and the semi-major axis defined as

$$a = \frac{\mu_{\sun}}{2\mu_{\sun}/r(t_{out}) - V^2(t_{out})} \tag{5.6}$$

Therefore, the cost function depends only on the final state, so $J = \varphi(\mathbf{x}(t_{out}))$. State is subjected to the dynamic system

$$\dot{\mathbf{x}} = \mathbf{f}(\mathbf{x})$$

defined by Eqs. (4.1)–(4.4), with the control variable σ, subjected to magnitude constraints $0 \leq \sigma_{min} \leq |\sigma| \leq \sigma_{max} \leq \pi$.
Furthermore, the terminal constraint, describing the *apoapsis targeting*,

$$r_a = r_a^* \tag{5.7}$$

has to be satisfied, where

$$r_a = a\left(1 + \sqrt{1 - \frac{V^2(t_{out}) r^2(t_{out}) \cos^2\gamma(t_{out})}{\mu_{\sun} a}}\right) \tag{5.8}$$

is the apoapsis determined by the exit conditions.
Defining the Hamiltonian of the system as

$$H = \boldsymbol{\lambda}^T \mathbf{f} \tag{5.9}$$

where $\boldsymbol{\lambda}$ is the costate varablies vector, by the Maximum Principle [29], the optimal control is found from the optimality condition

$$\begin{aligned}\sigma = \arg\max \Bigg[& \lambda_r V \sin\gamma + \lambda_V \left(-D - \frac{\mu_{\male} \sin\gamma}{r^2} \right) + \\ & + \lambda_\gamma \left(\frac{L}{V} \cos\sigma + \left(V^2 - \frac{\mu_{\male}}{r} \right) \frac{\cos\gamma}{rV} \right) + \lambda_q f_q \Bigg]\end{aligned} \tag{5.10}$$

where f_q is an hypothetic explicit function describing the heat flux dynamics. Although it can be easily proved that it is impossible to write an explicit function for $\dot{q}$, the *Implicit Function theorem* can be used to prove the existence of that f_q.
Eq. (4.4) defines an implicit function $g(r, V, \dot{q}) = 0$. This function is continuously differentiable and it can be used to compute $\dot{\tilde{q}}$ for each given couple $(\tilde{r}, \tilde{V})$ describing the trajectory. Furthermore,

$$\frac{\partial g}{\partial \dot{q}}(r, V, \dot{q}) = 1 + k_0 \left(\frac{\rho}{r_n} \right)^{\frac{1}{2}} V^{3.04} c_{P_{TPS}} \left(\frac{1}{4\varepsilon\sigma \left(\frac{\dot{q}}{\sigma\varepsilon} \right)^{\frac{3}{4}} H} \right) \neq 0, \qquad \forall\ (r, V, \dot{q})$$

Thus, it is possible to assume the existence of an explicit function $\dot{q} = f_q(r,\ V)$, such that $f_q(\tilde{r}, \tilde{V}) = \dot{\tilde{q}},\ \forall\ (\tilde{r}, \tilde{V})$, even if it cannot be written explicitly.
Coming back to Eq. (5.10), since L/V is always positive and $\cos\sigma$ has a monotonic behavior in the interval $[\sigma_{min},\ \sigma_{max}] \in [0,\ \pi]$, the optimal bank angle is determined only by the sign of λ_γ; so

$$\sigma^* = \begin{cases} \sigma_{min} & \text{if } \lambda_\gamma > 0 \\ \sigma_{max} & \text{if } \lambda_\gamma < 0 \\ \in [\sigma_{min},\ \sigma_{max}] & \text{if } \lambda_\gamma = 0 \text{ in } [t_1,\ t_2] \end{cases} \tag{5.11}$$

The last case in Eq. (5.11) is called *singular optimal control*. If that condition is verified, the bank angle can assume a time-varying value in the interval $[\sigma_{min},\ \sigma_{max}]$. Otherwise, the control variable can be only σ_{max} or σ_{min} alternatively and so the control has a bang-bang structure.

5.1.1 Singular control in aerocapture

An analysis about the possibility of singular control is now needed.
Starting from Eq. (5.9), the Hamiltonian can be written in expanded form as

$$H = \lambda_r V \sin\gamma + \lambda_V \left(-D - \frac{\mu_{\male} \sin\gamma}{r^2} \right) + \lambda_\gamma \left(\frac{L}{V} \cos\sigma + \left(V^2 - \frac{\mu_{\male}}{r} \right) \frac{\cos\gamma}{rV} \right) + \lambda_q f_q \tag{5.12}$$

where the costate variables have to satisfy the equations

$$\dot{\lambda}_r = -\frac{\partial H}{\partial r} = \lambda_V \left(\frac{\partial D}{\partial r} - \frac{2\mu_{\male} \sin\gamma}{r^3} \right) - \lambda_\gamma \frac{\partial f_\gamma}{\partial r} - \lambda_q \frac{\partial f_q}{\partial r} \tag{5.13}$$

$$\dot{\lambda}_V = -\frac{\partial H}{\partial V} = -\lambda_r \sin\gamma + \lambda_V \frac{\partial D}{\partial V} - \lambda_\gamma \frac{\partial f_\gamma}{\partial V} - \lambda_q \frac{\partial f_q}{\partial V} \tag{5.14}$$

$$\dot{\lambda}_\gamma = -\frac{\partial H}{\partial \gamma} = -\lambda_r V \cos\gamma + \lambda_V \frac{\mu_{\male} \cos\gamma}{r^2} - \lambda_\gamma \frac{\partial f_\gamma}{\partial \gamma} \tag{5.15}$$

$$\dot{\lambda}_q = -\frac{\partial H}{\partial q} = 0 \tag{5.16}$$

where f_γ is the right-hand side of the Eq. (4.3).
Assuming by contradiction that the singular control exists, this means that $\lambda_\gamma = 0$ and $\dot{\lambda}_\gamma = 0$ in time interval $[t_1,\ t_2] \subset [t_0,\ t_{out}]$, due to its definition. Simplifying Eq. (5.15) using these last assumptions, assuming that $\cos\gamma \neq 0$, it is found that

$$\lambda_r = \frac{\mu_{\male}}{r^2 V} \lambda_V \tag{5.17}$$

Then, by Maximum Principle, the relation

$$H = 0 \qquad \forall t \in [t_0,\ t_{out}] \tag{5.18}$$

has to hold on the optimal trajectory. This means, remembering that $\lambda_\gamma = 0$, that Eq. (5.9) becomes

$$\lambda_r V \sin\gamma - \lambda_V D - \lambda_V \frac{\mu_{\male} \sin\gamma}{r^2} + \lambda_q f_q = 0 \tag{5.19}$$

Inserting the Eq. (5.17) in this last expression, the result is

$$-\lambda_V D + \lambda_q f_q = 0 \tag{5.20}$$

Assuming that $\lambda_q \neq 0$, it is possible to write that

$$f_q = \frac{\lambda_V}{\lambda_q} D \tag{5.21}$$

Using this in Eqs. (5.13) and (5.14), the costate dynamics becomes

$$\dot{\lambda}_r = -\frac{2\mu_{\male} \sin\gamma}{r^3} \lambda_V \tag{5.22}$$

$$\dot{\lambda}_V = -\lambda_r \sin\gamma \tag{5.23}$$

Now, starting from Eq. (5.17), the expression

$$\lambda_V = \frac{r^2 V}{\mu_{\male}} \lambda_r \tag{5.24}$$

can be retrieved and, differentiating it with respect to the time, yields

$$\dot{\lambda}_V = \frac{1}{\mu_{\male}} \left(2r\dot{r}V\lambda_r + r^2 \dot{V}\lambda_r + \dot{\lambda}_r r^2 V \right) \tag{5.25}$$

Putting Eq. (5.22) and the dynamics equations inside this equation, the result is

$$\dot{\lambda}_V = \frac{1}{\mu_{\male}} \left[2rV^2 \sin\gamma\lambda_r + r^2 \left(-D - \frac{\mu_{\male} \sin\gamma}{r^2} \right) \lambda_r - \frac{2\mu_{\male} \sin\gamma}{r^3} r^2 V \lambda_V \right] \tag{5.26}$$

that can be simplified using Eq. (5.17), becoming

$$\dot{\lambda}_V = \left(-\frac{Dr^2}{\mu_{\male}} - \sin\gamma \right) \lambda_r \tag{5.27}$$

This last equation has an extra non-null term with respect to Eq. (5.23) . The only way to have Eq. (5.23) consistent with Eq. (5.27) is that $\lambda_r = 0$.
This means that also $\lambda_V = 0$. And, consequentially, $f_q = 0$; but this is a non-sense.
Otherwise, if $\lambda_q = 0$, Eq. (5.20) is simply

$$-\lambda_V D = 0 \rightarrow \lambda_V = 0 \tag{5.28}$$

since $D \neq 0$ always in the trajectory. But $\lambda_V = 0$ together with Eq. (5.17) indicates that $\lambda_r = 0$. Therefore, the costate vector $\boldsymbol{\lambda} = [\lambda_r,\ \lambda_V,\ \lambda_\gamma,\ \lambda_q]^T = \mathbf{0}$ in $[t_1,\ t_2]$. Since that the costate equations are affine in $\boldsymbol{\lambda}$ and $\boldsymbol{\lambda}$ is continuous in $[t_0,\ t_{out}]$, it follows that $\boldsymbol{\lambda} = \mathbf{0}, \quad \forall t \in [t_0,\ t_{out}]$; but this is not possible because it is in contradiction with the Maximum Principle that states that the costate vector cannot be null.
Thus, the possibility to have a singular optimal control in this problem is ruled out.

5.1.2 Conclusions for control in aerocapture

Starting from the conclusions in previous paragraphs, it is possible to state that the control has a bang-bang structure. Numerical simulations in [25] show that for a classical aerocapture problem with ΔV minimization the vehicle flies nearly full lift up, then almost full lift down. Extending this result to this work, the control profile is the one in Figure 5.1: from t_0 up to a switching time t_s the bank angle is small and equal to σ_0;

then, from t_s to the atmosphere exit the control variable is equal to σ_d.
Of course, a full-lift down trajectory is also possible, if in the optimization process a switching time equal to 0 is obtained. Conversely, full-lift up cases can be found when t_s is higher with respect to the atmospheric exit time.
As showed in [19], performances are not affected by the value of σ_0. For this reason, a fixed value of 5° is selected for the initial bank angle.
So, at the end, the optimal aerocapture problem is to find the values of the parameters σ_d and t_s that minimize $J = J(\mathbf{x}(t_{out}))$, subjected to $\dot{\mathbf{x}} = \mathbf{f}(\mathbf{x})$ and $r_a = r_a^*$.
This result is valid not only for aerocapture, but it can be simply extended to all the aeroassist optimal problems that respect the assumptions:

1. The cost function depends only on the final value of the state $\mathbf{x}(t_{out})$;
2. The bank angle σ is the only control variable.

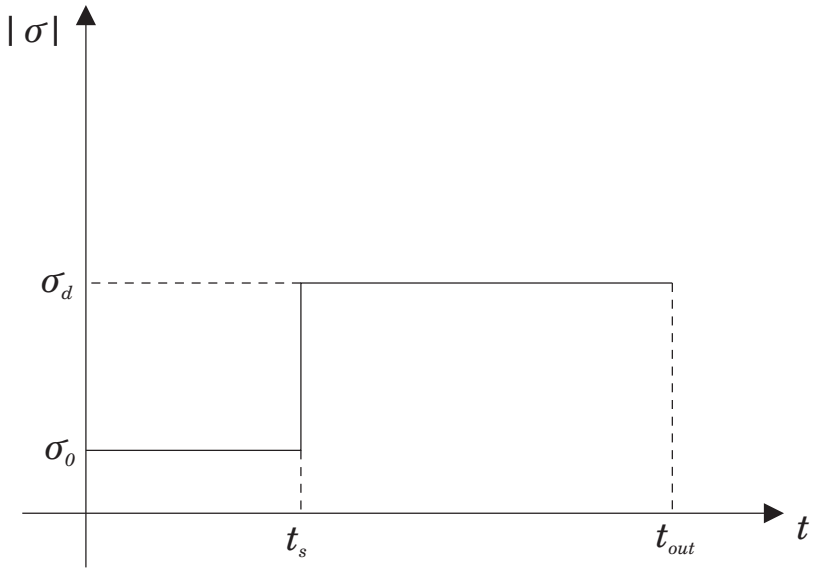

FIGURE 5.1. Optimal bank angle profile

5.2 Aero-ballistic capture optimization

For aero-ballistic capture, the objective is to find the control function that minimize

$$J = -m_0 \left[1 - Kq^{\beta}(t_{out})\right] e^{-\frac{\Delta V}{I_{sp} g_0}} \tag{5.29}$$

such that

$$\left\|\mathbf{R}\left(t_{fin}\right)\right\| = r_p^* \tag{5.30}$$

and with

$$\Delta V = v_p^* - \left\|\mathbf{V}\left(t_{fin}\right)\right\| \tag{5.31}$$

where $\begin{bmatrix}\mathbf{R}\\ \mathbf{V}\end{bmatrix}_{t_{fin}} = \mathscr{M}_{\alpha,\, f_0}\left(r,\, V,\, \gamma\right)_{t_{out}}$ and v_p^* is the velocity at the pericenter of the final orbit and it can be computed as

$$v_p^* = \sqrt{2\mu_{\sphericalangle}}\sqrt{\frac{1}{r_p^*} - \frac{1}{r_p^* + r_a^*}} \tag{5.32}$$

State $\mathbf{x} = [r,\, V,\, \gamma,\, q]$ is subjected, as the aerocapture, to the dynamics system

$$\dot{\mathbf{x}} = \mathbf{f}(\mathbf{x})$$

defined by Eqs. (4.1)–(4.4), with the bank-angle σ as control variable, subjected to magnitude constraints $0 \leq \sigma_{min} \leq |\sigma| \leq \sigma_{max} \leq \pi$.
So, it is possible to state that the cost function

$$J = \varphi(\mathbf{x}(t_{out}),\, \alpha,\, f_0) \tag{5.33}$$

depends only on the value of the final state and on the parameters α and f_0.
In [29], Pontryagin describes how to deal with problems with the cost function dependent not only on the state, but also on some constant parameters. In this case, a conversion from the Problem of Mayer to the Problem of Lagrange is needed [17].
That is

$$J = \varphi(\mathbf{x}(t_{out}),\, \alpha,\, f_0) \quad \rightarrow \quad J = \int_{t_0}^{t_{out}} \frac{\mathrm{d}\varphi}{\mathrm{d}t}\,\mathrm{d}t \quad \text{with } \varphi(\mathbf{x}(t_0),\, \alpha,\, f_0) = 0 \tag{5.34}$$

An augmented state vector is then defined as

$$\tilde{\mathbf{x}} = \left[\varphi,\, \mathbf{x}\right]^T \tag{5.35}$$

allowing to define the Hamiltonian of the problem as

$$H = \lambda_0 \dot{\varphi} + \boldsymbol{\lambda}^T \mathbf{f} \tag{5.36}$$

Therefore, by Maximum Principle the optimal bank angle can be found solving

$$\sigma = \arg\max \left[\lambda_0 \frac{\varphi}{\mathrm{d}t} + \lambda_r V \sin\gamma + \lambda_V \left(-D - \frac{\mu_{\sun} \sin\gamma}{r^2} \right) + \right. \\ \left. + \lambda_\gamma \left(\frac{L}{V} \cos\sigma + \left(V^2 - \frac{\mu_{\sun}}{r} \right) \frac{\cos\gamma}{rV} \right) + \lambda_q f_q \right] \tag{5.37}$$

with f_q the local explicit function associated to the heat load dynamics, as explained in the previous section.

Now, as before, since σ appears only in the term $\cos\sigma$, associated to λ_γ, having a monotonic behavior in the existence interval, and $L/V > 0$ always, the optimal bank angle is again determined only by the sign of the costate associated to the flight path angle and, thus, as in Eq. (5.11) for aerocapture,

$$\sigma^* = \begin{cases} \sigma_{min} & \text{if } \lambda_\gamma > 0 \\ \sigma_{max} & \text{if } \lambda_\gamma < 0 \\ \in [\sigma_{min},\ \sigma_{max}] & \text{if } \lambda_\gamma = 0 \text{ in } [t_1,\ t_2] \end{cases} \tag{5.38}$$

The last case in Eq. (5.38) is a *singular optimal control*. If that condition happens, the control variable can assume any value inside the interval $[\sigma_{min},\ \sigma_{max}]$ and the bang-bang structure is no more valid. For this reason, an analysis is required.

5.2.1 Singular control in aero-ballistic capture

The Hamiltonian of the system in expanded form is

$$H = \lambda_0 \dot{\varphi} + \lambda_r V \sin\gamma + \lambda_V \left(-D - \frac{\mu_{\sun} \sin\gamma}{r^2} \right) + \\ + \lambda_\gamma \left(\frac{L}{V} \cos\sigma + \left(V^2 - \frac{\mu_{\sun}}{r} \right) \frac{\cos\gamma}{rV} \right) + \lambda_q f_q \tag{5.39}$$

and the costate variables have to satisfy Eqs. (5.13)–(5.16), plus a new ODE that is

$$\dot{\lambda}_0 = -\frac{\partial H}{\partial \varphi} = -\lambda_0 \frac{\partial \dot{\varphi}}{\partial \varphi} = 0 \tag{5.40}$$

Since the cost function depends on some parameters, some additional transversal conditions have to be added and they are

$$\boldsymbol{\lambda}(t_{out})^T \int_{t_0}^{t_{out}} \frac{\partial \mathbf{f}}{\partial \alpha} \mathrm{d}t = 0 \tag{5.41}$$

and

$$\boldsymbol{\lambda}(t_{out})^T \int_{t_0}^{t_{out}} \frac{\partial \mathbf{f}}{\partial f_0} \mathrm{d}t = 0 \tag{5.42}$$

Since only the objective function depends on the parameters, some simplifications can be made. In fact, Eq. (5.41) becomes

$$\lambda_0(t_{out})\int_{t_0}^{t_{out}} \frac{\partial \dot{\varphi}}{\partial \alpha}\,\mathrm{d}t = 0 \quad \rightarrow \quad \lambda_0(t_{out})\frac{\partial}{\partial \alpha}\int_{t_0}^{t_{out}} \frac{\mathrm{d}\varphi}{\mathrm{d}t}\,\mathrm{d}t = 0 \quad \rightarrow \tag{5.43}$$

$$\lambda_0(t_{out})\frac{\partial \varphi(t_{out})}{\partial \alpha} = 0$$

where the property that α is constant and does not depend on time is used.
A similar reasoning can be done for Eq. (5.42), obtaining the condition

$$\lambda_0(t_{out})\frac{\partial \varphi}{\partial f_0} = 0 \tag{5.44}$$

The only way that satisfies these two last equations is $\lambda_0(t_{out}) = 0$ and due to Eq. (5.40)

$$\lambda_0 \equiv 0 \quad \forall t \in [t_1,\ t_2] \tag{5.45}$$

From now on, passages made in Subsection 5.1.1 can be performed, bringing to the conclusion that, also for aero-ballistic capture optimization, the singular optimal control is pruned out.

5.2.2 Conclusions for control in aero-ballistic capture

Also in aero-ballistic capture the optimal control has a bang-bang structure. First the vehicle flies full lift up with a small bank angle σ_0; then from the switching time t_0 to t_{out} the spacecraft changes its attitude, flying nearly full lift down, with the control variable equal to σ_d. As in aerocapture, a fixed value of 5 deg is considered for σ_0, since this value does not change the performances.
In conclusion, the optimal aero-ballistic capture problem is to find the values of σ_d, t_s, α and f_0, minimizing the cost function.

5.3 Nonlinear Programming Problem statement

Starting from conclusions in the previous section, the optimal problem for aero-ballistic capture can be translated in a *Nonlinear Programming Problem*.
In this case, the aim is to find σ_d, t_s, α and f_0 that minimize the cost function

$$J = \varphi(\mathbf{x}(t_{out}),\ \alpha,\ f_0) = -m_0\left[1 - Kq^{\beta}(t_{out})\right]e^{-\frac{\Delta V}{I_{sp}g_0}} \tag{5.46}$$

with

$$\Delta V = v_p^* - \left\| \mathbf{V}\left(t_{fin}\right) \right\| \tag{5.47}$$

such that

$$\dot{\mathbf{x}} = \begin{bmatrix} \dot{r} \\ \dot{V} \\ \dot{\gamma} \\ \dot{q} \end{bmatrix} = \begin{bmatrix} V \sin\gamma \\ -D - \frac{\mu_{\male}}{r^2} \sin\gamma \\ \frac{1}{V}\left[L\cos\sigma + \left(V^2 - \frac{\mu_{\male}}{r} \right) \frac{\cos\gamma}{r} \right] \\ f_q(r, V) \end{bmatrix} \tag{5.48}$$

where f_q is the explicit function describing the heat flux and with the bank angle

$$\sigma = \begin{cases} \sigma_0 & \text{when } t_0 < t \leq t_s \\ \sigma_d & \text{when } t_s < t < t_{out} \end{cases}$$

where t_{out} is the time when $r = r_{interface}$, subjected to the final constraint

$$\left\| \mathbf{R}\left(t_{fin}\right) \right\| = r_p^* \tag{5.49}$$

where

$$\begin{bmatrix} \mathbf{R} \\ \mathbf{V} \end{bmatrix}_{t_{fin}} = \mathscr{M}_{\alpha,\, f_0}\left(r,\, V,\, \gamma\right)_{t_{out}} \tag{5.50}$$

with t_{fin} the time when the conditions

$$\begin{cases} \mathbf{V}\left(t_{fin}\right) \cdot \mathbf{R}\left(t_{fin}\right) = 0 \\ \left\| \mathbf{V}\left(t_{fin}\right) \cdot \mathbf{R}\left(t_{fin}\right) \right\| < 0 \end{cases} \tag{5.51}$$

directly implemented in the map $\mathscr{M}$, are attained. These last conditions are the translation in P2-centered reference frame of the Eqs. (4.6).
In addition, some inequality path constraints are included both on the load factor and on the dynamic pressure, in order to avoid too high stresses on the structure, and also on the heating rate and the total heat load. These are:

$$\begin{aligned} n = \sqrt{L^2 + D^2} &\leq n_{max} \\ \bar{q} = \frac{1}{2}\rho V^2 &\leq \bar{q}_{max} \\ \dot{q} &\leq \dot{q}_{max} \\ q\left(t_{out}\right) &\leq q_{max}\left(t_{out}\right) \end{aligned} \tag{5.52}$$

with $n_{max} = 2.3$ g, $\bar{q}_{max} = 4600$ Pa, $\dot{q}_{max} = 460\ \mathrm{W\,cm^{-2}}$ and $q_{max}(t_{out}) = 70\ \mathrm{kJ\,cm^{-2}}$, as in [24].

5.4 Numerical techniques

An overview on how the problem is effectively solved is now required. Thus the numerical techniques adopted are presented in this section, with a particular focus on the motivations underneath the selection.
The analysis will be carried out step by step, in a descending way, starting from the most "external" function.

5.4.1 Minimization

In Nonlinear Programming Problems, the choice of the minimization algorithm is of paramount importance, since a wrong selection will lead to sub-optimal solutions. For this reason, a first study on how the cost function behaves modifying the variables is carefully performed, paying attention also to the pericenter distance constraint. This last value is considered through a logarithmic relative error, defined as

$$r^*_{p_{err}} = \log_{10}\left(\left|\frac{\left\|\mathbf{R}\left(t_{fin}\right)\right\| - r^*_p}{r^*_p}\right|\right)$$

Figures 5.2 and 5.3, obtained evaluating J varying some optimization parameters, show that the cost function has multiple basins of attraction, leading a local solver to find non-optimal local minima. Some of them have also an high error on the final constraint, as showed by the surface color. Moreover, the objective function varies widely, even when there is only a small change in variables. In conclusion, this one is a multi-modal problem and a local optimizer will be not able to find a global optimal solution.

Starting from this observation, a method to find global or multiple minima is required. The choice fell on the *MultiStart* algorithm, that in numerical experiments effectively is able to sample the multiple basins of attraction, seek for the lowest minimum and, so, for the optimal solution.
The idea behind this approach is quite simple: some initial points are randomly generated inside a feasible domain and then they are used as initial points of a local solver. In this way, several local optimizations are performed and, eventually, the best solution in term of cost function is recorded and stored. Parallel computing is implemented, allowing to distribute start points to different cores, so reducing the time needed for computation.
The local solver has to be a constrained nonlinear optimization algorithm, that allows both nonlinear equality constraints and path inequality constraints. Furthermore, a large-scale algorithm can be useful since the cost function has an high nonlinearity and, so, using sparse matrices, memory and computational resources can be saved. Due

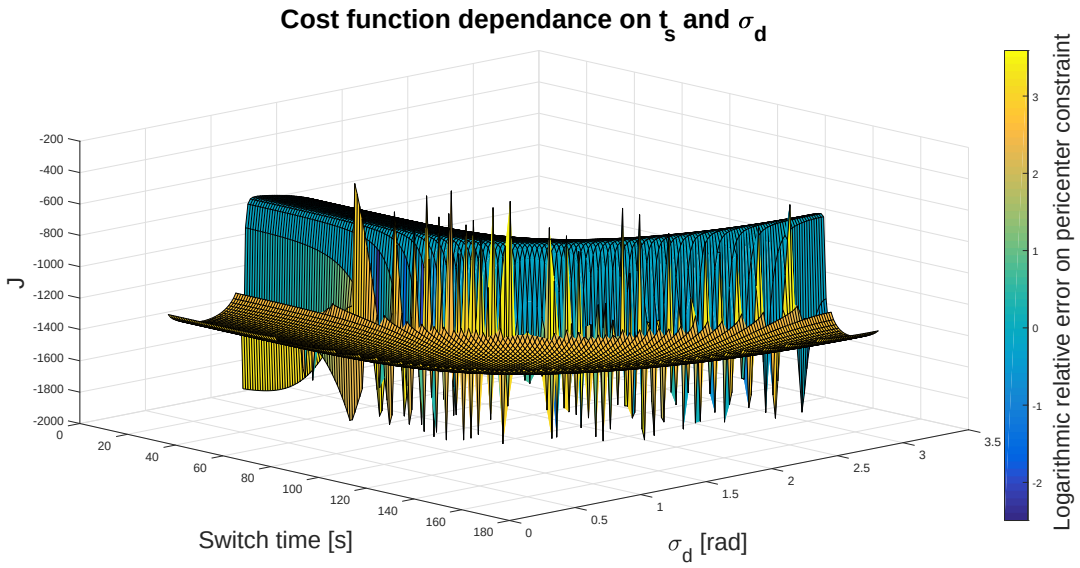

FIGURE 5.2. Cost function in dependence of t_s and σ_d. Surface colors are related to the logarithmic relative error of final constraint.

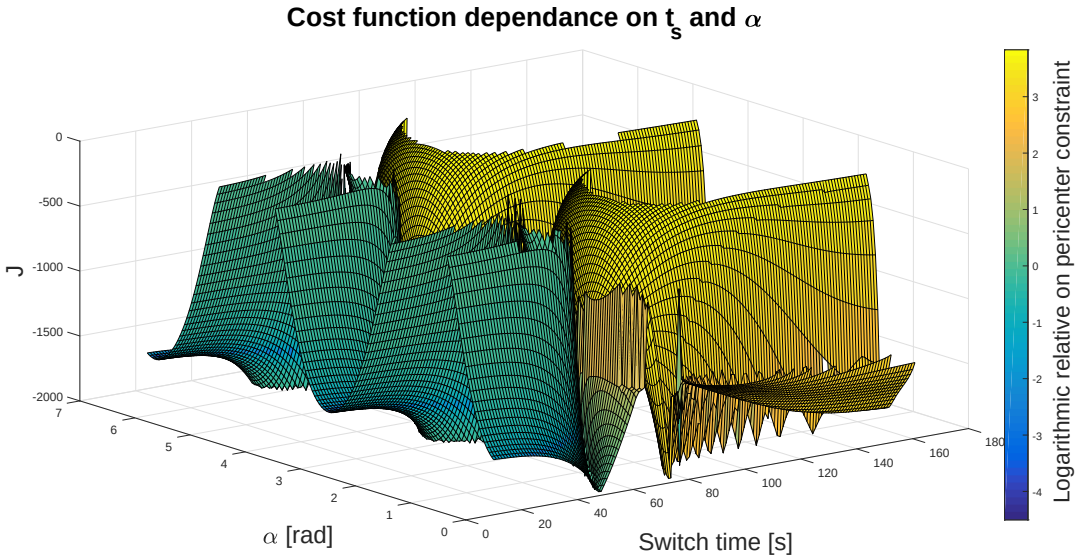

FIGURE 5.3. Cost function in dependence of t_s and α. Surface colors are related to the logarithmic relative error of final constraint.

to these motivations, the *interior point* method is selected. Tests were performed also using other algorithms. This assessment showed that interior point is the best choice, as

showed in Table 5.1. In fact, it is the one giving the higher number of feasible solutions and the best result in term of cost function. Analysis on the running times (performed on a PC with Intel i7@2.20GHz and 16 GB of RAM) shows that it is also quite fast. Just for sake of completeness, the *thrust region reflective* algorithm cannot be used, since it is impossible to provide analytically the gradient of the objective function.

Algorithm	CPU time [min]	J	n_{sol}
Interior point	23	-1655	8
Sequential quadratic programming	26	-	0
Active set	45	-	0
Sequential quadratic programming - legacy	20	-1649	2

TABLE 5.1. Local optimization algorithms comparison, with areostationary orbit as final orbit. Last column shows the number of feasible solutions found out of 20 runs.

The minimization is performed imposing as inequality constraints the ones in Eq. (5.52) and as equality constraint the pericenter distance at final time, as written in Eq. (5.49); the pericenter velocity conditions are handled using a different logic, as explained in Subsection 4.3.2.
Furthermore, boundaries on minimization variables are set, in order to properly pick the initial points in the *MultiStart* algorithm, avoiding unreasonable conditions and exploiting periodicity of some variables; they are

$$\begin{cases} 0 \leq t_s \leq 200 \\ 0 \leq \sigma_d \leq \pi \\ 0 \leq \alpha \leq 2\pi \\ 0 \leq f_0 \leq 2\pi \end{cases} \tag{5.53}$$

The boundary on switching time is selected after some numerical investigations. Boundaries on angles are used actually only on initial points and not during minimization.
A check on trajectories crashing on Mars surface is also made: if this event occurs, the cost function is imposed to be equal to 0 and this makes sure that the local solver avoids these situations.

5.4.2 Integration

The other major numerical issue in this Nonlinear Programming Problem is related to the integration of the ordinary differential equations both for the atmospheric phase and for the ballistic phase. A versatile and accurate integration scheme is required; speed is also a desired property since several integrations have to be performed at a time during the optimization.
For this reason, an explicit $7^{\text{th}}/8^{\text{th}}$-order Runge-Kutta integration scheme is implemented. As all the RK methods, the idea is to approximate the $(n+1)$ step of the integration of a generic ODEs system $\dot{\mathbf{x}} = \mathbf{f}(\mathbf{x}, t)$ as

$$\mathbf{x}_{n+1} = \mathbf{x}_n + h \sum_{i=1}^{l} b_i \mathbf{k}_i \tag{5.54}$$

with

$$\mathbf{k}_i = \mathbf{f}\left(t_n + c_i h,\ \mathbf{x}_n + h \sum_{j=1}^{i-1} a_{ij} k_j \right)$$

where h is the step size and l is the number of the stages. It can be seen that no derivative is computed, but the differential equations are simply integrated evaluating $\mathbf{f}(\mathbf{x}, t)$ at suitably derived points.
The *Runge-Kutta matrix elements* a_{ij}, the *weights* b_i and the *nodes* c_i are numerical coefficients, that change according to the order of approximation. They can be computed requiring that a method of order p has to have a truncation error of order $\mathcal{O}(h^{p+1})$. This request does not permit to define properly all the numbers, since some degrees-of-freedom exist and they can be exploited in order to customize the RK method. All these coefficients are gathered in the so-called *Butcher tableau* that gives a visual summary of the scheme.
Since Runge-Kutta methods are variable step algorithms, the choice of h and its variation during the numerical integration is of paramount importance. In fact, an high value of the step size gives a cheap, but inaccurate solution; on the other hand, accurate, but time consuming, results are obtained with a small h. Thus, the right value is sought trying to keep the truncation error below a given tolerance. The error can be defined, in a simplified way, as

$$\epsilon = \frac{\left\| \mathbf{x}_{n+1}^{RK_p} - \mathbf{x}_{n+1}^{RK_{p-1}} \right\|}{\left\| \mathbf{x}_{n+1}^{RK_p} \right\|} \tag{5.55}$$

where the subscripts of RK indicate the order of the Runge-Kutta scheme. If $\epsilon < toll$, the integration algorithm is performing well and so no adjustments have to be done, or h

can be increased; otherwise, the step size is decreased.
So, in order to compute the error, the solution using a scheme of lower order is required. For the 8^{th}-order Runge-Kutta algorithm used in this work a 7^{th}-order solution is also needed, but computing two different solutions is computationally intense, because of the high number of function evaluations. For this reason, Dorman and Prince formulas are used. They allow, exploiting the degrees of freedom of the coefficients, to compute the function in the same points both for RK7 and RK8, reducing the evaluations from 20 to 13. A summary for this scheme can be found in [31].
Figure 5.4 shows the comparison between the 8^{th}-order Runge-Kutta integration algorithm and some MATLAB® built-in functions: both *ode45* (based on Dormand-Prince 5^{th}-order Runge Kutta scheme) and *ode113* (using a variable-step, variable-order Adams-Bashforth-Moulton solver of orders 1 to 12) give inaccurate results if default tolerances are used; an accurate solution, very similar to the one of RK8, is found only if tolerances are reduced down to 10^{-12}. Moreover, Table 5.2 summarizes some data on the numerical integration, showing that RK8 provides a good result with short CPU time and few evaluation points.

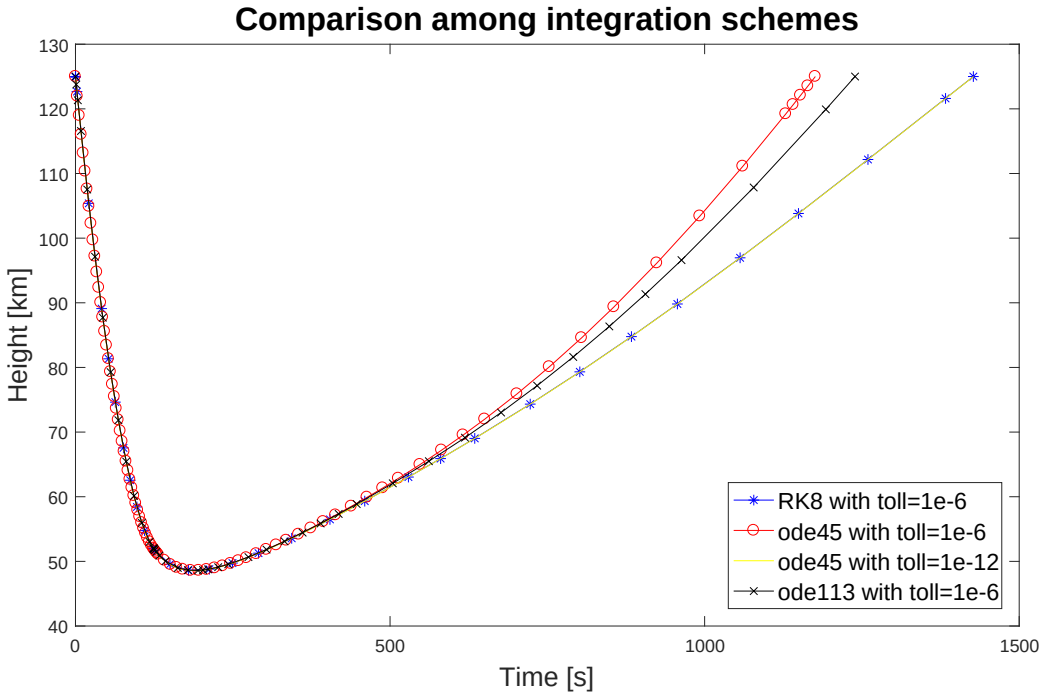

FIGURE 5.4. Comparison among different integration schemes solution for a low-Mars orbit aerocapture.

Algorithm	Tolerance	CPU time [sec]	Points number	Accuracy
RK8	10^{-6}	0.26	34	High
ode45	10^{-6}	0.051	85	Very low
ode45	10^{-12}	0.894	1513	High
ode113	10^{-6}	0.06	46	Low

TABLE 5.2. Summary of data related to different integration schemes solution for a low-Mars orbit aerocapture.

5.4.2.1 Event handling in RK8

In this study, both the atmospheric phase and the ballistic phase do not end at a specific time instant but when a condition is verified, that is when an event occurs. So the numerical integration method has to handle this issue, being able to compute the exact instant when the stopping situation occurs. Due to that, a root-finding algorithm has to be implemented.

As many other built-in ODE solvers, *regula falsi* is used. It is similar to the bisection method, but the new solution guess is estimated using the secant method. An advantage of this method is that it does not require providing the derivatives of the event function, at the contrary, for example, of Newton's method. Assuming that the equation $f(x) = 0$ has to be solved, the method starts, as bisection, with two points a_0 and b_0, such that $f(a_0)f(b_0) < 0$. By the intermediate point theorem, the function f has a root in the interval $[a_0, b_0]$. At the step k, the root of the secant through $(a_k, f(a_k))$ and $(b_k, f(b_k))$ is evaluated. Starting from the secant equation, that is

$$\frac{y - f(a_k)}{f(b_k) - f(a_k)} = \frac{x - a_k}{b_k - a_k} \tag{5.56}$$

setting $y = 0$ and calling c_k the root value, it is possible to write

$$c_k = b_k - f(b_k)\frac{b_k - a_k}{f(b_k) - f(a_k)} \tag{5.57}$$

Now, if $f(c_k)f(a_k) < 0$, $b_{k+1} = c_k$ and $a_{k+1} = a_k$, otherwise $a_{k+1} = c_k$ and $b_{k+1} = b_k$. A graphical representation of the method is given in Figure 5.5. This process is iterated until $f(c_k) < tol$, that means that c_k is a good approximation of the function root.

For the problems in this work, this algorithm can be easily adapted and used to compute the instant when an event occurs. Defining the event function as

$$f_{ev}(\mathbf{x}, t) = 0 \tag{5.58}$$

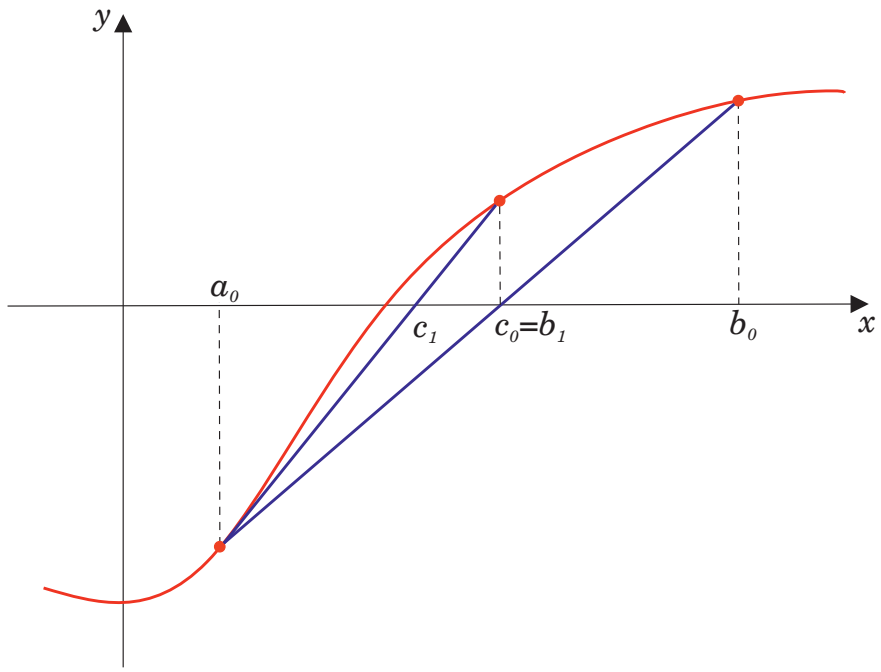

FIGURE 5.5. Graphical representation of the first steps of the regula falsi method. The red curve is the function f and the blue lines are the secants.

if during the integration the condition

$$f_{ev}(\mathbf{x}_n, t_n) f_{ev}(\mathbf{x}_{n+1}, t_{n+1}) < 0 \tag{5.59}$$

is verified, it is possible to state that in the time interval $[t_n,\ t_{n+1}]$ the event has occurred. So, an iterative process begins, with at the k-th step

$$\tilde{t}_k = t^k_{n+1} - f_{ev}\left(\mathbf{x}^k_{n+1}, t^k_{n+1}\right) \frac{t^k_{n+1} - t^k_n}{f_{ev}\left(\mathbf{x}^k_{n+1}, t^k_{n+1}\right) - f_{ev}\left(\mathbf{x}^k_n, t^k_n\right)} \tag{5.60}$$

So a new time step $\tilde{h}_k = \tilde{t}_k - t^k_n$ is defined and it is inserted in the Eq. (5.54) for the RK8, allowing to compute $\tilde{\mathbf{x}}_k$. Those values can be used to evaluate the event function in a new position. Then if $f_{ev}\left(\tilde{\mathbf{x}}_k, \tilde{t}_k\right) < toll$ the time when the event happens is found; otherwise, if $f_{ev}\left(\tilde{\mathbf{x}}_k, \tilde{t}_k\right) f_{ev}\left(\mathbf{x}^k_n, t^k_n\right) < 0$, $\mathbf{x}^{k+1}_{n+1} = \tilde{\mathbf{x}}_k$ and $t^{k+1}_{n+1} = \tilde{t}_k$ with the value for the point n left unchanged; else the other way round happens.
No check is needed for the integration error since the time step at the beginning of the regula falsi algorithm gives already a good solution and, given that h is only reduced, the error can only drop.

5.4.3 Heat flux integration

The last ODE in Eq. (5.48), describing the heat flux, is an implicit equation and, so, its integration can be an issue, since at each step its root has to be found. Fortunately though it does not depend directly on the control variable and the other three equations describing the dynamics are fully decoupled from that one; so they can be solved separately and the heating rate equation can be integrated a posteriori.
Starting from this observation, the RK8 algorithm is used only to solve the ODEs related to r, V and γ; then for each computed couple $(\tilde{r}, \tilde{V})$ describing the trajectory, the equation

$$\dot{q} - k_0 \left(\frac{\rho}{r_n}\right)^{\frac{1}{2}} \tilde{V}^{3.04} \left(1 - \frac{c_{p_{TPS}} \left(\frac{\dot{q}}{\sigma\varepsilon}\right)^{\frac{1}{4}}}{H}\right) + C r_n^a \rho^b f(\tilde{V}) = 0 \tag{5.61}$$

is solved, allowing to compute $\dot{\tilde{q}}$ for each integration time. Then a spline interpolation, with a step equal to 1 second, is performed in order to smooth down the evolution of the heat flux. As last point, the piecewise polynomial $\dot{\hat{q}}$ obtained is integrated in time using a trapezoidal numerical integration.
Table 5.3 summarizes some relevant differences between this procedure and the integration of all the 4 ODEs in Eq. (5.48) using RK8: this last method is almost 20 times slower, but there is no practical distinction in the two values found. In fact, the relative error between them can be computed as

$$err = \frac{\left|q_{RK8}(t_{out}) - q_{trapz}(t_{out})\right|}{q_{RK8}(t_{out})} = 4.2289 \times 10^{-5} \tag{5.62}$$

that is a negligible quantity.

Algorithm	CPU time [sec]	Points number	$q(t_{out})$ [W cm^{-2}]
RK8	8.638	42	1.7526×10^4
trapz	0.496	34	1.7526×10^4

TABLE 5.3. Summary of relevant differences between RK8 and trapezoidal rule for heat flux integration for a aerocapture to a low-Mars orbit.

5.4.4 Summary

In conclusion of this section, a wrap-up is needed in order to clearly represent how the NLP is solved. The block scheme in Figure 5.6 schematizes the logic flow followed in solving this problem. On the other hand, Figure 5.7 shows the algorithm used to find a solution for the aero-ballistic capture optimization.

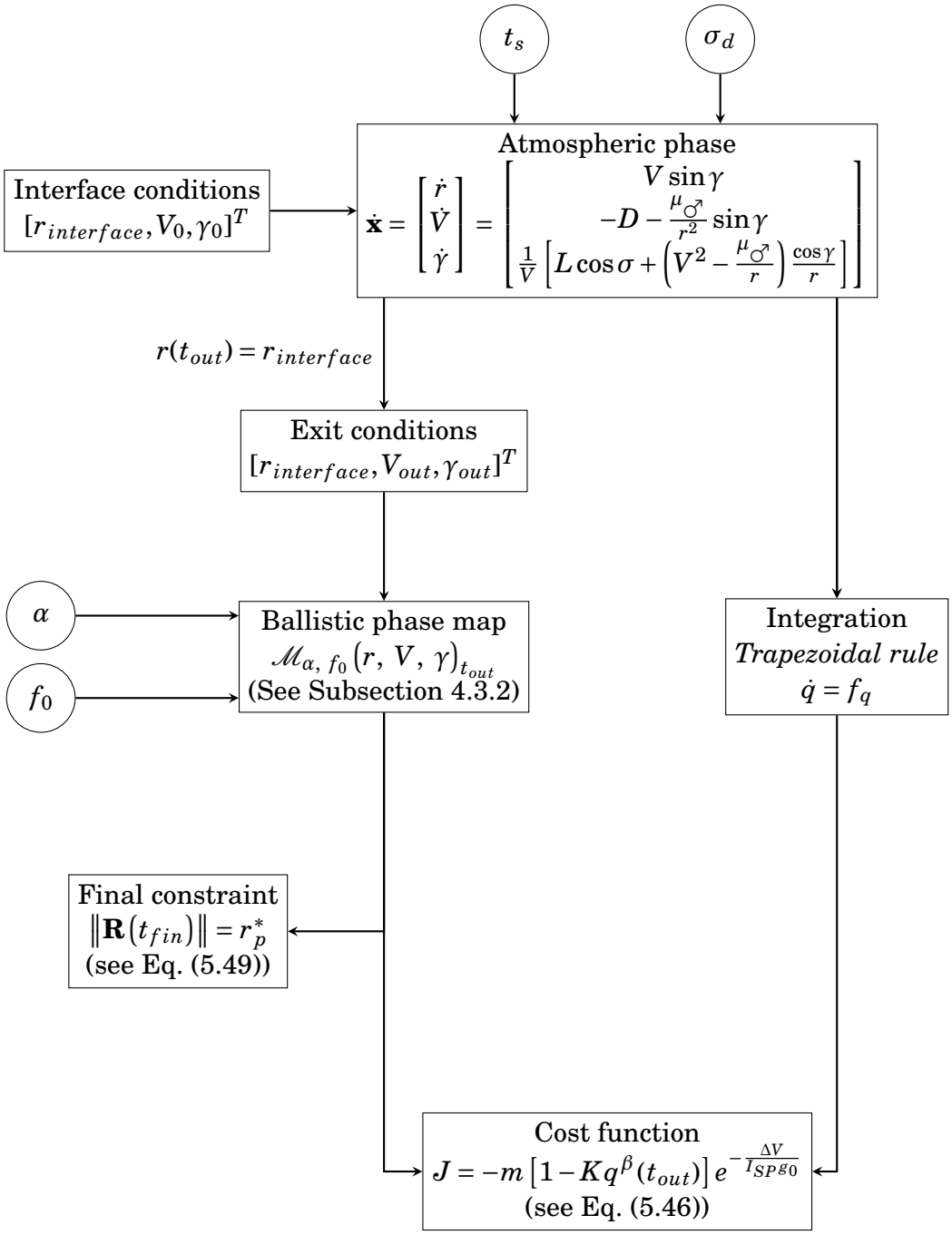

FIGURE 5.6. Block scheme of the logic flow for solving the nonlinear programming problem.

1. **Initialization**
   Set vehicle parameters
   Set final orbit parameters r_p^* and r_a^*
   Select initial conditions V_0 and γ_0 at the interface
   Set the number n of local optimization

2. **Optimization**
   Generate n initial points of optimization parameters for local optimizer (inside the intervals $t_s \in [0,\ 200]$, $\sigma_d \in [0,\ \pi]$, $\alpha \in [0,\ 2\pi]$ and $f_0 \in [0,\ 2\pi]$)
   Assign j =number of current local minimization
   FOR $j = 1 : n$
   Start a local optimization using *interior point method* with as starting point $[t_s(j),\ \sigma_d(j),\ \alpha(j),\ f_0(j)]$
   i. *Atmospheric phase*
   Integrate using RK8 the first three equations of the system (5.48) with $\sigma = 5°$, until when $t = t_s$
   Integrate using RK8 the first three equations of the system (5.48) with $\sigma = \sigma_d$, until when $r = r_{interface}$
   Use the solution in order to compute $\dot{\tilde{q}}$ through Eq. (5.61)
   Perform a spline interpolation on $\dot{\tilde{q}}$
   Integrate $\dot{\tilde{q}}$ using trapezoidal rule to get $q(t_{out})$
   ii. *Ballistic phase*
   Use map $\mathscr{M}_{\alpha,\ f_0}\left(r,\ V,\ \gamma\right)_{t_{out}}$, described in Subsection 4.3.2
   a) Convert the state from P2-centered inertial coordinates to polar non-inertial coordinates, using Eqs. (4.8) and (4.9)
   b) Integrate until pericenter conditions are reached (Eq. (4.6))
   c) Convert back to the P2-centered inertial frame
   iii. *Final computations*
   Compute final constraint $\left\|\mathbf{R}\left(t_{fin}\right)\right\| - r_p^*$
   Compute ΔV (Eq. (5.47))
   Compute the cost function J, as in Eq. (5.46)
   END
   Pick the best feasible solution

FIGURE 5.7. Algorithm to solve nonlinear programming problem for aero-ballistic capture optimization.

CHAPTER 6

RESULTS

In this chapter results will be presented. In the first sections, some reference orbits are taken into consideration and a comparison among different strategies is made. Then, a general comparison is performed in order to assess when an approach is better than another one.

6.1 Study cases

First of all, a presentation of the selected reference orbits is mandatory. Sample final orbits around Mars with direct scientific interest have been chosen. Orbit inclination is not considered since no lateral dynamics is addressed in this thesis and, so, all the orbits lies on Martian orbital plane.

1. A *low-Mars orbit* (LMO) is the first study case. LMOs are important for planetary science: they allow a closer observation of the *Red Planet*, the possibility of analyzing the subsurface and the Martian atmosphere. Among LMOs, the one selected is a circular orbit with a radius equal to 3690 km, similar in altitude with respect to previous missions, like *Mars Reconnaissance Orbiter* [23];

2. Then a final orbit with the same radius of an *areostationary orbit* is also investigated. Areostationary orbits are circular equatorial orbits with a period equal to the rotational period of Mars. This means that a spacecraft on these orbits will appear fixed in the sky for a Martian observer. These orbits are analogous to

geostationary orbits. They have a radius of 20427 km. Future human exploration missions forecast an areostationary satellite for communication purposes [14];

3. As last reference scenario, trajectories for the *Martian moons* are considered. Mars has two natural satellites, Phobos and Deimos, the first closer to the surface (the orbital radius is 9375 km) and the other farther from the surface, beyond the areostationary orbit, revolving at a distance of 23458 km. Both moons have a quasi-equatorial orbit and their gravitational interaction can be neglected since they are very small.

Table 6.1 summarizes the characteristics of the different scenarios.

	r [km]	h [km]	T [h]
LMO	3690	300	1.89
Areostationary	20427	17037	24.62
Phobos	9375	5985	7.66
Deimos	23458	20068	30.3

TABLE 6.1. Study cases main data.

6.2 Aero-ballistic capture solutions

Solutions related to aero-ballistic capture are shown first. Both the atmospheric phase and the ballistic phase are presented and analyzed.

6.2.1 Low-Mars orbit

Table 6.2 summarizes the optimization parameters for the aero-ballistic capture to the LMO. The bank-angle reversal occurs quite soon, after only 13 seconds. On the other hand, the final bank angle has a relative small value with respect to aerocapture solution used in literature (see [19] where $\sigma_d = 110°$). A lower maximum bank angle means a faster change in attitude and so a more easy situation to handle for the guidance algorithm. The overall atmospheric passage lasts 338 s.

t_s [s]	σ_d [°]	α [°]	f_0 [°]
13.4	64.40	199.24	51.56

TABLE 6.2. Optimization parameters for the aero-ballistic capture to LMO.

Starting from the atmospheric phase, Figures 6.1(a) and 6.1(b) show the behavior of the spacecraft during the atmospheric flight. The altitude has a "parabolic" shape, decreasing smoothly until a minimum at 49.7 km.

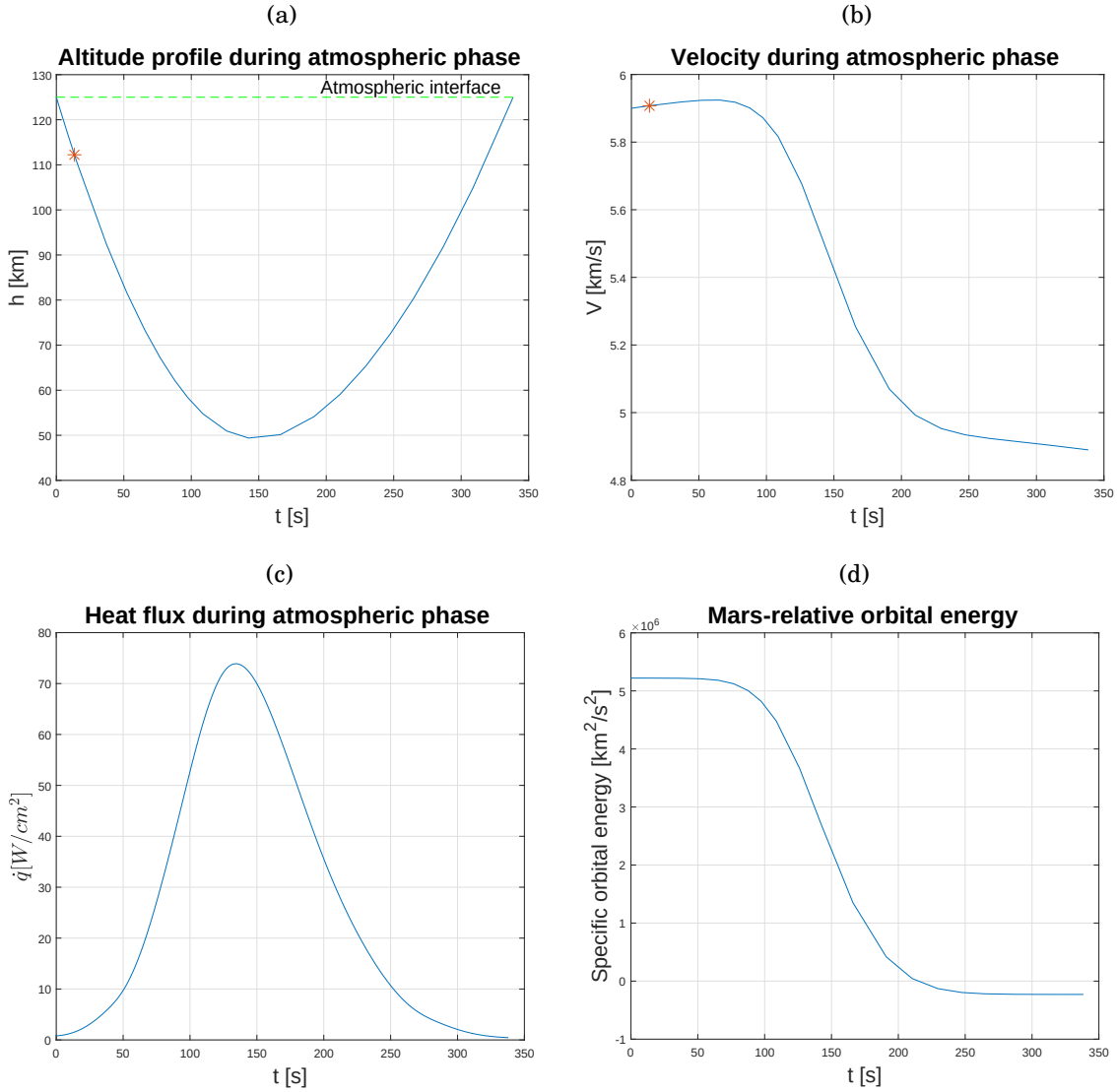

FIGURE 6.1. (a) Altitude profile for the atmospheric phase of an aero-ballistic capture to a low-Mars orbit. (b) Velocity for the atmospheric phase of an aero-ballistic capture to a low-Mars orbit. Asterisk indicates the switching time point. (c) Heat flux for the atmospheric phase of an aero-ballistic capture to a low-Mars orbit. (d) Orbital energy with respect to Mars during the atmospheric phase.

For what concerns the speed (Figure 6.1(b)), it is possible to notice that in the first seconds the spacecraft accelerates. This is related to the fact that at the beginning of

this phase the vehicle is approaching the pericenter of its orbit, so the velocity tends to increase, while at the same time the density of the atmosphere is still too low, and it is not able to counteract this phenomenon. Then, passing through denser layers of the atmosphere, the spacecraft slows down and it exits the atmosphere with a velocity of 4.89 km/s.

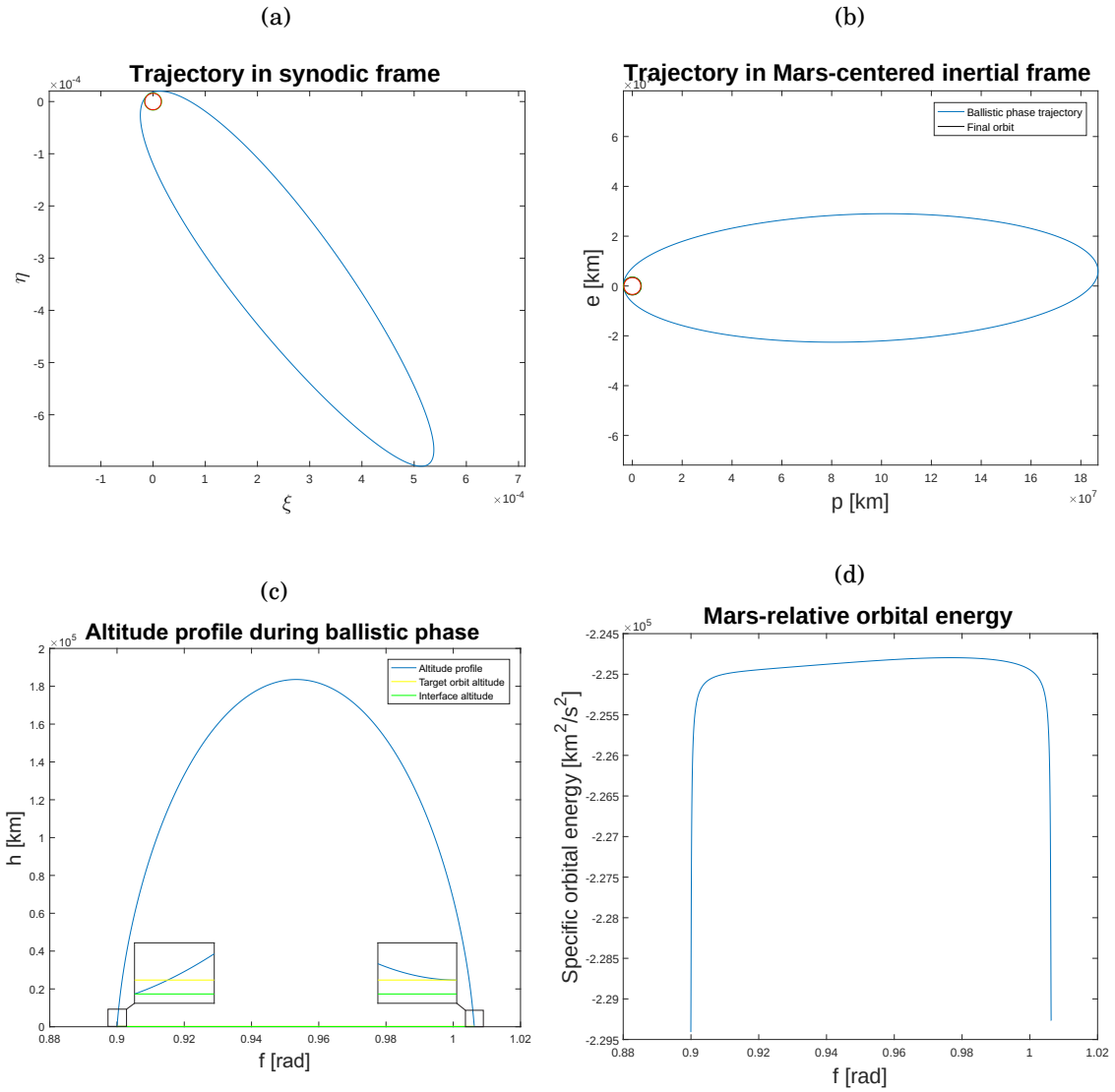

FIGURE 6.2. (a) Trajectory in synodic frame for the ballistic phase of an aero-ballistic capture to a low-Mars orbit. Sun is at far left. (b) Trajectory in Mars-centered inertial frame for the ballistic phase of an aero-ballistic capture to a low-Mars orbit. (c) Altitude profile for the ballistic phase of an aero-ballistic capture to a low-Mars orbit. (d) Orbital energy with respect to Mars during the ballistic phase.

Figure 6.1(c) shows the history of the heat flux. It has a peak just before the spacecraft reaches the minimum altitude, very lower with respect to the $\dot{q}_{max}$ boundary ($\dot{q}_{max}$ = 460 $\mathrm{W\,cm^{-2}}$). The cumulative heat load, obtained integrating the heat flux, is equal to 9097 $\mathrm{J\,cm^{-2}}$.
As last point, it is possible to see in Figure 6.1(d) that, as expected, the orbital energy relative to Mars goes from positive to a negative value, representing the closure of the orbit around the planet.
The trajectory followed by spacecraft during ballistic phase is shown in Figures 6.2(a) and 6.2(b). The first image shows that the apocenter of the transfer orbit is in the IV quadrant. This result agrees with the theory since a rise in pericenter is sought.
The altitude profile in Figure 6.2(c) shows that in order to bring the pericenter on the desired value the vehicle goes very far from the planet surface, at a distance equal to 54 Mars radii, but it is still inside the sphere of influence that has a radius of 174 Mars radii.
Also the analysis of the orbital energy shows some interesting features (see Figure 6.2(d)): first of all, the farther is the spacecraft, the higher is the orbital energy. Then, above all, at the end of the maneuver, the spacecraft has a higher value of orbital energy with respect to the initial time instant. This means that, remembering that the final point is the new pericenter by construction, an higher value for the pericenter distance is attained, as expected.
Table 6.3 summarizes all the relevant values for this solution. t_{BAL} indicates the time of the ballistic phase, from the atmospheric exit up to the final orbit.

t_{out} [s]	t_{BAL} [d]	t_{fin} [d]
338.42	10.33	10.33

$q(t_{out})$ [J/cm^2]	ΔV [km/s]	m_{fin} [kg]
9097	1.384	**1274**

TABLE 6.3. Times and relevant values for mass computation for the aero-ballistic capture to a low-Mars orbit.

6.2.2 Areostationary

Optimized parameters for the present application case are shown in Table 6.4. It is possible to see that the parameters related to the atmospheric phase (t_s and σ_d) are similar to the one for LMO, even if the final orbit target is different. Given this similarity,

it can be stated that the atmospheric flight does not play a big role, but the final state is attained only due to a dissimilar ballistic trajectory. In fact, relevant differences can be found in α and f_0, with this last value very close to 0, which allows exploiting as much as possible the Solar gravitational assist, according to theory.

t_s [s]	σ_d [°]	α [°]	f_0 [°]
14.26	61	347.11	0.46

TABLE 6.4. Optimization parameters for the aero-ballistic capture to a areostationary orbit.

Figures from 6.3(a) to 6.3(d) illustrate the atmospheric path of the spacecraft in this solution. As expected from the optimization parameters, there are no visible differences with respect to the low-Mars orbit solution, except for the energy, that at the atmospheric exit time is closer to 0, representing an orbit with an higher apocenter. This difference is due to a slightly higher exit velocity, equal to 4.92 km/s.
At the opposite, the ballistic phase is very different from the one for LMO. Figure 6.4(a) shows the trajectory in synodic frame: it is a figure of eight and it has the apocenter in the II quadrant. The orbit in inertial Mars-centered frame is depicted in Figure 6.4(b).
The altitude profile in Figure 6.4(c) shows that the maximum distance reached by the spacecraft is 174 Martian radii, 3 times the apocenter for the LMO case. This distance is at the boundary of the Mars *sphere of influence*.
In the Figure 6.4(d), the Mars-relative energy is plotted. Its final value is higher than both the initial time value and the low-Mars orbit case, since the pericenter is further from Mars.
Table 6.5 summarizes some relevant data for this case study.
The overall *time of flight*, slightly less than 2 months, is for sure higher with respect to a simply aerocapture maneuver and, depending on the mission, this can be a disadvantage, that has to be taken in account.
As last observation, it can be pointed out that the final mass has an higher value than the LMO final mass. This is an expected result, because the further is the final orbit, the lower is the heat load during atmospheric phase and the ΔV needed for the orbital maneuver. Thus, a higher final orbit radius means also an higher final mass and so better performances.

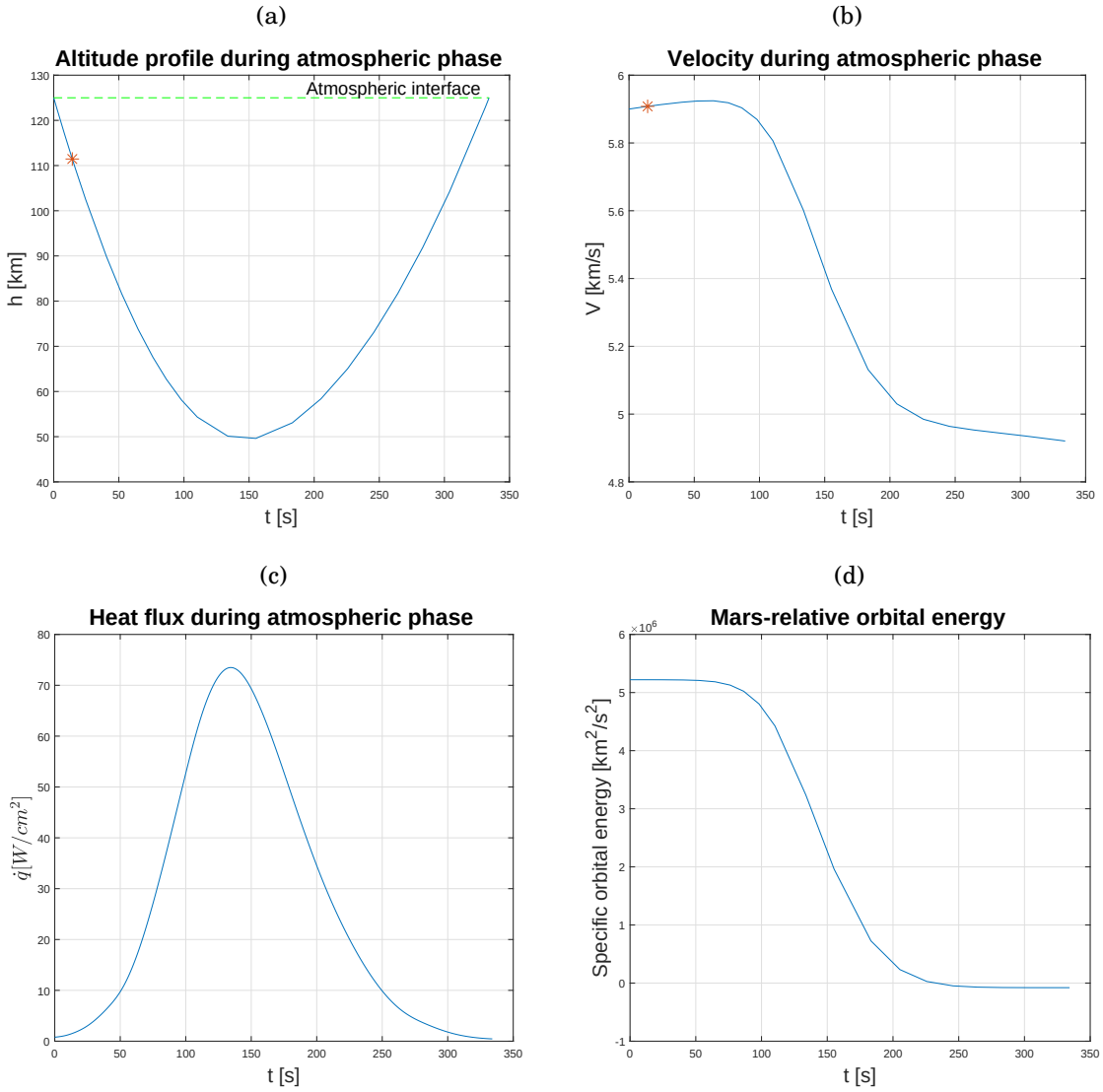

FIGURE 6.3. (a) Altitude profile for the atmospheric phase of an aero-ballistic capture to an areostationary orbit. (b) Velocity for the atmospheric phase of an aero-ballistic capture to an areostationary orbit. Asterisk indicates the switching time point. (c) Heat flux for the atmospheric phase of an aero-ballistic capture to an areostationary orbit. (d) Orbital energy with respect to Mars during the atmospheric phase.

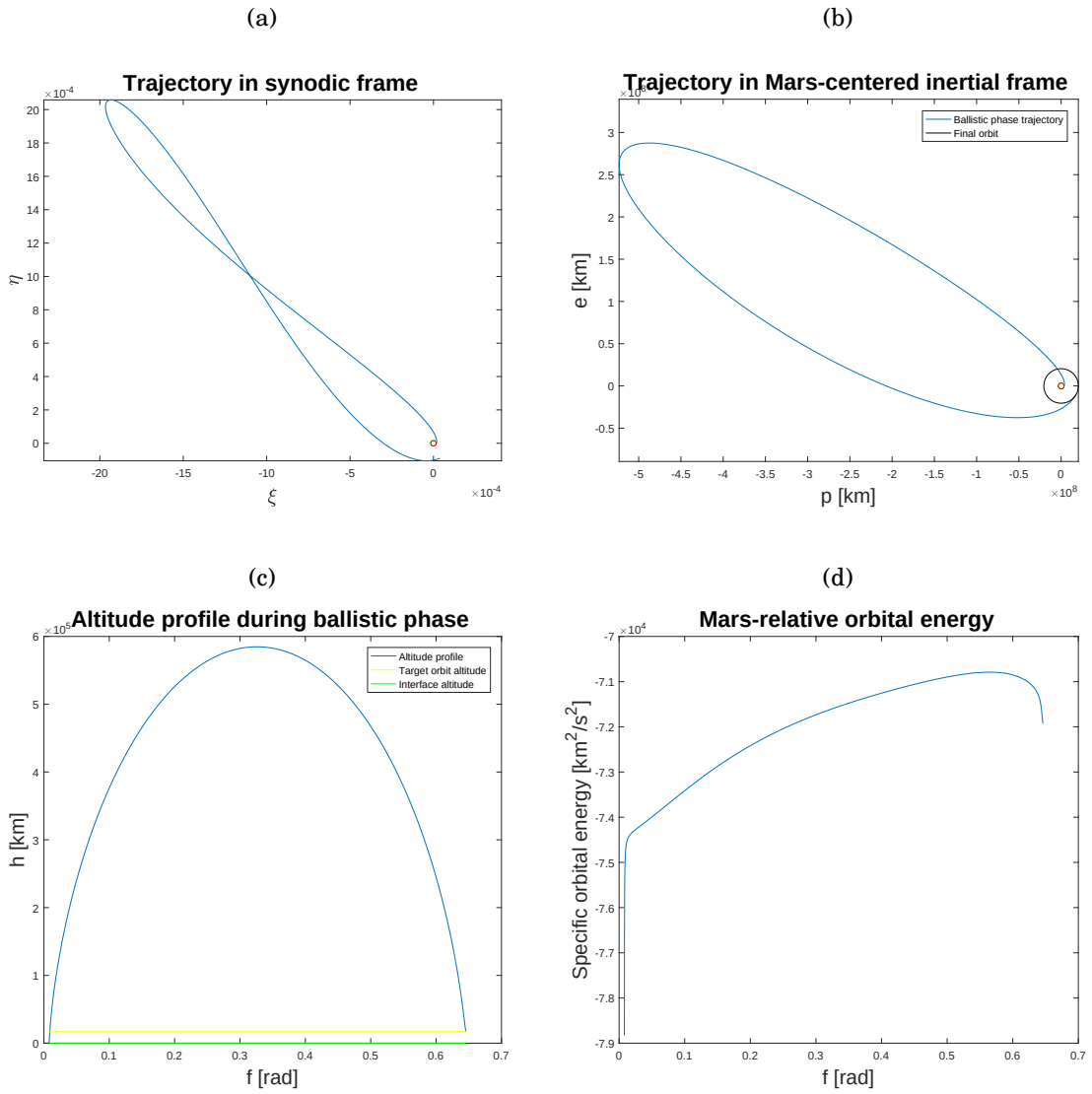

FIGURE 6.4. (a) Trajectory in synodic frame for the ballistic phase of an aero-ballistic capture to an areostationary orbit. Sun is at far left. (b) Trajectory in Mars-centered inertial frame for the ballistic phase of an aero-ballistic capture to an areostationary orbit. (c) Altitude profile for the ballistic phase of an aero-ballistic capture to an areostationary orbit. (d) Orbital energy with respect to Mars during the ballistic phase.

t_{out} [s]	t_{BAL} [d]	t_{fin} [d]
334.31	58.29	58.29

$q(t_{out})$ [J/cm^2]	ΔV [km/s]	m_{fin} [kg]
8955	0.564	**1655**

TABLE 6.5. Times and relevant values for mass computation for the aero-ballistic capture to an areostationary orbit.

6.2.3 Moons

In Table 6.6, the optimization parameters related to trajectories to the moons can be found. The two final bank angles are quite close one with the other, but the switching times are quite different, bringing to different solutions. Also in these cases, f_0 is the lower, when the final orbit radius is the higher.

	t_s [s]	σ_d [°]	α [°]	f_0 [°]
Phobos	6.68	61.41	346.58	1.51
Deimos	23.47	60.99	359.37	0.06

TABLE 6.6. Optimization parameters for the aero-ballistic capture to moons' orbits.

Figures 6.5(a) and 6.5(b) show the altitude profile for the solution to Phobos and Deimos respectively. Except for the switching time marker, there are no visible differences between these two solutions; and it seems there are not clear variation with respect to solutions for LMO and areostationary orbit. Also in these cases, targeting the final orbit is mostly driven by the ballistic flight.

Figures 6.6(a) and 6.6(b) show the transfer orbit to Phobos and Deimos in non-inertial reference frame. Also in this case, the orbits follow a figure of eight, similar to the one for areostationary orbit, narrower in the first case. Both have apocenter in the II quadrant, in agreement with the Solar gravitational assist theory.
In Figures 6.6(c) and 6.6(d), the inertial orbits are plotted. In both cases the spacecraft has to go very far from Mars in order to attain the desired raise in pericenter: it is important then to notice that, if Deimos is the desired target, the apocenter of the transfer orbit is at a distance equal to 181 Martian radii, that means beyond the sphere of influence of the planet.

In Tables 6.7 and 6.8, relevant data for the aero-ballistic trajectories to Phobos and Deimos are gathered. As expected, the time of the atmospheric phase is similar for both

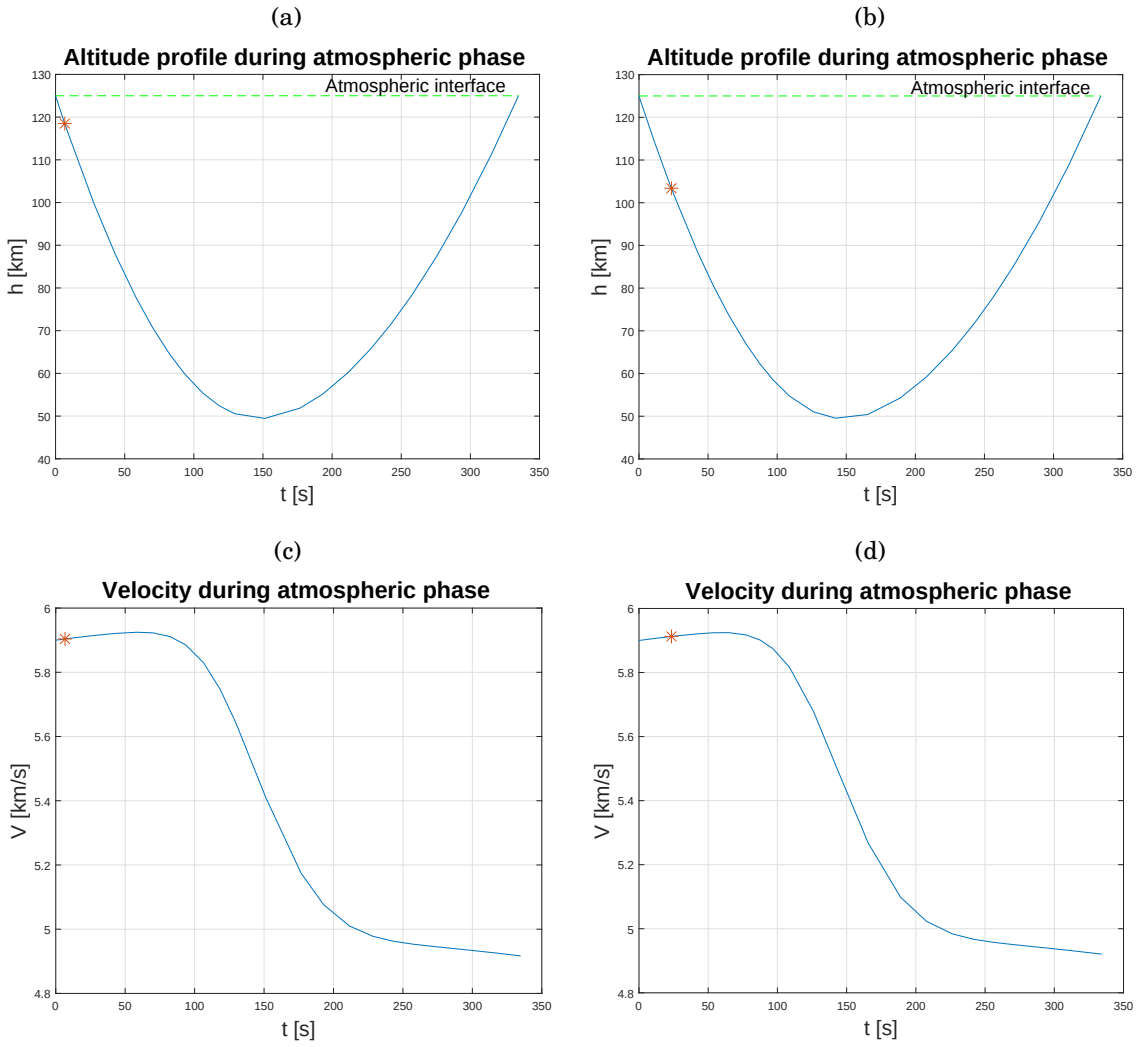

FIGURE 6.5. (a)-(b) Altitude profile for the atmospheric phase of an aero-ballistic capture to Phobos and Deimos. (c)-(d) Velocity for the atmospheric phase of an aero-ballistic capture to Phobos and Deimos. Asterisk indicates the switching time point.

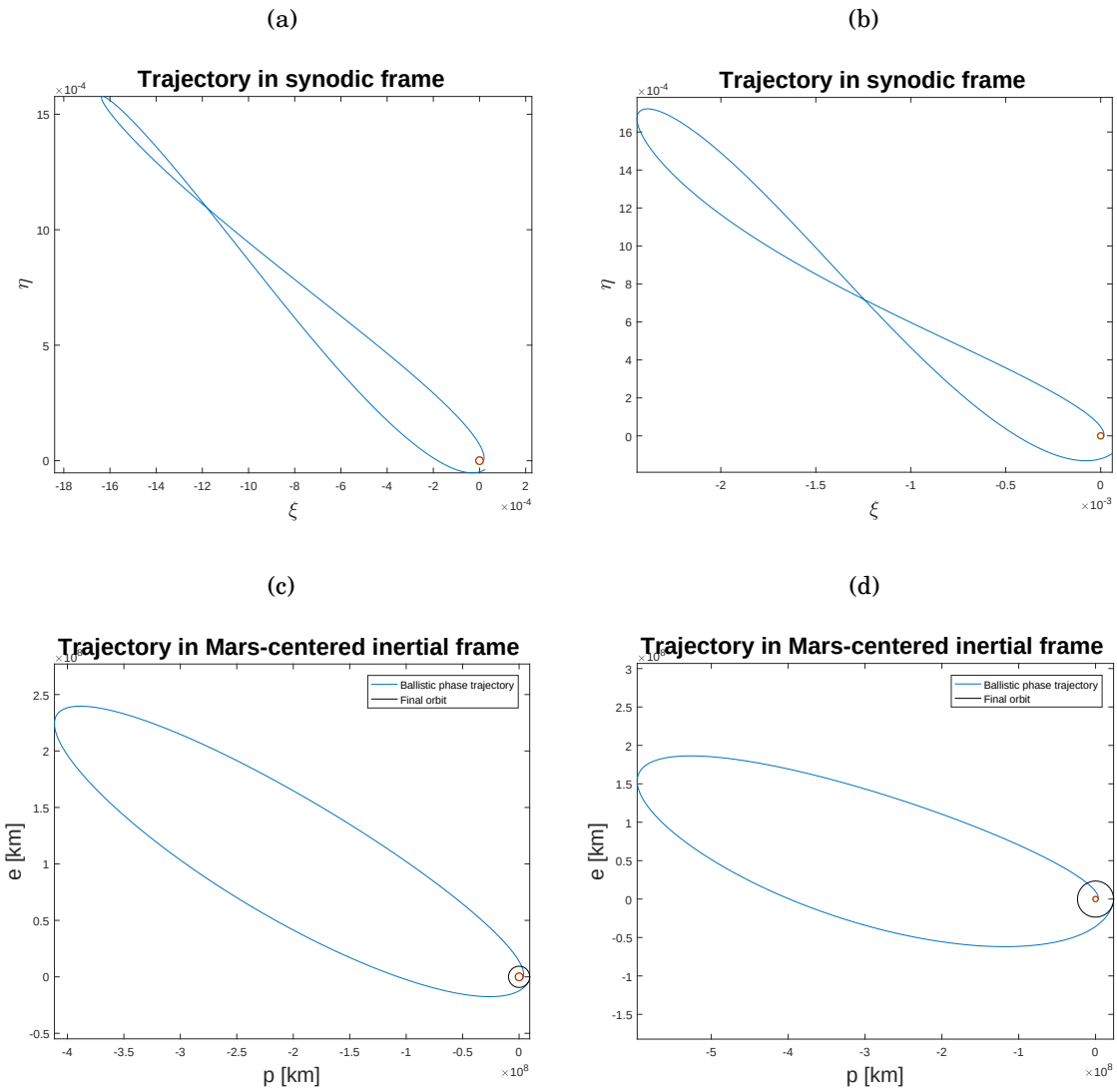

FIGURE 6.6. (a)-(b) Trajectory in synodic frame for the ballistic phase of an aero-ballistic capture to Phobos and Deimos. Sun is at far left. (c)-(d) Trajectory in Mars-centered inertial frame for the ballistic phase of an aero-ballistic capture to Phobos and Deimos.

problems and they are comparable with times of the previous cases. On the other hand, the ballistic phase time is lower for Phobos than the one for Deimos. This result agrees with expectations.
For what concerns the total head load, no major differences can be found between these two solutions and the previous NLP problem results, since the flight through the atmosphere is similar for all the four study cases. The interesting difference is only in propellant consumption that, decreases, increasing the final orbit radius.

t_{out} [s]	t_{BAL} [d]	t_{fin} [d]
334.78	41.21	41.21

$q(t_{out})$ [J/cm^2]	ΔV [km/s]	m_{fin} [kg]
8973	0.855	**1509**

TABLE 6.7. Times and relevant values for mass computation for the aero-ballistic capture to Phobos.

t_{out} [s]	t_{BAL} [d]	t_{fin} [d]
334.28	63.94	63.95

$q(t_{out})$ [J/cm^2]	ΔV [km/s]	m_{fin} [kg]
8955	0.523	**1677**

TABLE 6.8. Times and relevant values for mass computation for the aero-ballistic capture to Deimos.

6.3 Reference aerocapture solutions

In order to understand if the aero-ballistic capture has some advantages on already known techniques, purely aerocapture solutions are derived for the study cases as well.These are taken as reference for comparison.

6.3.1 Methodology

First of all, an overview on how the aerocapture problem is solved in needed. As proven in Section 5.1, also the aerocapture optimization can be transcribed in a nonlinear

programming problem, similar to the one for aero-ballistic capture.
In the case, the aim is to find only t_s and σ_d that minimize the cost function

$$J = \varphi(\mathbf{x}(t_{out})) = -m_0 \left[1 - Kq^{\beta}(t_{out})\right] e^{-\frac{\Delta V}{I_{sp} g_0}} \tag{6.1}$$

with

$$\Delta V = \sqrt{2\mu_{\sun}} \left(\sqrt{\frac{1}{r_a^*} - \frac{1}{r_a^* + r_p^*}} - \sqrt{\frac{1}{r_{a*}} - \frac{1}{2a}} \right) \tag{6.2}$$

where

$$a = \frac{\mu_{\sun}}{2\mu_{\sun}/r(t_{out}) - V^2(t_{out})} \tag{6.3}$$

such that

$$\dot{\mathbf{x}} = \begin{bmatrix} \dot{r} \\ \dot{V} \\ \dot{\gamma} \\ \dot{q} \end{bmatrix} = \begin{bmatrix} V \sin\gamma \\ -D - \frac{\mu_{\sun}}{r^2} \sin\gamma \\ \frac{1}{V}\left[L\cos\sigma + \left(V^2 - \frac{\mu_{\sun}}{r}\right)\frac{\cos\gamma}{r}\right] \\ f_q(r,V) \end{bmatrix} \tag{6.4}$$

where f_q is the explicit function describing the heat flux and with the bank angle

$$\sigma = \begin{cases} \sigma_0 & \text{when } t_0 < t \leq t_s \\ \sigma_d & \text{when } t_s < t < t_{out} \end{cases}$$

where t_{out} is the time when $r = r_{interface}$, subjected to the final constraint

$$r_a^* = r_a = a\left(1 + \sqrt{1 - \frac{V^2(t_{out}) r^2(t_{out}) \cos^2\gamma(t_{out})}{\mu_{\sun} a}}\right) \tag{6.5}$$

Furthermore, the inequality path constraints in Eqs. (5.52) are considered.
From the numerical point of view, the same techniques illustrated in Section 5.4 are implemented. This means that a *MultiStart* algorithm is implemented as global solver, using as local minimization method an interior point scheme. About integration, the only the first 3 ODEs from the system (6.4) are directly integrated using the 8^{th}-order Runge-Kutta scheme, while the last equation is evaluated through the trapezoidal rule.

6.3.2 Low-Mars orbit

Table 6.9 summarizes the optimization parameters for the aerocapture to a low-Mars orbit. The bank-angle reversal happens later with respect to the same problem for aero-ballistic capture. Also the value of the final bank angle is higher, closer to the maximum admissible value.

t_s [s]	σ_d [°]
123.86	179

TABLE 6.9. Optimization parameters for the aerocapture to a low-Mars orbit.

Figures 6.7(a) and 6.7(b) show the behavior of the spacecraft during the atmospheric flight. They are quite different from the ones of aero-ballistic capture.

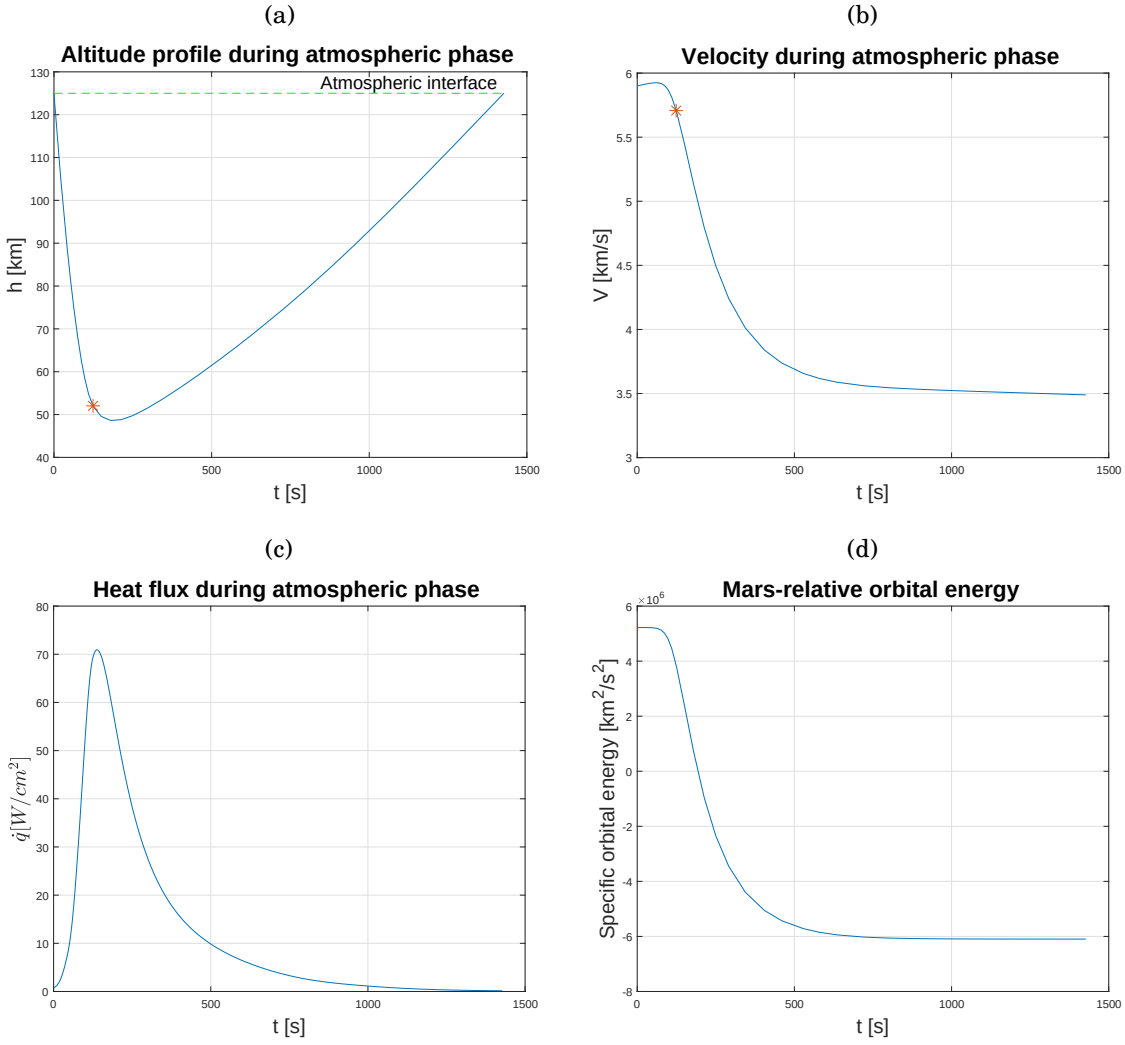

FIGURE 6.7. (a) Altitude profile for an aerocapture to a low-Mars orbit. (b) Velocity for an aerocapture to a low-Mars orbit. Asterisk indicates the switching time point. (c) Heat flux for an aerocapture to a low-Mars orbit. (d) Orbital energy with respect to Mars during the aerocapture.

Even if the minimum altitude reached is not so different, the altitude profile shows clearly a more evident knee just after the bank-angle reversal, preceded by a steep descending path and followed by a more gradual ascending trajectory.
The velocity plot has a similar shape, but the final speed is lower than aero-ballistic capture, since an orbit closer to Mars is desired.
In Figure 6.7(c) the heat flux is depicted. The heat flux peak has approximately the same figure than aero-ballistic capture, but, since the time of the atmospheric flight is higher, an higher value for the total heat load is expected.
For what concerns the orbital energy (Figure 6.7(d)), the final value is lower with respect to the one in Figure 6.1(d), where it is very close to 0. This is an expected result.

Table 6.10 summarizes some relevant data about this problem. With t_{BAL}, in this case, is indicated the time from the atmospheric exit to the apocenter of the transfer orbit.
In comparison with aero-ballistic capture, the atmospheric flight lasts about five times longer, since more energy has to be dissipated. On the other hand, the ballistic time of flight is only 26 minutes, with an overall maneuver time, from the entrance in the atmosphere to the final orbit, of only 50 minutes. This value is very small in comparison with the aero-ballistic capture ToF.
Moreover, even if the cumulative heat load is two times higher than before, the propellant consumption is "negligible", bringing to an improvement in the final mass of 27%.
So, in conclusion, for low-Mars orbit the aerocapture shows some relevant advantages with respect to aero-ballistic capture, both in time-of-flight and in final mass.

t_{out} [s]	t_{BAL} [s]	t_{fin} [s]
1427	1574	3001

$q(t_{out})$ [J/cm^2]	ΔV [km/s]	m_{fin} [kg]
17526	38.16	**1868**

TABLE 6.10. Times and relevant values for mass computation for the aerocapture to a low-Mars orbit.

6.3.3 Areostationary

Optimization parameters for the aerocapture to an areostationary orbit are shown in Table 6.11. In this solution, the spacecraft flies lift down since the beginning, but with a relative low maximum bank angle.

t_s [s]	σ_d [°]
0.006	86.89

TABLE 6.11. Optimization parameters for the aerocapture to an areostationary orbit.

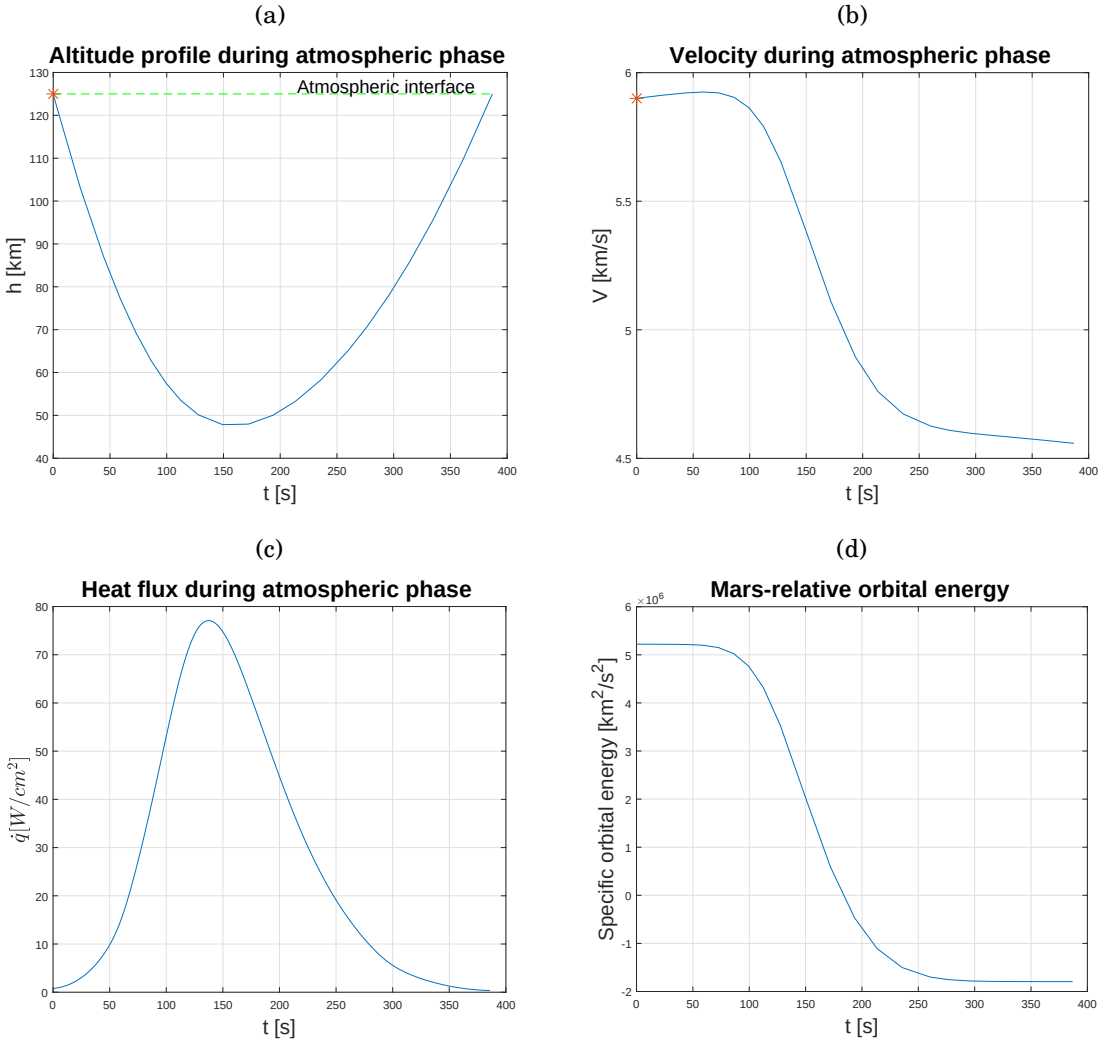

FIGURE 6.8. (a) Altitude profile for an aerocapture to an areostationary orbit. (b) Velocity for an aerocapture to an areostationary orbit. Asterisk indicates the switching time point. (c) Heat flux for an aerocapture to an areostationary orbit. (d) Orbital energy with respect to Mars during the aerocapture.

The atmospheric path of the spacecraft is described by the Figures 6.8(a) and 6.8(b). They are similar to the one of the areo-ballistic capture, but both the minimum altitude and the exit velocity are lower.

On the other hand, the heat flux peak is higher and, so, an higher total heat load is expected, taking in account also that more energy has to be dissipated.
Of course, in this case, the orbital energy assumes a lower value with respect to aero-ballistic capture, as showed in Figure 6.8(d) since an orbit closer to Mars is sought.
In Figure 6.9, the ballistic trajectory from the interface exit to the final orbit is plotted. It is very different from the areo-ballistic capture ballistic phase and it is more similar in shape to an Hohmann transfer.

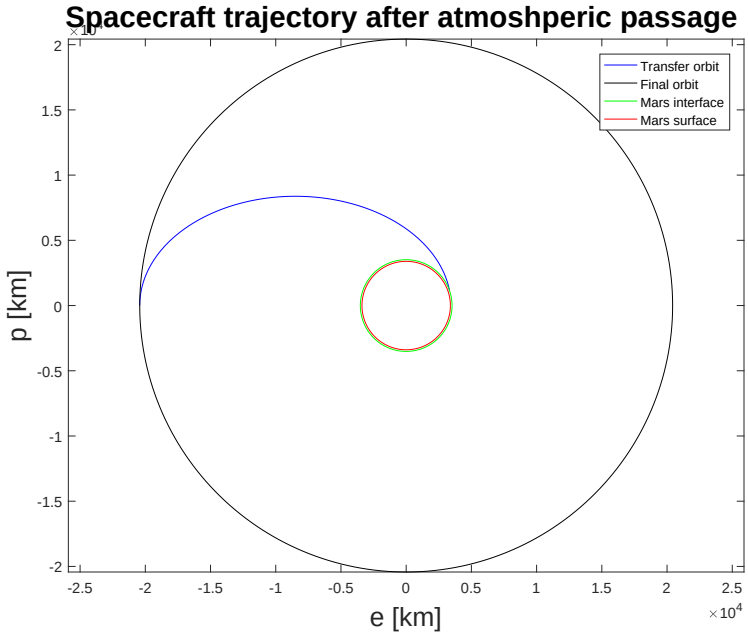

FIGURE 6.9. Transfer and final orbits for an aerocapture to an areostationary orbit.

Table 6.12 summarizes some relevant data for aerocapture to areostationary orbit.
Even if the times for the atmospheric phase have comparable values for between aerocapture and aero-ballistic capture, the time of flight for the ballistic leg is considerably reduced, since in the last case lasts only few hours.
On the other hand, both the total heat load and the ΔV needed are higher, and so the final mass is lower in aerocapture.
In conclusion, it is possible to deduce that for final orbit close to the Mars surface, the aerocapture has some advantages in terms of mass, but the further the spacecraft has to go, the more convenient become the aero-ballistic capture, even if from the time point of view aerocapture is always the best option.

t_{out} [s]	t_{BAL} [h]	t_{fin} [h]
386.97	5.43	5.53

$q(t_{out})$ [J/cm^2]	ΔV [km/s]	m_{fin} [kg]
10472	0.671	**1585**

TABLE 6.12. Times and relevant values for mass computation for the aerocapture to an areostationary orbit.

6.3.4 Moons

Optimization parameters relative to trajectories to the moons can be found in Table 6.13. For both final orbits, the switching time is very early, after only few seconds from the beginning of the simulation. Values of the final bank angle are higher with respect to aero-ballistic capture. By comparison with the solutions in the previous study cases, σ_d seems to have a decreasing behavior, while desired final orbit radius increases.

	t_s [s]	σ_d [°]
Phobos	1.71	98.06
Deimos	2.62	84.84

TABLE 6.13. Optimization parameters for the aerocapture to moons' orbits.

Figures 6.10(a) and 6.10(b) show the altitude profile for solutions to Phobos and Deimos respectively. As showed, analyzing again the solutions in the two previous study cases, two general rules can be drawn: the knee is clearer and the minimum altitude is smaller when the final orbit is farther. For what concerns comparison with aero-ballistic capture, the shape of altitude profile is not so different, but it can be seen that the atmospheric flight lasts longer and a lower altitude is reached.
Moreover, in Figures 6.10(c) and 6.10(d) the velocity profile is plotted. It can be seen that the final velocity is lower in the first case, since Phobos is closer to the Martian soil and so the apocenter of the spacecraft orbit has to have a lower altitude.

In Tables 6.14 and 6.15 relevant data about aerocapture to Phobos and Deimos are gathered. As expected, the time of the atmospheric flight is higher in the first case, since more energy has to be dissipated, while the time of flight of the transfer orbit is lower. In both cases, the aero-ballistic capture takes more time to complete the injection on the final orbit.
From the mass point of view, the statement made in the previous subsection can be confirmed: the farther the spacecraft has to go, the higher the heat load and the propellant

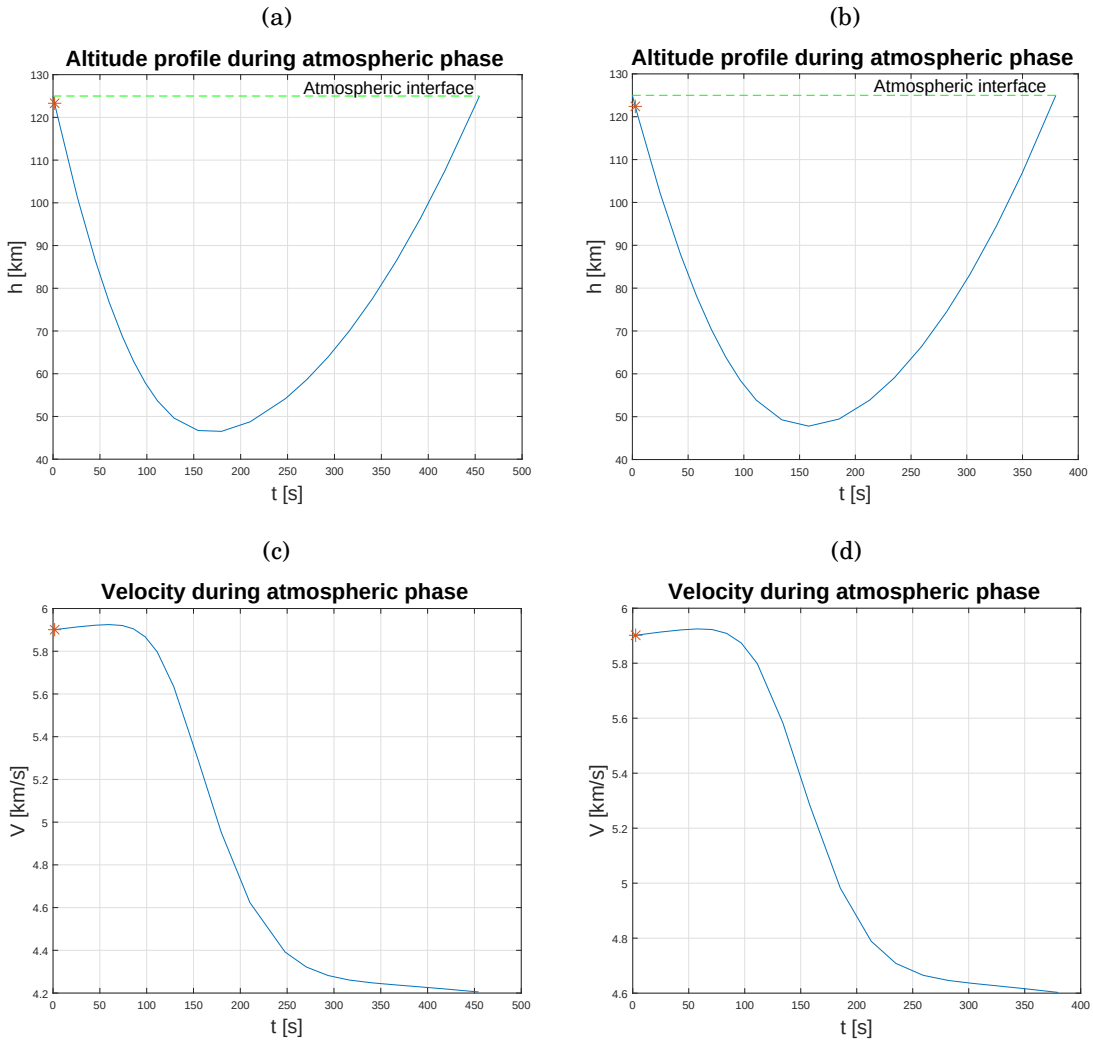

FIGURE 6.10. (a)-(b) Altitude profile for an aerocapture to Phobos and Deimos. (c)-(d) Velocity for an aerocapture to Phobos and Deimos. Asterisk indicates the switching time point.

consumption are and so the lower is the final mass in comparison with aero-ballistic capture.

t_{out} [s]	t_{BAL} [h]	t_{fin} [h]
454.49	2.08	2.20

$q(t_{out})$ [J/cm^2]	ΔV [km/s]	m_{fin} [kg]
11753	0.572	**1624**

TABLE 6.14. Times and relevant values for mass computation for the aerocapture to Phobos.

t_{out} [s]	t_{BAL} [h]	t_{fin} [h]
379.28	6.51	6.61

$q(t_{out})$ [J/cm^2]	ΔV [km/s]	m_{fin} [kg]
10299	0.668	**1588**

TABLE 6.15. Times and relevant values for mass computation for the aerocapture to Deimos.

6.4 Reference impulsive-maneuver solutions

A last analysis has to be done on trajectories using only propulsive maneuvers, in order to show their low efficiency with respect to aero-assisted methods (see [5]).
Two different strategies of this kind are implemented:

1. *Direct insertion*: this is the typical method used today for Martian missions; the spacecraft is injected in the final orbit directly from the hyperbolic trajectory, with a single impulse at the pericenter (see Figure 6.11);

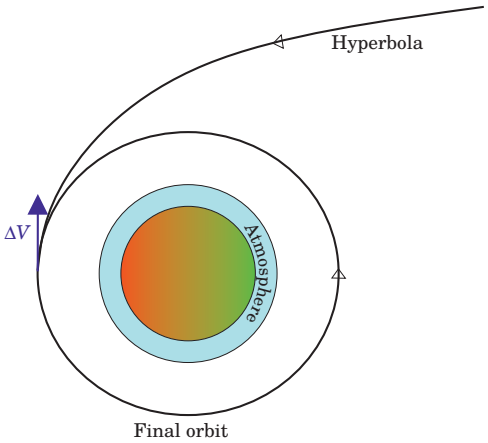

FIGURE 6.11. Direct insertion: the spacecraft arrives on a *hyperbola* and a *single impulse* at its pericenter (in blue) moves the probe to the *final orbit*.

2. *Two-impulse maneuver*: this exploits both the Oberth effect and the solar gravity gradient. It is similar to the aero-ballistic capture, but instead of performing an atmospheric passage, the spacecraft is inserted on a transfer orbit with a very high apocenter using a propulsive maneuver. Thus, this technique will follow this path:

   i) At the beginning the spacecraft approaches Mars with an hyperbolic trajectory with the pericenter at a fixed altitude, outside the atmosphere. A conservative value of 200 km is selected;

   ii) At the pericenter of the hyperbolic trajectory, a first impulsive maneuvers is performed, in order to bring the spacecraft on a closed transfer orbit, but with a very high apocenter, such that the effects of solar gravity cannot be neglected;

   iii) The Sun gravity field accelerates the probe when it is far from Mars and, thus, the pericenter is naturally raised at the desired altitude;

   iv) Finally, at the pericenter of this transfer orbit a second propelled impulse is given in order to reduce the velocity and so lowering the apocenter to a prescribed value.

   Figure 6.12 shows the trajectory for this strategy.

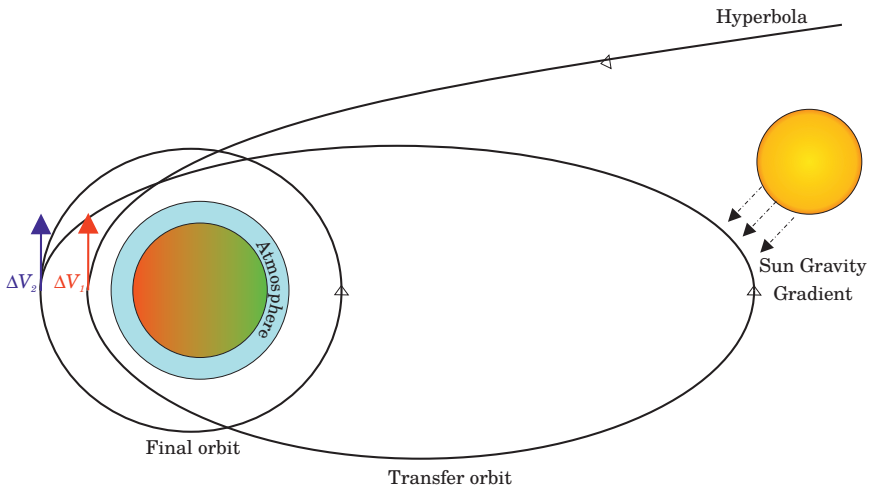

FIGURE 6.12. The different phases of two-impulse maneuver: the spacecraft arrives on a *hyperbola*; then a *first impulse* at hyperbola pericenter (in red) brings the vehicle on a very elliptic transfer orbit; during the *ballistic phase* the solar gravity gradient raises the pericenter (dotted arrows); a *second impulse* is performed (in blue) moving the probe to the *final orbit*.

6.4.1 Methodology

6.4.1.1 Direct insertion

The direct insertion with a single impulse maneuver does not take in account the presence of the Sun or other bodies and, since the energy will always assume quite high values, everything can be evaluated simply using the analytic expressions for the two-body problem. So, using the same V_∞ used for the aero-ballistic capture problem, that is

$$V_\infty = \sqrt{V_0^2 - \frac{2\mu_{\male}}{r_{interface}}} \tag{6.6}$$

the velocity at the pericenter of the hyperbola can be computed as

$$v_{p_h} = \sqrt{V_\infty^2 - \frac{2\mu_{\male}}{r_p^*}} \tag{6.7}$$

Then, the velocity for the desired circular orbit is computed as

$$v_p^* = \sqrt{\frac{\mu_{\male}}{r_p^*}} \tag{6.8}$$

And, in conclusion,

$$\Delta V = v_{p_h} - v^* \tag{6.9}$$

In this case, the final mass can be evaluated through

$$m_{fin} = m_0 e^{-\frac{\Delta V}{I_{sp} g_0}} \tag{6.10}$$

6.4.1.2 Two-impulse maneuver

In order to solve the two-impulse maneuver problem, since it is similar to the aero-ballistic capture problem, it is solved in a similar way.
In fact, a solution is sought finding V_p (that is the pericenter velocity of the transfer orbit), α and f_0 that minimize the cost function

$$J\left(V_p,\ \alpha,\ f_0\right) = -m_0 e^{-\frac{\Delta V}{I_{SP} g_0}} \tag{6.11}$$

with

$$\Delta V = \Delta V_1 + \Delta V_2 \tag{6.12}$$

where

$$\begin{aligned} \Delta V_1 &= v_{p_h} - V_p \\ \Delta V_2 &= v_p^* - \left\| \mathbf{V}\left(t_{fin}\right) \right\| \end{aligned} \tag{6.13}$$

subjected to the final constraint

$$\left\| \mathbf{R}\left(t_{fin}\right) \right\| = r_p^* \tag{6.14}$$

where

$$\begin{bmatrix} \mathbf{R} \\ \mathbf{V} \end{bmatrix}_{t_{fin}} = \mathscr{M}_{\alpha,\, f_0}\left(r_p,\, V_p,\, 0\right) \tag{6.15}$$

with t_{fin} the time when the conditions

$$\begin{cases} \mathbf{V}\left(t_{fin}\right) \cdot \mathbf{R}\left(t_{fin}\right) = 0 \\ \left\| \mathbf{V}\left(t_{fin}\right) \cdot \mathbf{R}\left(t_{fin}\right) \right\| < 0 \end{cases} \tag{6.16}$$

are attained. $\mathscr{M}$ is the same map used for aero-ballistic capture, described in Subsection 4.3.2. As inputs, position and velocity of the transfer orbit pericenter are used, instead of the state at the end of the atmospheric phase. The value of v_{p_h} is computed as

$$v_{p_h} = \sqrt{V_\infty^2 - \frac{2\mu_{\male}}{r_p}} \tag{6.17}$$

with r_p that is the fixed hyperbolic pericenter altitude, while v_p^* is the same in Eq. (6.8). From the numerical point of view, the same techniques illustrated in Section 5.4 are implemented. This means that a *MultiStart* algorithm is used as global solver, with as local minimization method an interior point scheme.

6.4.2 Low-Mars orbit

Table 6.16 summarizes the relevant data found for the single-impulse strategy. The computed ΔV is very high, bring to a very low value for the final mass.

ΔV [km/s]	m_{fin} [kg]
2.394	**1026**

TABLE 6.16. Relevant values for mass computation for the direct insertion to a Low-Mars orbit.

On the other hand, if a two-impulse strategy is considered, better performances are expected. Table 6.17 shows the optimization parameters for this maneuver to a low-Mars orbit, while Table 6.18 shows the values of the impulses together with the final mass. As expected this last figure is higher with respect to a direct insertion, but of a negligible amount. The time of flight from the first impulse to the final orbit is about 8 days, lower with respect to the one of aero-ballistic capture, since that the pericenter has to be raised of a smaller quantity and so the transfer orbit will be closer to Mars.

V_p [km/s]	α [°]	f_0 [°]
4.829	138.11	355.19

TABLE 6.17. Optimization parameters for the two-impulse maneuver to a low-Mars orbit.

ΔV_1 [km/s]	ΔV_2 [km/s]	m_{fin} [kg]
1.027	1.355	**1030**

TABLE 6.18. Relevant values for mass computation for the two-impulse maneuver to a low-Mars orbit.

In Figures 6.13(a) and 6.13(b) the spacecraft trajectory is plotted. It can be seen that the apocenter is in the IV quadrant and its value is 46 Mars radii, lower than the one for aero-ballistic capture. These results agree with theory and previous reasoning.

6.4.3 Areostationary

Results for a direct insertion on an areostationary orbit are presented in Table 6.19. Also in that case the propellant mass needed for the injection in very high and, as consequence, the final mass is very low.

ΔV [km/s]	m_{fin} [kg]
2.378	**1032**

TABLE 6.19. Relevant values for mass computation for the direct insertion to an areostationary orbit.

Considering the two-impulse maneuver, optimization parameters are shown in Table 6.20. The velocity at the pericenter is not so different from the LMO case. So, for the two-impulse maneuver, the initial velocity of the transfer orbit is not so important, but it

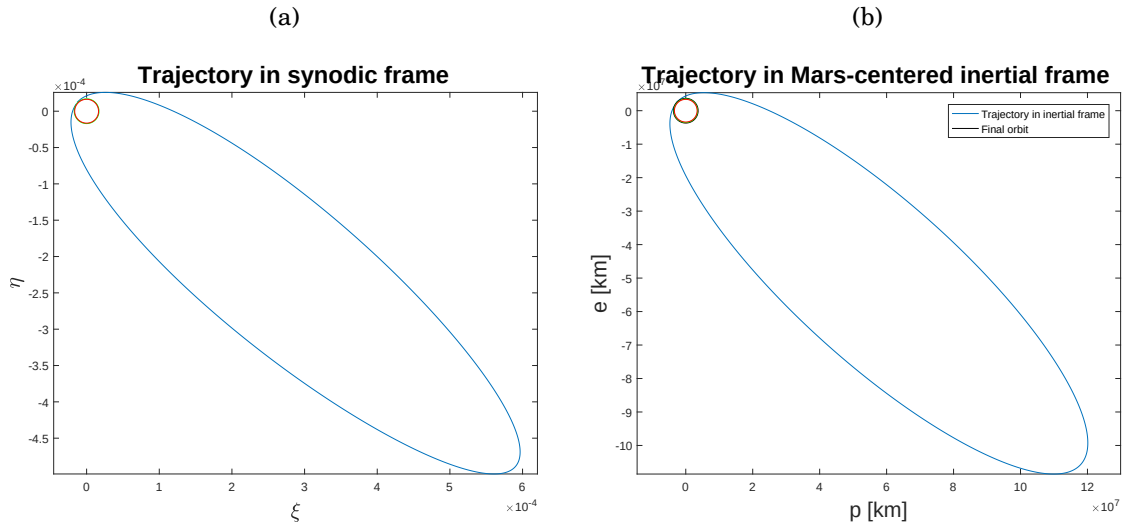

FIGURE 6.13. (a) Trajectory in synodic frame of a two-impulse maneuver to a low-Mars orbit. Sun is at far left. (b) Trajectory in Mars-centered inertial frame of a two-impulse maneuver to a low-Mars orbit.

is the celestial configuration that drives mostly the transfer orbit. This observation is similar the one done for the aero-ballistic capture.

For this problem, relevant results are reported in Table 6.21. The final mass is higher than the single-impulse maneuver, but it is still lower to the ones of both the aero-assisted problems, since that the propellant needed for the first impulse is higher than the TPS mass.

The maneuver time is about 58 days, slight lower than aero-ballistic capture total time.

V_p [km/s]	α [°]	f_0 [°]
4.879	113.25	318.36

TABLE 6.20. Optimization parameters for the two-impulse maneuver to an areostationary orbit.

ΔV_1 [km/s]	ΔV_2 [km/s]	m_{fin} [kg]
0.986	0.564	**1343**

TABLE 6.21. Relevant values for mass computation for the two-impulse maneuver to an areostationary orbit.

Trajectories for the two-impulse strategy both in synodic and inertial reference frame are plotted in Figures 6.14(a) and 6.14(b).

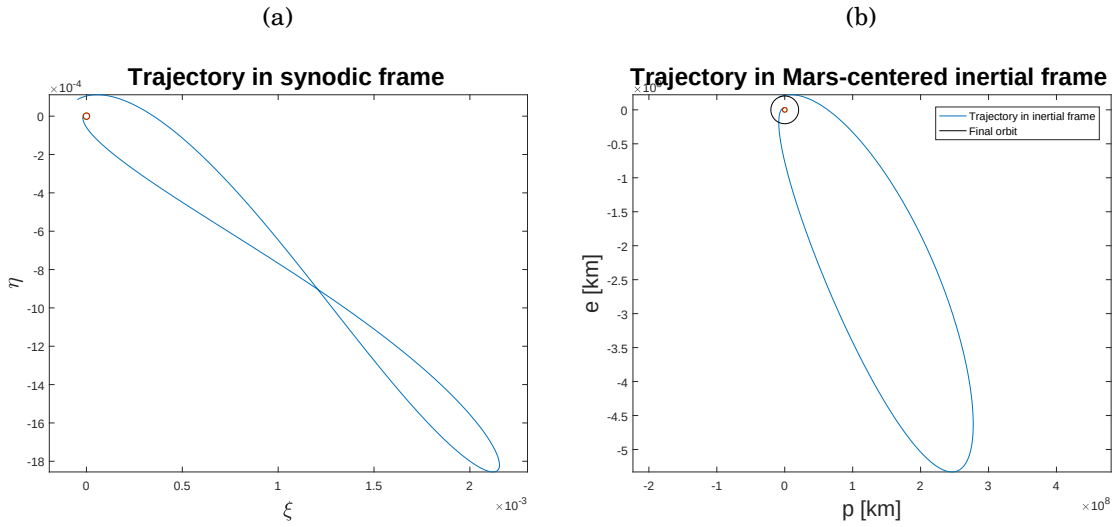

FIGURE 6.14. (a) Trajectory in synodic frame of a two-impulse maneuver to an areostationary orbit. Sun is at far left. (b) Trajectory in Mars-centered inertial frame of a two-impulse maneuver to an areostationary orbit.

6.4.4 Moons

Results related to direct insertion to the moons' orbits can be found in Table 6.22. For both the natural satellites, the maneuver cost is similar and it is again very high, meaning a low value for the final mass. In all the four study cases, the needed ΔV is between 2.2 and 2.4 km/s.

	ΔV [km/s]	m_{fin} [kg]
Phobos	2.287	**1062**
Deimos	2.403	**1023**

TABLE 6.22. Relevant values for mass computation for the direct insertion to moons' orbits.

In Table 6.23, the optimization parameters for the two-impulse maneuver are summarized. Again, the pericenter velocity is similar to the previous study cases, with only α and the primaries true anomaly that change.

Relevant data for the mass computation for the two-impulse strategy can be found in Table 6.24. If the first impulse does not change its magnitude, as expected, the second impulse is distance dependent and, as already realized, decreases increasing final orbit distance. This means that as aero-ballistic capture, the final mass increases with desired orbit altitude.

	V_p [km/s]	α [°]	f_0 [°]
Phobos	4.876	115.26	341.27
Deimos	4.480	127.58	329.84

TABLE 6.23. Optimization parameters for the two-impulse maneuver to moons' orbits.

The final mass value, as already observed in the other study cases, is lower than aero-assisted strategies.

	ΔV_1 [km/s]	ΔV_2 [km/s]	m_{fin} [kg]
Phobos	0.989	0.856	**1222**
Deimos	0.986	0.522	**1361**

TABLE 6.24. Relevant values for mass computation for the two-impulse maneuver to moons.

6.5 General comparison

In order to understand when aero-ballistic capture is convenient with respect to aero-capture, a general comparison has to be performed. For this reason, some best solutions are sought for final circular orbits with altitudes from 200 km up to 25000 km, for both the aero-assisted problems. In addition, solutions are computed also for fully propulsive maneuvers.

Results can be found in Figure 6.15. For lower orbits aerocapture is more efficient and the final mass is higher; but above 10000 km of altitude, aero-ballistic capture becomes the optimal solution in terms of final mass maximization. The higher is the orbit, the better is aero-ballistic capture. This result is achieved because both the total head load in the atmospheric phase and the needed propellant for the final orbit injection are lower. As already observed, fully propulsive solutions are very inefficient, with two-impulse maneuver that is always better than a single-impulse maneuver.

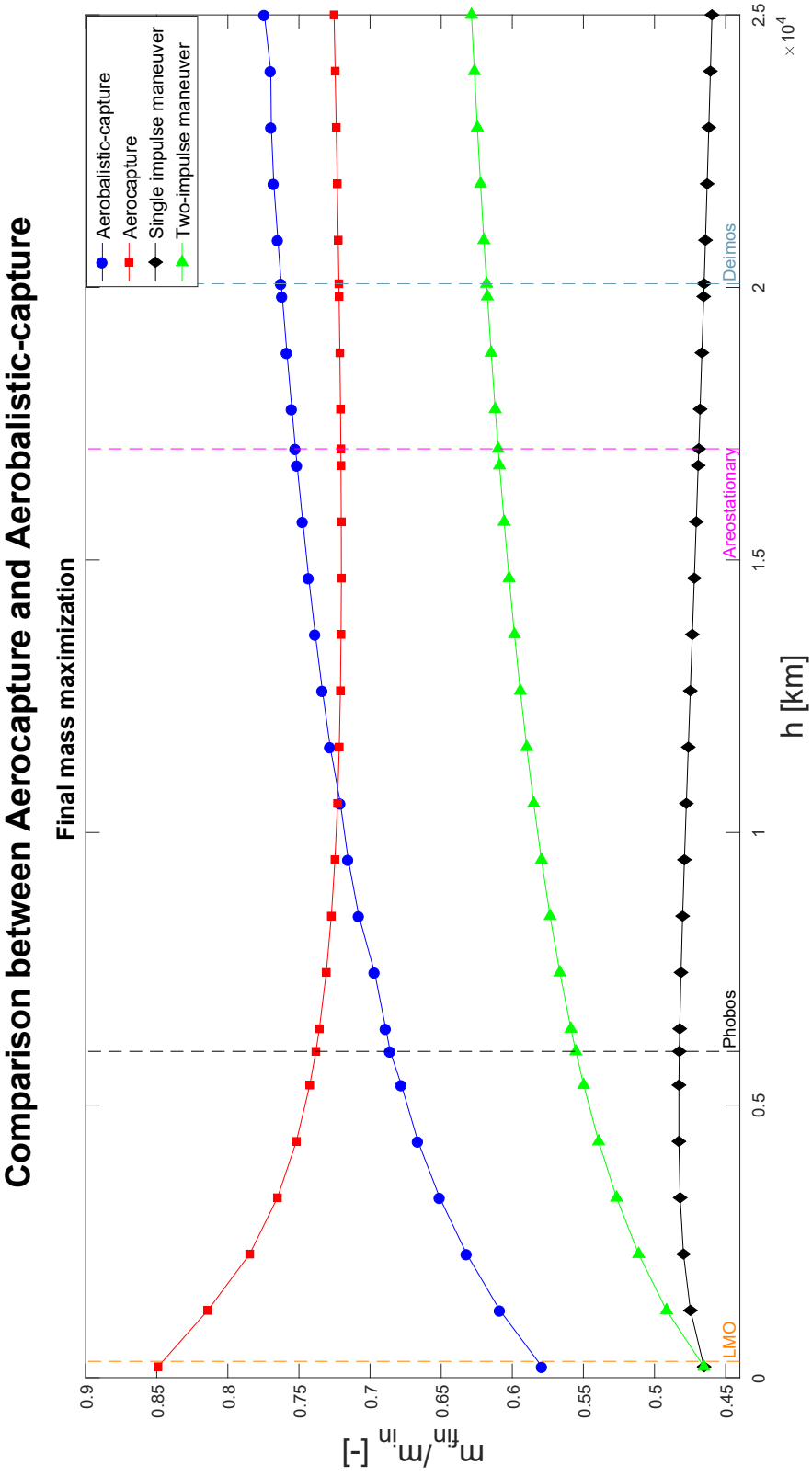

FIGURE 6.15. Comparison of between aero-ballistic capture and aerocapture. Markers indicate where the optimization is actually performed. Study cases orbits are reported in dashed lines.

CHAPTER 7

CRITICAL ANALYSIS

As last point of the thesis a critical analysis on the solutions found in Chapter 6 has to be performed in order to study their robustness against single point failures and variation of the optimization parameters and, then, a focus on the feasibility of the optimal solutions is done.

7.1 Robustness analysis against single-point failure

In aerocapture, if no maneuver is performed at apocenter, that means if a single point failure (SPF) happens, the pericenter of the transfer orbit is still inside the atmosphere and so, after only a revolution, the spacecraft will interact again with it, crashing then on the planet. On the other hand, for aero-ballistic capture, the pericenter is raised naturally outside the atmosphere and, so, the spacecraft is able to continue to revolve about the planet, even if on a very elliptic orbit.
Taking, for example, as final orbit, an areostationary orbit, the trajectory in Figures 7.1(a) and 7.1(b) is followed by the spacecraft.
In inertial frame, the path followed by the spacecraft is formed by different ellipses, with similar shape and, above all, with similar direction. This observation leads to have, in synodic frame, an orbit with the apsis line that rotates clockwise (since Mars rotation is counterclockwise) and so its apocenter goes from the II quadrant to the I (or from the IV to the III). By the theory about the Solar gravitational gradient, the pericenter reduces when apocenter is in the I or III quadrant and, thus, there is the possibility

the spacecraft enters again the atmosphere and crashes. This is what happens in this example: in the last orbit, the apocenter is at the center of the I quadrant, the pericenter is lowered below the atmospheric interface and, so, the spacecraft crashes.
The altitude with respect to Mars, plotted in Figure 7.1(c), clearly shows this phenomenon.

(a)

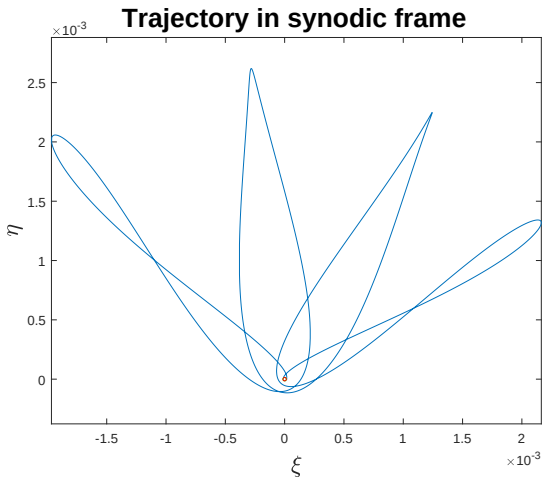

(b)

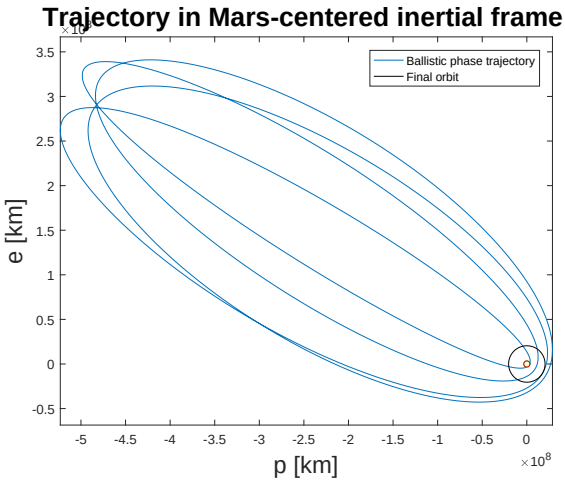

(c)

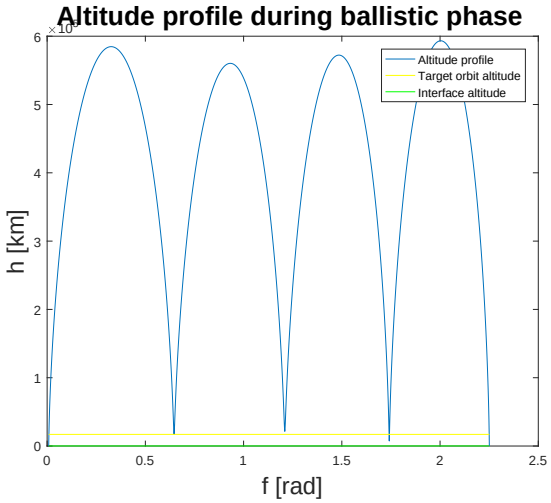

FIGURE 7.1. (a) Trajectory in synodic frame in case of single point failure of an aero-ballistic capture to an areostationary orbit. (b) Trajectory in Mars-centered inertial frame in case of single point failure of an aero-ballistic capture to an areostationary orbit. (c) Altitude profile in case of single point failure of an aero-ballistic capture to an areostationary orbit.

Moreover, in this situation, the spacecraft stays naturally around the planet for more than an orbit and, since they are very elliptic orbit, their orbital period is quite long. Thus, without any maneuver, the vehicle is able to stay around the planet for a very long time. For example, for the optimal areostationary solution, the vehicle revolves about Mars before crashing for 228 days. In case of failure, this huge amount of time can be used to recover the mission, changing objectives or finding alternative ways of maneuvering.
Some trajectories allows to revolve longer about the planet, depending on the relative position of the primaries. In that case, the spacecraft "survives" at the first change of quadrant and it crashes after 18 months.
In conclusion, the aero-ballistic capture is more robust against SPFs, since that, if the maneuver at the pericenter cannot be performed for an engine failure, the mission is not totally jeopardized, but a recovery can be still feasible.

7.1.1 Robustness analysis against optimal parameters

When a real mission is accomplished, it is quite impossible that the optimization parameters computed during the simulation correspond to the actual ones. In fact, due to non-modeled small effects or due to sensors accuracy, errors in parameters appears. For example, some wind can be present in the atmosphere and this alters the actual value of the bank angle; this effect cannot be reproduced, because of the unpredictable behavior of the atmosphere. So, for this reason, it is important to investigate what happens if small variations in parameters are taken in account.
Figure 7.2 shows the violation of the final constraint, varying one by one the optimization parameter for the optimal areostationary solution.
Final constraint variation is evaluated through the relative error, defined as

$$\Delta r_p = \frac{\left\|\mathbf{R}\left(t_{fin}\right)\right\| - r_p^*}{r_p^*} \tag{7.1}$$

On the other hand, the considered variations in parameters are

$$\begin{aligned} t_s &= t_s^* \pm 5 \text{ s} \\ \sigma_d &= \sigma_d^* \pm 4^\circ \\ \alpha &= \alpha^* \pm 3^\circ \\ f_0 &= f_0^* \pm 2^\circ \end{aligned} \tag{7.2}$$

where with the star are indicated the optimal values show in Table 6.4.
An error of 5 seconds in switching time, as showed in Figure 7.2(a), produces a maximum

relative error of 1.4% that, for an areostationary orbit, is about 250 km. Furthermore, if the reversal time is anticipated, the error is negative, meaning that the final pericenter has a lower altitude with respect to the prescribed one. This result can be explained with the fact that the spacecraft is lift-down and, so, it undergoes the effect of the atmosphere for a longer period. More energy is removed by friction and the exit velocity is slightly lower.

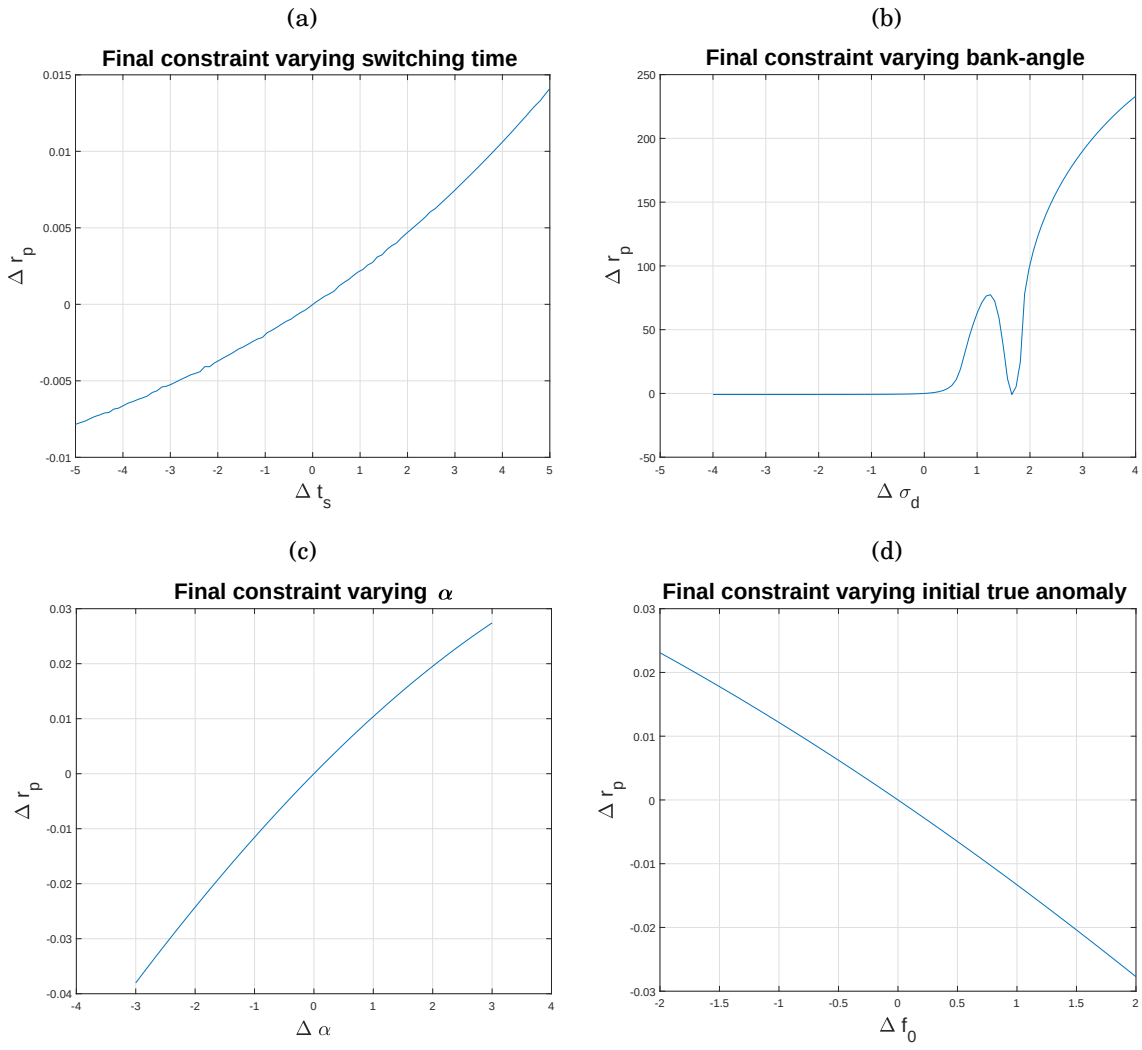

FIGURE 7.2. (a) Final constraint error varying the switching time. (b) Final constraint error varying the final bank angle. (c) Final constraint error varying α. (d) Final constraint error varying initial true anomaly.

A bigger error can be found for variation of α (see Figure 7.2(c)). If the relative position of the spacecraft with respect to the primaries is biased according to (7.2), a

maximum error of 4% is found.
Also for errors in the primaries true anomaly at the beginning of the ballistic phase, the error obtained is quite low, with a maximum value of less than 3%, that means about 470 km.
Problems appear only for variations in σ_d. In fact, in that case, as showed in Figure 7.2(b), some absurd values for the final pericenter are found. If a positive error of 4° is committed in the maximum bank angle, the final constraint relative error is equal to 20000%. In order to understand what is the phenomenon underneath these strange results, the problem with $\sigma_d = \sigma_d^* + 4°$ is studied.
In Figure 7.3(a), the energy during the atmospheric phase is plotted. It is possible to see that, at the atmospheric exit, the energy is still positive and so the result will be an open orbit with respect to Mars. Figure 7.3(b) clearly shows the fact that the spacecraft escapes. This result is obtained because, as observed in Chapter 6, the nominal solution orbital energy at the end of the atmospheric phase is quite close to 0, since the apocenter of the transfer orbit has to be at the boundaries of Mars sphere of influence. If the bank angle is changed too much, less energy is dissipated and, thus, the energy remains above 0 and the spacecraft escapes.
So, particular attention has to be paid in bank-angle determination sensors, if an aero-ballistic capture to high orbits is designed, in order to avoid possible failures.

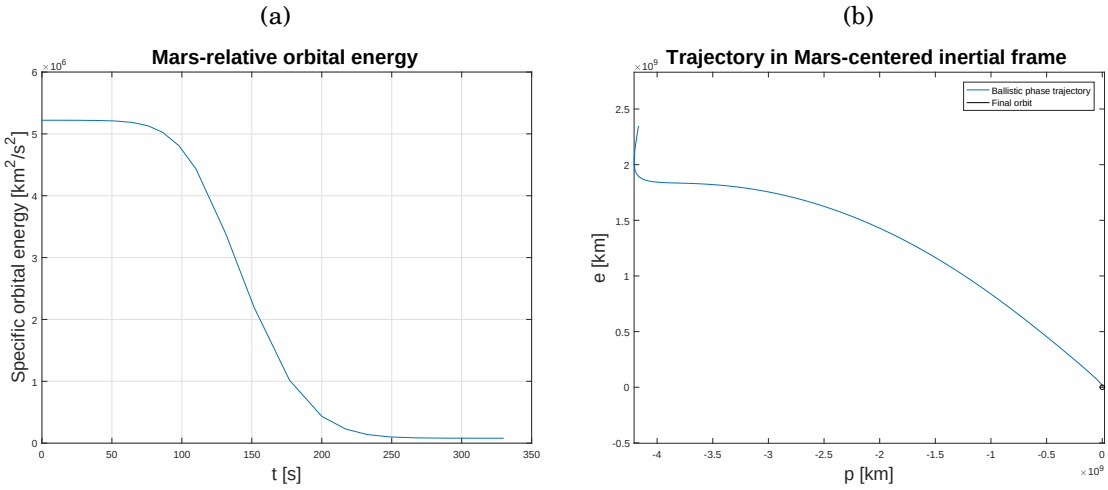

FIGURE 7.3. (a) Orbital energy with respect to Mars during the atmospheric phase of the aero-ballistic capture with bank angle variation. (b) Trajectory in Mars-centered inertial frame for the ballistic phase of an aero-ballistic capture with bank angle variation.

7.2 Critical analysis

Aero-ballistic capture solutions need a peculiar combination of different factors that cannot be controlled by designers. For example, both the V_∞ and f_0 are determined by the orbital mechanics of the Solar system; but it is possible to find not feasible or not convenient trajectories for a given couple of residual velocity and Mars true anomaly. For this reason a critical analysis that studies the feasibility of the optimal aero-ballistic capture solutions is needed.
Figure 7.4 shows the porkchop plot for an Earth to Mars trip. Departure date are selected from the 1st January 2017 to 1st January 2022, with the time of flight going from 150 days up to 500 days. Minima are inside the blue contour lines.

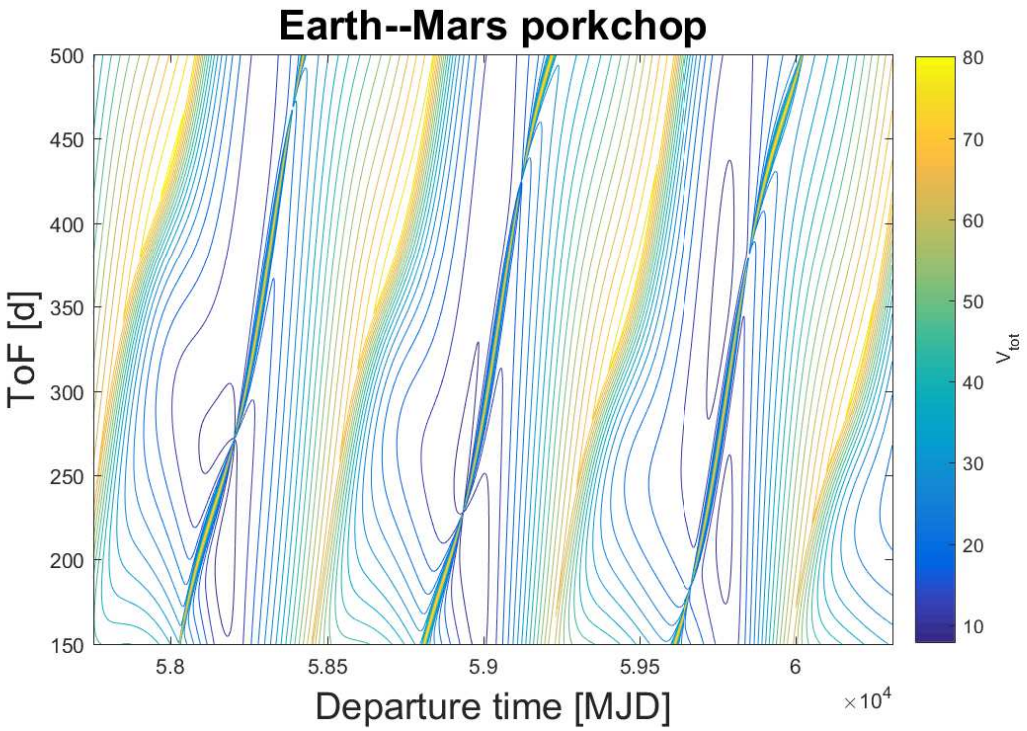

FIGURE 7.4. Earth–Mars porkchop plot. Contour lines represent constant V_{tot} solution.

On this plot, it is possible to draw areas with a given V_∞ (the residual velocity at Mars), in a interval close to the one selected for this study, that is equal to 3.23 km/s. If the interval selected is $V_\infty = V_\infty^* \pm 0.5$ km/s, where V_∞^* is the nominal solution, Figure 7.5 is obtained.
These areas contain the minima or they are very close to them. This means that an

optimal solution also from the launching point of view is selected: trajectories with low residual velocity at the Earth are chosen, allowing to launch an higher mass in the interplanetary journey.

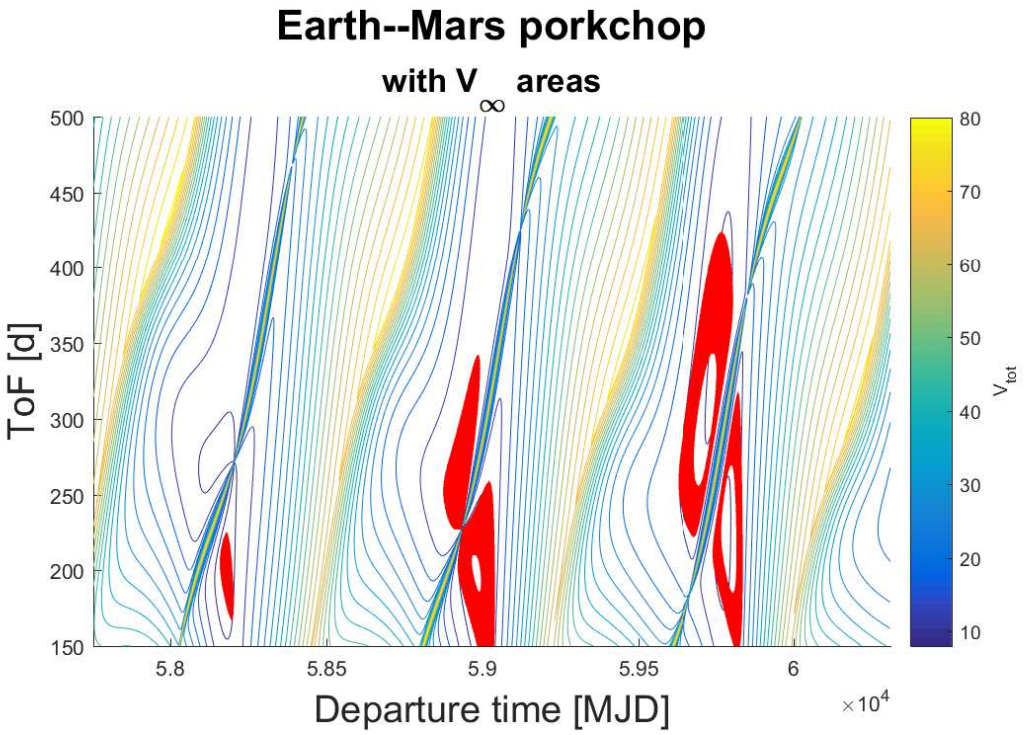

FIGURE 7.5. Earth–Mars porkchop plot. Contour lines represent constant V_{tot} solution. Red areas are the solution with V_∞ inside the given interval.

Now, the aim is to show if the solutions inside the red areas are compatible with the relative configuration of the celestial bodies required by the optimal aero-ballistic capture problem.
In the case studies for the areostationary orbit and to the moons' orbits, Mars is close to the pericenter, so in the porkchop plot, diagonal lines that represent when Mars is at its pericenter are plotted. Figure 7.6 show this result. Only for the first red area, there is the possibility of an arrival at Mars when $f_0 = 0$ and with a residual velocity compatible with the one used in the thesis. So, the solution found is feasible, but only a launch window is available in the next five years.

So, a new question arises: is it possible to have a good sub-optimal solution when $f_0 \neq 0$, in order to have more launch windows in the next future?
If the condition $f_0 = 45°$ is considered, the porkchop plot for Earth–Mars missions become

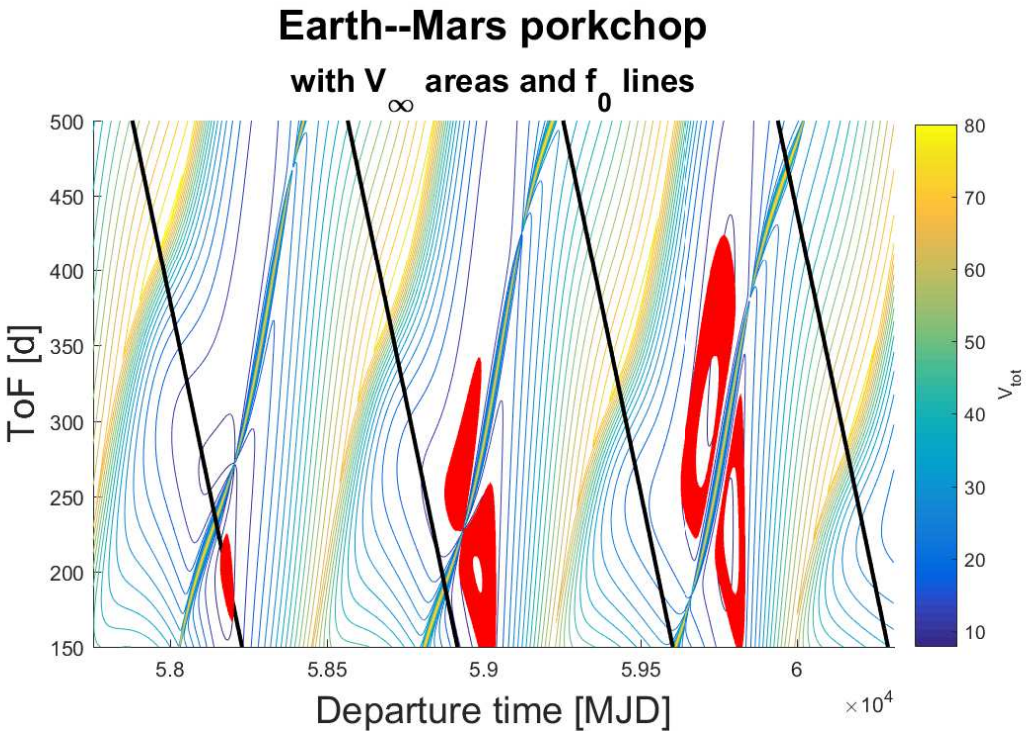

FIGURE 7.6. Earth–Mars porkchop plot. Contour lines represent constant V_{tot} solution. Red areas are the solution with V_∞ inside the given interval. Diagonal black lines represent the time when $f_0 = 0$.

the one in Figure 7.7, where magenta diagonal lines represent the arrival time with the desired true anomaly. In this case, the intersection is in the second red area.

If a solution compatible with the Figure 7.7 is sought, fixing $f_0 = 45°$, results found are not far from the optimal one.

For an areostationary orbit, relevant data are shown in Table 7.1. With respect to the optimal solution, ballistic phase lasts 13 days more, since the spacecraft has to go far to increase the orbit radius of the same amount. On the other hand, the final mass found is not so far from the optimal one, being only 1 kg lower.

In conclusion, even if f_0 is different from the optimal one, a good solution can be found, allowing to have more opportunity to launch, increasing so the feasibility of the mission.

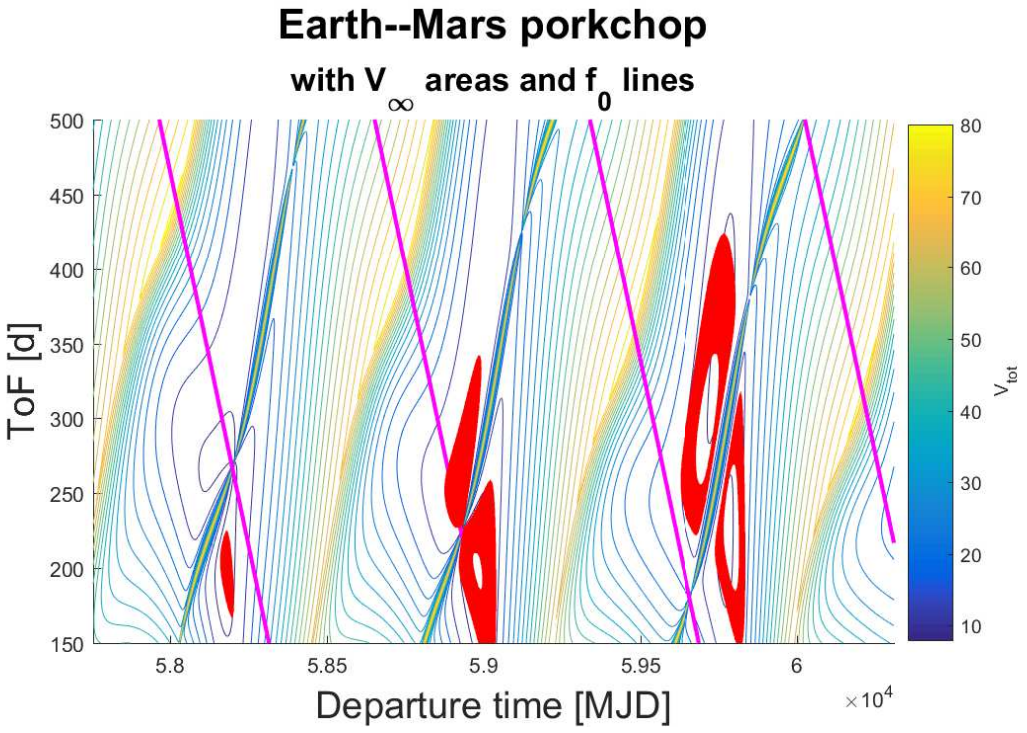

FIGURE 7.7. Earth–Mars porkchop plot. Contour lines represent constant V_{tot} solution. Red areas are the solution with V_∞ inside the given interval. Diagonal magenta lines represent the time when $f_0 = 45°$.

t_{out} [s]	t_{BAL} [d]	t_{fin} [d]
334.19	71.14	71.15
Δt_{out} [s]	Δt_{BAL} [d]	Δt_{fin} [d]
-0.12	12.85	12.86

$q(t_{out})$ [J/cm^2]	ΔV [km/s]	m_{fin} [kg]
8950	0.567	**1654**
$\Delta q(t_{out})$ [J/cm^2]	$\Delta(\Delta V)$ [km/s]	Δm_{fin} [kg]
-5	0.003	-1

TABLE 7.1. Times and relevant values for mass computation for the aeroballistic capture to an areostationary orbit with $f_0 = 45°$. Δ indicates the variation with respect to the nominal optimal solution.

CHAPTER 8

CONCLUSIONS AND FURTHER DEVELOPMENTS

In conclusion, a summary of the results attained in the thesis is be presented. Furthermore, future developments are addressed in the last section.

8.1 Summary of results

In this work a method merging aerocapture and ballistic capture is designed and its optimization is studied and discussed.
This technique, called aero-ballistic capture, exploits the interaction of a spacecraft with the atmosphere, in order to remove energy thanks to friction. At the exit from the atmosphere, the vehicle is on an elliptic orbit, that brings it far from the planet. There, the interaction with the solar gravity can raise the pericenter of this transfer orbit outside the atmosphere up to a prescribed value. At the end, a propelled maneuver is performed in order to move the probe to the final orbit.
It is possible to determine that the optimal control for this problem has a bang-bang structure, allowing to solve it as a non-linear programming problem.
Some study cases are analyzed, showing that trajectory is driven more by the ballistic phase than the atmospheric phase and the final mass, that is the cost function for this problem, increases, increasing the altitude of the final orbit.
Comparison with aerocapture and fully propulsive maneuvers shows that aero-ballistic capture gives advantages in terms of final mass for high altitude orbits, with a target distance from Mars center more than 13400 km. Furthermore, it is more robust with

respect to aerocapture against single point failures, since the spacecraft revolves about the planet for a long time before crashing, if no maneuver is performed.
Also, feasibility of these solution is analyzed, as last point, showing that there is compatibility between the solutions found and the Solar system dynamics in the next future. Furthermore it is noted that more launch windows can be used, apart from the nominal ones, because good solutions can be found even if the relative positions of the primaries is not the optimal one.

8.2 Future improvements

This thesis is only a starting point for the aero-ballistic capture. A guidance algorithm has to be developed in order to study also the orbit inclination targeting and the behavior of the spacecraft when the bank-angle reversal occurs in a finite amount of time. Then, more sophisticated models can be implemented both for the atmospheric phase and for the ballistic trajectory. For example, the lateral dynamics has to be analyzed during the atmospheric flight and a three-dimensional 3-body problem can be used outside the atmosphere. On the other hand, since the transfer orbit lasts for a very long time, the use of electric propulsion to lower the apocenter can be studied. For the same purpose, also aerobraking can be analyzed and multiple high altitude passage in Martian atmosphere can be performed in order to slowly dissipate orbital energy.

BIBLIOGRAPHY

[1] E. A. BELBRUNO AND J. K. MILLER, *Sun-perturbed Earth-to-Moon transfers with ballistic capture*, Journal of Guidance, Control, and Dynamics, 16 (1993), pp. 770–775.

[2] C. CIRCI AND P. TEOFILATTO, *On the dynamics of weak stability boundary lunar transfers*, Celestial Mechanics and Dynamical Astronomy, 79 (2001), pp. 41–72.

[3] H. FRAYSSE, R. POWELL, S. ROUSSEAU, AND S. STRIEPE, *CNES-NASA Studies of the Mars Sample Return Orbiter aerocapture phase*, (2000).

[4] J. R. FRENCH AND M. I. CRUZ, *Aerobraking and aerocapture for planetary missions.*, Astronautics & Aeronautics New York, N.Y., 18 (1980), pp. 48–55, 71.

[5] J. L. HALL, M. A. NOCA, AND R. W. BAILEY, *Cost-benefit analysis of the aerocapture mission set*, Journal of Spacecraft and Rockets, 42 (2005), pp. 309–320.

[6] J.-F. HAMEL AND J. D. LAFONTAINE, *Improvement to the analytical predictor-corrector guidance algorithm applied to Mars aerocapture*, Journal of Guidance, Control, and Dynamics, 29 (2006), pp. 1019–1022.

[7] T.-Y. HUANG AND K. INNANEN, *The gravitational escape/capture of planetary satellites*, The Astronomical Journal, 88 (1983), pp. 1537–1548.

[8] N. HYERACI AND F. TOPPUTO, *Method to design ballistic capture in the elliptic restricted three-body problem*, Journal of Guidance, Control, and Dynamics, 33 (2010), pp. 1814–1823.

[9] ——, *The role of true anomaly in ballistic capture*, Celestial Mechanics and Dynamical Astronomy, 116 (2013), pp. 175–193.

[10] C. G. JUSTUS AND R. D. BRAUN, *Atmospheric environments for entry, descent and landing (EDL)*, Technical report, NASA Marshall Space Flight Center, (2007).

[11] A. M. KORZUN, G. F. DUBOS, C. K. IWATA, B. A. STAHL, AND J. J. QUICKSALL, *A concept for the Entry, Descent, and Landing of high-mass payloads at Mars*, Acta Astronautica, 66 (2010), pp. 1146–1159.

[12] A. I. KOZYNCHENKO, *Development of optimal and robust predictive guidance technique for Mars aerocapture*, Aerospace Science and Technology, 30 (2013), pp. 150–162.

[13] J. M. LAFLEUR, *The conditional equivalence of ΔV minimization and apoapsis targeting in numerical predictor-corrector aerocapture guidance*, NASA TM-2011-216156, (2011).

[14] N. LAY, C. CHEETHAM, H. MOJARADI, AND J. NEAL, *Developing low-power transceiver technologies for in situ communication applications*, Jet Propulsion Laboratory, California Inst. of Technology, Pasadena, CA, Interplanetary Networks Prog. Rep, (2001), pp. 42–147.

[15] M. K. LOCKWOOD, *Titan aerocapture systems analysis*, in 39th AIAA/ASME/SAE/ASEE Joint Propulsion Conference and Exhibit, 2003.

[16] ——, *Neptune aerocapture systems analysis*, in Collection of Technical Papers - AIAA Atmospheric Flight Mechanics Conference, vol. 1, 2004, pp. 660–675.

[17] J. M. LONGUSKI, J. J. GUZMÁN, AND J. E. PRUSSING, *Optimal control with aerospace applications*, vol. 32, Springer Science & Business Media, 2013.

[18] P. LU, *Entry guidance: a unified method*, Journal of guidance, control, and dynamics, 37 (2014), pp. 713–728.

[19] P. LU, C. J. CERIMELE, M. A. TIGGES, AND D. A. MATZ, *Optimal Aerocapture Guidance*, Journal of Guidance, Control, and Dynamics, 38 (2015), pp. 553–565.

[20] Z. LUO AND F. TOPPUTO, *Analysis of ballistic capture in Sun-planet models*, Advances in Space Research, 56 (2015), pp. 1030–1041.

[21] ——, *Capability of satellite-aided ballistic capture*, Communications in Nonlinear Science and Numerical Simulation, 48 (2017), pp. 211–223.

[22] Z. LUO, F. TOPPUTO, F. BERNELLI-ZAZZERA, AND G. TANG, *Constructing ballistic capture orbits in the real Solar System model*, Celestial Mechanics and Dynamical Astronomy, 120 (2014), pp. 433–450.

[23] D. LYONS, *Mars reconnaissance orbiter: aerobraking reference trajectory*, in AIAA/AAS Astrodynamics Specialist Conference and Exhibit, 2002, p. 4821.

[24] J. P. MASCIARELLI, S. ROUSSEAU, H. FRAYSSE, AND E. PEROT, *An analytic aerocapture guidance algorithm for the Mars Sample Return Orbiter*, in Atmospheric Flight Mechanics Conference, 2000.

[25] A. MIELE, T. WANG, W. LEE, AND Z. ZHAO, *Optimal trajectories for the aeroassisted flight experiment*, Acta Astronautica, 21 (1990), pp. 735–747.

[26] D. OLYNICK, M. LOOMIS, Y. . CHEN, E. VENKATAPATHY, AND G. ALLEN, *New TPS design strategies for planetary entry vehicle design*, in 37th Aerospace Sciences Meeting and Exhibit, 1999.

[27] J. PARKER AND C. M. HOGAN, *Techniques for wind tunnel assessment of ablative materials*, NASA Ames Research Center, Technical Publication, (1965).

[28] D. PITTS, J. TILLMAN, N. JOHNSON, J. MURPHY, J. POLLACK, D. COLBUM, R. HABERLE, R. ZUREK, AND I. STEWART, *The Mars Atmosphere: Observations and Model Profiles for Mars Missions*, NASA JSC-24455, (1990).

[29] L. PONTRYAGIN, V. BOLTYANSKII, AND R. GAMKRELIDZE, *The mathematical theory of optimal processes*, John Wiley & Sons, 1962.

[30] R. POWELL, W. WILLCOCKSON, AND M. JOHNSON, *Numerical predictor corrector aerocapture and precision landing guidance algorithms for the Mars 2001 missions*, AIAA-98-4573, AIAA Atmospheric Flight Mechanics Conference, Boston, MA, 1998.

[31] P. PRINCE AND J. DORMAND, *High order embedded Runge-Kutta formulae*, Journal of Computational and Applied Mathematics, 7 (1981), pp. 67–75.

[32] E. M. REPIC, M. G. BOOBAR, AND F. G. CHAPEL, *Aerobraking as a potential planetary capture mode*, Journal of Spacecraft and Rockets, 5 (1968), pp. 921–926.

[33] T. U. RO AND E. M. QUEEN, *Mars aerocapture terminal point guidance and control*, AIAA-98-4573, AIAA Atmospheric Flight Mechanics Conference, Boston, MA, 1998.

[34] B. R. STARR AND C. H. WESTHELLE, *Aerocapture performance analysis of a Venus exploration mission*, in Collection of Technical Papers - AIAA Atmospheric Flight Mechanics Conference, vol. 1, 2005, pp. 435–448.

[35] V. SZEBEHELY, *Theory of orbit: The restricted problem of three Bodies*, Elsevier, 1967.

[36] N. TAKASHIMA, B. R. HOLLIS, E. VINCENT ZOBY, K. SUTTON, J. OLEJNICZAK, M. J. WRIGHT, AND D. PRABHU, *Preliminary aerothermodynamics of Titan aerocapture aeroshell*, in 39th AIAA/ASME/SAE/ASEE Joint Propulsion Conference and Exhibit, 2003.

[37] M. E. TAUBER, J. V. BOWLES, AND L. YANG, *Use of atmospheric braking during Mars missions*, Journal of Spacecraft and Rockets, 27 (1990), pp. 514–521.

[38] S. TAUBER, M. E. AND K. SUTTON, *Stagnation-point radiative heating relations for Earth and Mars entries*, Journal of Spacecraft and Rockets, 28 (1991), pp. 40–42.

[39] F. TOPPUTO AND E. BELBRUNO, *Computation of weak stability boundaries: Sun-Jupiter system*, Celestial Mechanics and Dynamical Astronomy, 105 (2009), pp. 3–17.

[40] D. VAUGHAN, H. C. MILLER, B. GRIFFIN, B. F. JAMES, AND M. M. MUNK, *A comparative study of aerocapture missions with a Mars destination*, in Proceedings of the 41st AIAA/ASME/SAE/ASEE Joint Propulsion Conference and Exhibit, 2005.

[41] G. D. WALBERG, *A survey of aeroassisted orbit transfer*, Journal of Spacecraft and Rockets, 22 (1985), pp. 3–18.

[42] M. J. WRIGHT, R. A. BECK, K. T. EDQUIST, D. DRIVER, S. A. SEPKA, E. M. SLIMKO, AND W. H. WILLCOCKSON, *Sizing and margins assessment of mars science laboratory aeroshell thermal protection system*, Journal of Spacecraft and Rockets, 51 (2014), pp. 1125–1138.

[43] H. YAMAKAWA, J. KAWAGUCHI, N. ISHII, AND H. MATSUO, *Numerical study of gravitational capture orbit in the Earth-Moon system*, in Advances in the Astronautical Sciences, vol. 79, 1992, pp. 1113–1132.

[44] ——, *On Earth-Moon transfer trajectory with gravitational capture*, in Advances in the Astronautical Sciences, vol. 85, 1993, pp. 397–416.